Nanostructured Spinel Oxides as Bi-functional Electrocatalysts for Rechargeable Metal-Air Batteries

by

Dong Un Lee

A thesis
presented to the University of Waterloo
in fulfillment of the
thesis requirement for the degree of
Doctor of Philosophy
in
Chemical Engineering (Nanotechnology)

Waterloo, Ontario, Canada, 2017

© Dong Un Lee 2017

EXAMINING COMMITTEE MEMBERSHIP

The following served on the Examining Committee for this thesis. The decision of the Examining Committee is by majority vote.

External Examiner	Dr. Wei Tong Principal Investigator
Supervisor(s)	Dr. Zhongwei Chen Associate Professor
Internal Member	Dr. Eric Croiset Professor
Internal Member	Dr. Aiping Yu Associate Professor
Internal-external Member	Dr. Xianguo Li Professor, PEng

AUTHOR'S DECLARATION

This thesis consists of material all of which I authored or co-authored: see Statement of Contributions included in the thesis. This is a true copy of the thesis, including any required final revisions, as accepted by my examiners.

I understand that my thesis may be made electronically available to the public.

STATEMENT OF CONTRIBUTIONS

This thesis is based upon a combination of published work. Various chapters are adapted from the following list of published work, with specific reference to the published work provided within the chapter.

D. U. Lee, J. Scott, H. W. Park, S. Abureden, J. Y. Choi, Z. Chen, “Morphologically controlled Co_3O_4 nanodisks as practical bi-functional catalyst for rechargeable zinc–air battery applications”, *Electrochemistry Communications*, 43 (2014) 109-112.

D. U. Lee, B. J. Kim, Z. Chen, “One-pot synthesis of a mesoporous $NiCo_2O_4$ nanoplatelet and graphene hybrid and its oxygen reduction and evolution activities as an efficient bi-functional electrocatalyst”, *Journal of Materials Chemistry A*, 1 (2013) 4754-4762.

D. U. Lee, J. Li, M. G. Park, M. H. Seo, W. A, I. Stadelmann, L. Ricardez-Sandoval, Z. Chen, “Self-Assembly of Spinel Nanocrystals into Mesoporous Spheres as Bifunctionally Active Oxygen Reduction and Evolution Electrocatalysts”, *ChemSusChem*, 10 (2017) 2258-2266.

D. U. Lee, J. Y. Choi, K. Feng, H. W. Park, Z. Chen, “Advanced Extremely Durable 3D Bifunctional Air Electrodes for Rechargeable Zinc-Air Batteries”, *Advanced Energy Materials*, 4 (2014) 1301389.

D. U. Lee, P. Xu, Z. P. Cano, A. G. Kashkooli, M. G. Park, Z. Chen, “Recent progress and perspectives on bi-functional oxygen electrocatalysts for advanced rechargeable metal–air batteries”, *Journal of Materials Chemistry A*, 4 (2016) 7107-7134.

ABSTRACT

Due to continuously increasing energy demands, particularly with the emergence of electric vehicles (EV), smart energy grids, and portable electronics, advanced energy conversion and storage systems such as fuel-cells and metal-air batteries have drawn tremendous research and industrial attention. Even though the lithium-ion battery technology is the most developed and widely distributed energy device for a wide range of applications, some researchers view its energy density insufficient for fulfilling the ultimate requirements of highly energy intensive applications such as EVs. Recently, zinc-air batteries have re-gained research attention since the initial development in the 1970s due to their remarkably highly energy density and the potential to be electrically rechargeable. However, some technological hurdles such as low charge/discharge energy efficiency, and insufficient cycle stability have hampered commercialization and introduction of rechargeable zinc-air batteries to the market. The mentioned hurdles are currently the main challenges of rechargeable zinc-air battery developed, and they stem from the fact that the reaction kinetics of the oxygen reduction reaction (ORR) and oxygen evolution reaction (OER) are intrinsically very sluggish. The two are the main electrochemical reactions that govern the charge and discharge processes of a rechargeable metal-air battery at the air electrode, and these oxygen reactions must be facilitated by active electrocatalysts in order to progress them at practically viable and stable rates.

Currently, the best known catalysts for ORR and OER are carbon supported platinum (Pt/C) and iridium (Ir/C), respectively. However, the use of these precious metal based catalysts for large scale applications like EVs and energy storage systems is prohibitively expensive. Additionally, the durability of these catalysts have been reported to be insufficient for long-term usage under normal device operating conditions. Perhaps most importantly, the precious metal based catalysts

are strongly active towards only one of the two oxygen reactions required for rechargeable applications. For example, Pt/C is a strong ORR active catalyst, while Ir/C is a strong OER active catalyst. Recently in the literature, a simple physical mixture of these two catalysts have been used to render bi-functionality, but this method is very rudimentary and still requires two separate syntheses for each catalyst. This suggests that future bi-functionally active catalysts must not only be non-precious (inexpensive), but also a single active material capable of catalyzing both ORR and OER over the same active surface.

Having said above, non-precious catalyst research, specifically for bi-functional ORR and OER electrocatalyses, has increased dramatically beginning in the 90's with a very popular and positive belief in the energy community that rechargeable lithium-air batteries could potentially replace lithium-ion batteries. This wave of interest has also picked up research in rechargeable zinc-air batteries since the electrochemical oxygen reactions that take place at the air electrodes are fundamentally very similar. Additionally, the use of zinc metal as the anode, which is one of Earth's most abundant elements, and the water-based (aqueous) solutions as the electrolyte (as opposed to organic ones) made the rechargeable zinc-air battery development very attractive and seemingly easy to scale-up. Moreover, primary (non-rechargeable) zinc-air batteries have already been commercialized and are available in the market as hearing aid batteries, leading many researchers to believe that a simple tuning of the current technology would lead to a successful secondary (rechargeable) zinc-air battery development. However, there are a set of technical difficulties specific to rechargeable zinc-air batteries that have slowed the development for the past few decades. Therefore, the work presented in this thesis aims to address the challenges of rechargeable zinc-air batteries particularly from the active bi-functional electrocatalyst standpoint to make them as commercially viable as possible.

In the first study, a facile hydrothermal materials synthesis technique has been employed to synthesize a non-precious metal cobalt oxide bi-functional catalyst. Microscopic characterizations have revealed the morphology of this material to be mesoporous hexagonal nanodisks, a high surface area catalyst compared to simple granular nanoparticles which enhances active site exposure and transport of reactants during the electrochemical reactions. This unique nanostructure has been made possible with the addition of surface-active agents that played a role of capping agent, binding to specific crystal faces and allowing growth of cobalt oxide only in certain directions. Additionally, the adsorbed capping agent has been found to leave mesopores on the nanodisks as it decomposes during the heat treatment following the hydrothermal process. Compared to randomly shaped nanoparticle catalyst of the same atomic composition, the mesoporous nanodisks greatly outperformed in terms of both charge and discharge performance of a rechargeable zinc-air battery.

In the second study, the bi-functional capabilities of the cobalt oxide catalyst towards the ORR and OER in the first study have been improved by introducing nickel metal substituents into the spinel crystal lattice, as well as adapting a highly conductive nano-structured carbon support. The bi-functional activity enhancements have been attributed to an increase in electrical conductivity of spinel cobalt oxide with the insertion of nickel atoms into specific interstitial sites of the spinel lattice, as well as the high surface area nano-carbon support which helped to disperse the active spinel oxide catalyst and facilitate charge transfer during the electrochemical reactions.

In the third study, the effect of nickel and manganese insertion into the spinel cobalt oxide lattice on the bi-functional catalytic activity has been studied more in detail. Spinel oxide catalysts with different atomic compositions, including cobalt oxide (un-doped), nickel cobalt oxide, and manganese cobalt oxide, have been synthesized as nanocrystals that self-assembled into high surface area porous spheres. Based on the electrochemical evaluation, the best overall bi-functional catalytic activity has been observed with nickel-substituted cobalt oxide, while the least has been observed with manganese cobalt oxide, with pristine cobalt oxide in the middle. Interestingly, computational modelling of these catalysts has resulted in the same activity trend, confirming the importance of choosing an appropriate metal substituent depending on the level of bi-functional activity required.

In the last study, the knowledge gained from the high surface area nanostructured spinel oxide catalysts has been transferred to the fabrication of active catalyst/current collector assemblies. Specifically, cobalt oxide nanowire array has been directly grown on stainless steel mesh, a typical current collector used for zinc-air batteries. This unique active electrode assembly design greatly simplified battery architecture and the preparation steps required to produce a rechargeable air electrode, which usually involve physical deposition techniques such as spray-coating to deposit as-synthesized catalysts on gas diffusion layers. During this step, catalyst is mixed with ancillary materials such as carbon black and polymer ionomer, which corrode during battery charging. The direct coupling of active cobalt oxide catalyst onto the current collector completely eliminated the use of any additional material, and a gas diffusion layer was simply attached to the active assembly to form a rechargeable air electrode. Without any corrosion, the advanced electrode has demonstrated a remarkable durability during rechargeable zinc-air battery testing, lasting over 600 hours of operation, which has never been reported in the literature.

There are still a plenty of opportunities to further leverage the knowledge and experience gained from this thesis work to improve the performance of electrically rechargeable zinc-air batteries. For example, the cobalt oxide nanowire arrays can be doped with other metals such as nickel and manganese to precisely tune the bi-functional catalytic activity depending on specific requirements for the battery application. Also, the idea of high surface area nano-carbon support can be used to fabricate an interfacial layer between the cobalt oxide array and stainless steel mesh to improve charge transfer during the reactions. Graphitized carbon, such as graphene nanosheets and carbon nanotubes, that are stable in rechargeable zinc-air battery conditions are great candidates for this purpose and is likely to significantly improve both the activities of ORR and OER.

ACKNOWLEDGEMENTS

First of all, I would like to thank my supervisor, Professor Zhongwei Chen, for his consistent support and encouragement throughout my graduate studies. Also, I would like to thank all of the outstanding colleagues that I had opportunity to work with at the University of Waterloo as I learned something new from every single one of you, not to mention I made some great friends along the way including the Chen Lab and N2L members.

I would also like to thank my Ph.D. thesis examining committee, including Professor Aiping Yu, Professor Eric Croiset, and Professor Xianguo Li from the University of Waterloo, and Professor Wei Tong as my external examiner from Lawrence National Berkeley Laboratory for their time and contributions during this important process.

During my 4th year, I had an opportunity to conduct research at California Institute of Technology as a visiting scholar for a half year in Professor Nate Lewis' research group. It was my pleasure and honour working with Professor Lewis and the catalyst team. Special thanks goes to Daniel Torelli and Dr. Sonja Francis for sharing your knowledge and having discussions with me during my stay.

I also would like to acknowledge my friends and family for all their unconditional love and support, which really helped me stay on track during the difficult times of my Ph.D. studies. I would not have been able to make it without you all.

Finally, I would like to mention my gratitude to the Natural Science and Engineering Research Council of Canada (NSERC), the Waterloo Institute for Nanotechnology, and the University of Waterloo for their support and funding. They provided excellent research opportunities during my Ph.D., and allowed me to stay focused on research.

Table of Contents

LIST OF FIGURES

LIST OF TABLES

LIST OF ACRONYMS

BET – Brunauer-Emmett-Teller

CNT – Carbon nanotube

CV – Cyclic voltammetry

DDI – Distilled de-ionized water

EDS – Energy dispersive X-ray spectroscopy

EES – Electrical energy storage

ESCA – Electrochemically active surface area

EV – Electric vehicles

GDL – Gas diffusion layer

HWP – Half-wave potential

ND – Nano-disks

NP – Nano-particles

ORR – Oxygen reduction reaction

OER – Oxygen evolution reaction

Pt/C – Platinum on carbon catalyst

PVP – Polyvinylpyrrolidone

RDE – Rotating disk electrode

RHE – Reversible hydrogen electrode

SAED – Selected area electron diffraction

SEM – Scanning electron microscopy

TEM – Transmission electron microscopy

TGA – Thermogravimetric analysis

XPS – X-ray photoelectron spectroscopy

XRD – X-ray diffraction

1. Introduction

1.1 The energy challenge

Increasing fossil fuel prices and environmental issues associated with greenhouse gas emissions have been the main driving force for the development of next generation sustainable energy generation and storage systems. However, the majority of the current energy still comes from combusting fossil fuels, including coal and natural gases, which face depletion at the current rate of being mined and used. Furthermore, burning petroleum in combustion engines for automotive applications has significantly increased anthropogenic emission of carbon, resulting in environmental issues including global warming, rising sea levels, and localized air pollutions. These issues have caused irreversible environmental and ecological damage, and led to unnecessary spending in attempts to manage and regulate further deterioration. Despite this, continuously increasing demand for energy has resulted in geopolitical instabilities especially in the regions rich in natural reserves. To date, the lithium-ion battery technology is the most developed and widely distributed energy storage system for a wide range of applications, including portable electronics, electric vehicles (EV), and energy storage systems (EES) due to many their advantages over other older technologies such as lead-acid, nickel-cadmium (Ni-Cd) and nickel-metal hydride (Ni-MH) batteries.[1-3] However, one major drawback of lithium ion batteries is that the energy density depends on the amount of active material that can be stored inside the battery due to the nature of the intercalation and de-intercalation battery chemistry.[4] The limitation in the energy density of lithium ion batteries, particular for EV applications, causes “range anxiety” in the buyers even though the driving range has been significantly improved over the past few years. In fact, researchers anticipate that the energy density of lithium ion batteries will continue to improve through the development of high capacity materials such as lithium-rich oxides. In parallel, researchers have recently put significant research efforts in developing electrically rechargeable metal-air batteries that are practically viable and have sufficient energy density to potentially fulfill EV range requirements. In particular, lithium-air and zinc-air batteries have gained tremendous attention as they boast much higher energy densities compared to that of lithium-ion batteries, and are still electrically rechargeable. For instance, electrically rechargeable zinc-air batteries are capable of generating up to 1084 Wh/kg of specific energy density, which is approximately five times that of a lithium-ion battery. Additionally, zinc-air batteries have other notable advantages including abundance of zinc, environmental benignity, and safe battery operations. Similarly, the rechargeable lithium-air battery technology has also recently attracted immense research attention due to the extremely high gravimetric specific energy, but its development has been hampered by limited rechargeability associated with electrolyte decomposition, parasitic chemical reactions, and blockage of porous electrodes by insoluble discharge products.[5] When normalized volumetrically, however, zinc-air batteries have significantly higher energy density (per unit volume) than lithium-air batteries due to much higher atomic density of zinc metal (Figure 1.1).[3] Volumetric energy densities are often considered more important in applications such as EVs, which have limited space for battery installation. The high energy density of metal-air batteries in general is owing to the fact that oxygen is used as one of the main battery reactants, which is available virtually unlimited in ambient air. In contrast, lithium-ion batteries must carry the fuel (intercalation compounds) inside the battery, the amount of which is limited by the size of the battery.

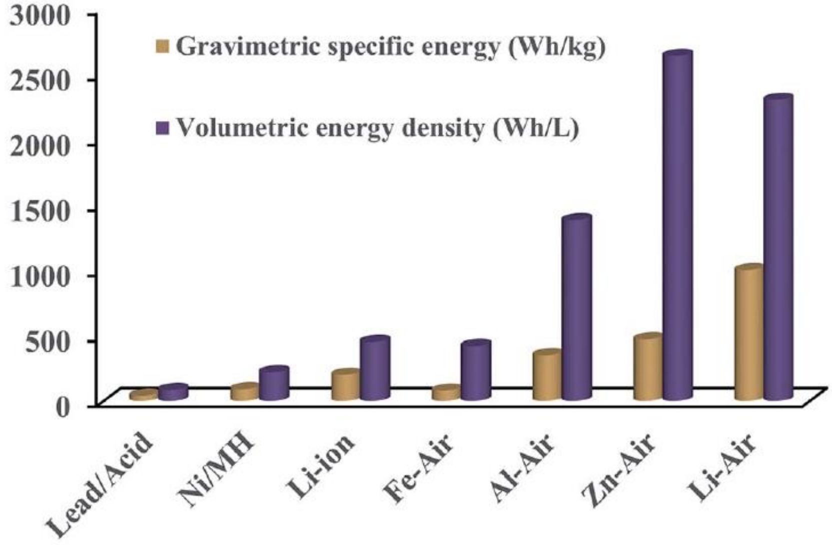

Figure 1.1 Practical gravimetric specific energy and volumetric energy density of rechargeable battery technologies. Reproduced in adapted form from ref. 6 with permission from the Royal Society of Chemistry.

In order for rechargeable zinc-air batteries to work, however, two electrochemical reactions, namely oxygen reduction reaction (ORR), and oxygen evolution reaction (OER), must be sufficiently catalyzed as these reactions occur at very slow rates. The main technical challenge for making rechargeable zinc-air batteries practically viable is therefore on the development of highly active ORR and OER facilitating electrocatalysts, which must sufficiently lower the activation energies so that the reactions progress at reasonable rates.[7] Currently, platinum and its alloy based electrocatalysts are used in fuel-cells to facilitate ORR,[8-13] while iridium-based electrocatalysts are used in electrolyzers to facilitate OER.[14-16] However, these catalysts are made of precious (noble) metals, which are scarce due to limited reserves around the world, making them prohibitively expensive for use in day-to-day applications. [17,18] These catalysts are certainly not viable for large-scale deployment of rechargeable zinc-air batteries for EVs and EES. Moreover, the state-of-the-art platinum on carbon (Pt/C) catalyst is known to degrade during the electrochemical reactions via various degradation pathways including dissolution and agglomeration, resulting in catalytically active site deactivation due to structural and chemical changes.[19-21] In addition, Pt/C is only mono-functionally active towards ORR, which makes it unsuitable for rechargeable applications.[22] Other less expensive precious metal based catalysts (i.e. palladium, iridium, ruthenium, etc.) have also been studied as potential air electrode catalysts, but there is always some degree of performance sacrifice compared to Pt/C which makes them unattractive despite the cost savings.[11] Perhaps most importantly, the precious metal based catalysts are ill-suited for rechargeable applications because they are mono-functionally active towards only of the two oxygen reactions. These issues clearly indicate that the development of rechargeable zinc-air battery technology is currently bottlenecked by the lack of practically viable bi-functional oxygen electrocatalysts, which is one of the main research focuses in the energy and electrocatalyst communities, including the work presented in this thesis. Prior to the discussion of electrocatalyst systems investigated in this thesis, however, the following sections will cover necessary background information on the structure of rechargeable zinc-air batteries, the battery operation principles, and a brief literature review on bi-functional electrocatalysts.

1.2 Rechargeable zinc-air batteries

As mentioned above, rising energy demands and environmental concerns have led to tremendous research efforts in the development of clean and sustainable energy technologies such as fuel-cells and metal-air batteries. These devices have definitely shown the potential to overcome the energy density limitations of the current energy conversion and storage systems. The type of metal-air battery is identified by the kind of metal used as the anode, which include lithium, magnesium, aluminum, iron, and zinc (Table 2.1). Among these, zinc-air battery is believe to be one of the most promising technology because of the rechargeable nature of zinc-air battery chemistry and the safety of using zinc metal. Despite the current research efforts, other types such as magnesium- and aluminum-air batteries are practically not rechargeable at this stage due to the instability (corrosion) of the metal anode which leads to the passivation of the active metal surface. Lithium-air batteries on the other hand are rechargeable and has much higher theoretical gravimetric energy density, but are limited in terms of cycle life due to the insoluble discharge product formation and parasitic chemical reactions that degrades the air electrode irreversibly. In comparison, reports on zinc-air batteries have consistently demonstrated the potential to generate relatively high energy density along with good electrochemical stability (cyclability) which makes it a very interesting and attractive technology to further explore and investigate.[3]

Table 1.1 Characteristic data of metal-air batteries. Reproduced in adapted form from ref. 23 with permission from Elsevier.

Metal anode	**Electrochemical equivalent of metal (Ah/kg)**	**Theoretical cell voltage with O_2 electrode (V)**	**Practical operating voltage (V)**
Li	3861	3.3	2.4
Ca	1337	3.4	2.0
Mg	2205	3.1	1.4
Al	2980	2.7	1.6
Fe	960	1.3	1.0
Zn	820	1.6	1.1

In addition to zinc being one of Earth's abundant metals, the oxygen drawn from atmospheric air is virtually unlimited in quantity, making zinc-air batteries extremely cost-effective. Recently, techno-economic analysis has predicted the price of rechargeable zinc-air batteries to be approximately a half of the current lithium-ion battery price. Furthermore, other metal-air systems that utilize alkali metals such as lithium, sodium, and potassium as anodes can potentially be very dangerous as they react violently with moisture in the atmosphere. However, zinc is much more stable, which makes zinc-air batteries extremely safe to operate and environmentally benign even compared to commercial lithium-ion and lead acid batteries. More importantly, the fabrication of zinc-air batteries can be done under ambient conditions, while metals such as lithium and sodium require an insert atmosphere (such as in glovebox) for handling and fabricating batteries. Practically speaking, this makes the mass production of zinc-air batteries that much more inexpensive and scalable. In fact, primary (non-rechargeable) zinc-air batteries have existed commercially for hearing aids and small medical devices (Figure 2.1). The battery which is sealed with a sticker operates by removing it to allow oxygen in the atmosphere to diffuse and react with active zinc material inside the battery. The active catalytic ingredient which facilitates the ORR during the battery discharge is typically manganese based catalyst, which is only mono-functionally active and is unable to reverse the discharge reaction. This means that in order for zinc-air batteries to be recharged, a bi-functionally active catalyst is required to facilitate both the ORR and OER over the same catalytically active surface. The proposed research, therefore, aims to develop cost-effective, and highly active and durable bi-functional catalysts through tailored composition and nanoscale morphology synthesized by facile and industrially scalable techniques. The rechargeable zinc-air battery operation will be demonstrated using the developed bi-functional catalyst incorporated into an advanced air electrode design with enhanced performance and cycle life.

1.3 Operation of an electrically rechargeable zinc-air battery

The electrochemical reactions that occur at the rechargeable air electrode (the cathode during battery discharge), and metallic zinc anode are very well known and have been studied extensively in the past. This is because the ORR and OER that occur at the air electrode are identical to the reactions of a fuel-cell and water electrolyzer, respectively, while zinc oxidation that occurs at the anode is identical to the anode reaction of nickel-zinc and silver-zinc batteries. A rechargeable zinc-air battery operates by combining these half reactions as shown in the schematic illustration below (Figure 1.3), and is often called zinc-air fuel-cells due to the similarities. Specifically, during discharge, electrons generated at the metallic zinc anode travel through an external load then reach the air electrode, forming zinc ions at the anode which are released into the electrolyte. At the air electrode, oxygen in the atmosphere enters through the pores by diffusion is electrochemically reduced by combining with the electrons from the anode, releasing hydroxide ions into the electrolyte. The hydroxide ions then form soluble zincate species by combining with the zinc ions in the electrolyte as the discharge product. Notably, the electrochemical reduction of oxygen occurs at the three-phase reaction site where gas (oxygen), liquid (electrolyte), and solid (electrocatalyst) meet. During battery charging, the electrochemical processes are reversed, and oxygen is evolved at the air electrode, while zincate ions in the electrolyte is reduced back to the zinc anode.[3] This charging process occurs with an electrical input from some source as the driving force, and is unique to “electrically” rechargeable batteries which is absent in other forms of rechargeable zinc-air batteries such as mechanically rechargeable and flow electrolyte zinc-air batteries. Mechanical zinc-air batteries are recharged by replacing the used (discharged) electrolyte and zinc anode with a fresh set, recharging the battery “instantaneously”. However, mechanically recharging requires a complex cartridge battery design and the used materials must be recycled elsewhere. A flow electrolyte zinc-air batteries on the other hand consist of an external reservoir of zinc slurry/electrolyte mixture that is fed to the battery through a pump system at a controlled rate, which allows the battery to be discharged "infinitely" as long as the used zinc slurry returns to the reservoir is recycled (recharged) through a separate process and introduced back into the loop. In comparison, the main advantage of an electrical rechargeable zinc-air batteries is that the battery architecture can be greatly simplified and no external "fuel" reservoir or infrastructure to recharge/recycle the used battery components are needed, which makes it very applicable to a wide range of applications. However, there are a set of technical challenges of electrically rechargeable zinc-air batteries which must be address before successful introduction to the market, which will be discussed in the later parts of this thesis.

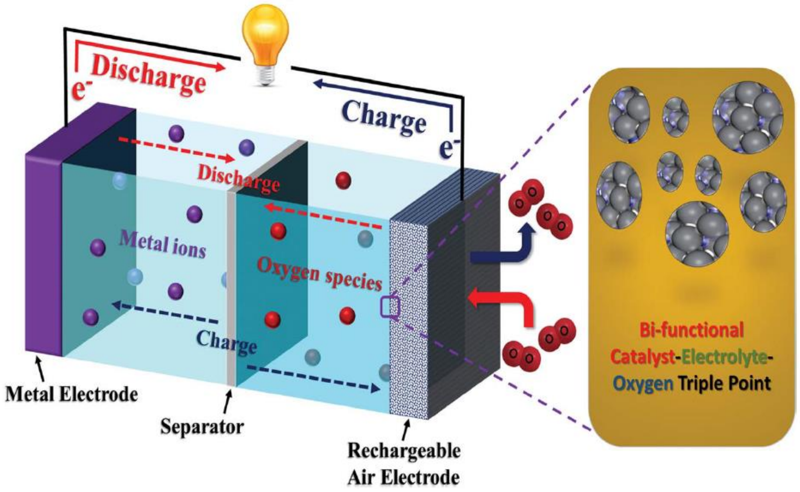

Figure 1.2 Schematic illustration of the operating process of a rechargeable zinc-air battery. Reproduced in adapted form from ref. 6 with permission from the Royal Society of Chemistry.

1.4 Structure of Rechargeable Zinc-Air Batteries

The structure of a rechargeable zinc-air battery is relatively very simple compared to the aforementioned mechanical and flow electrolyte systems which is a major advantage for space confined applications. An electrically rechargeable system typically consists of an air electrode (the cathode during discharge), zinc anode, aqueous electrolyte, and separator. The air electrode is further divided into gas diffusion layer and catalytically active layer which will be discussed in the section below. Currently in the laboratory research scale, a manually machined plastic battery housing is typically used to fabricate rechargeable zinc-air batteries such as in this work, but other forms of the battery including cable-like[24] and flexible[25] types have been reported in the literature. The battery architecture engineering is out of scope of this thesis as the emphasis is on the development of highly active catalyst materials for the air electrode, but the same engineering methodologies can be applied here to fabricate novel battery types.

1.4.1 Zinc anode

Metallic zinc is the anodic reactant of a zinc-air battery, which forms soluble zincate ions, $Zn(OH)_4^{2-}$, inside the electrolyte over the course of discharge. Some zincate ions further decompose to inactive zinc oxide species, but the majority plates back to metallic zinc during charge. The formation of zinc oxide is time- and concentration-dependent and its lack of electrical conductivity makes it very difficult to electrochemically reduce back to metallic zinc. Typically, the capacity of zinc anode is improved by increasing the active surface area to maximize the interface between the electrolyte and metallic zinc. For instance, morphology control during the fabrication of zinc anode has been reported in the literature to produce high surface area materials such as zinc flakes, ribbons, and fibers (Figure 1.4). These novel structures have demonstrated improved zinc-air battery performance compared to using a flat-surfaced zinc plate. However, one major downside of increasing the active zinc surface area is that it also increases the area for parasitic reactions such as hydrogen evolution reaction to occur. This reaction which uses active zinc to produce unnecessary hydrogen, $Zn + 2H_2O \rightarrow Zn(OH)^2 + H_2(gas)$, lowers the material utilization for zincate formation during battery discharge which in turn reduces the energy density of the battery. To prevent this, the metallic zinc is sometimes alloyed with other metals such as Hg, Pb, and Cd which exhibit relatively higher overpotential for hydrogen evolution. However the use of these metals are often discouraged due to their toxic nature, and the additional complexity during the formation of alloy with zinc.

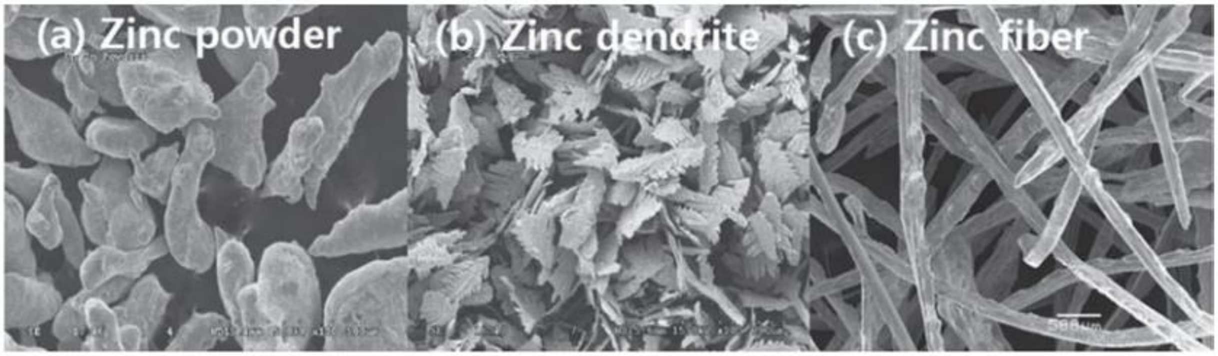

Figure 1.3 Various morphologies of zinc anode: (a) zinc powder, (b) zinc dendrite, and (c) zinc fiber. Reproduced in adapted form from ref. 26 with permission from Elsevier.

In order to successfully develop a zinc-air battery that is electrically rechargeable, not only a bi-functionally active catalyst is required at the air electrode to facilitate both ORR and OER, but a sufficiently reversible metallic zinc surface is required at the anode. However, zinc surfaces in aqueous electrolytes are well-documented to undergo a shape change upon extended charge-discharge cycling of the battery, producing sharp needle-like dendrite structures. The formation of zinc dendrites can be detrimental to the lifetime of a zinc-air battery since an uncontrolled growth can result in a short with the air electrode inside the battery.[27] Furthermore, as mentioned before, zinc oxidation during discharge produces zincate ions which dissolve into the electrolyte. However, once zincate ions reach a saturation point in the electrolyte, they decompose to form a solid white zinc oxide, which is electrically insulating. Often times, zinc oxide deposits over the surface of active zinc anode, significantly reducing the capacity and cycle life of the battery. The saturation of zincate ions in aqueous electrolyte is also time-dependent, so it is often difficult to predict and control the lifetime of the battery. Further systematic research activity is required to understand the exact surface chemistry and the behaviour of active zinc species in aqueous electrolytes to ultimately achieve highly active and durable electrically rechargeable zinc-air batteries.

1.4.2 Separator

The separator in a rechargeable zinc-air battery is usually a microporous polypropyelene membrane, sometimes with a surfactant coating for rapid wetting of the electrolyte. It is electrically insulating and mechanically strong enough to act as a physical barrier against potential zinc dendrite growth and penetration mentioned above. Also it allows the movement of hydroxide ions between the air electrode and the zinc anode during the electrochemical oxygen reactions.[28] A separator should be chemically stable in aqueous electrolytes, usually highly alkaline potassium hydroxide solutions, and inert to electrochemical oxidation so that it remains unchanged and intact during battery cycling. Other forms of separators that satisfy the requirements of a rechargeable zinc-air batteries are polyethylene, polyvinyl alcohol, and polyolefin membranes as they also allow hydroxide ion movement, and are mechanically robust to prevent zinc dendrite penetration. [29-33] The work presented in this thesis use Celgard 5550, a typical microporous polypropylene membrane used for rechargeable zinc-air batteries.

1.4.3 Electrolyte

As mentioned above, rechargeable zinc-air batteries use an aqueous solution as the electrolyte. Usually, alkaline electrolytes are used because zinc is much more stable than in acidic electrolytes where zinc would readily oxidize. Typical alkaline electrolytes used in zinc-air batteries are potassium hydroxide, and sodium hydroxide.[34] Potassium hydroxide is more widely used as it exhibits superior ionic conductivity of K^+ (73.50 $\Omega^{-1}cm^2$) compared to Na^+ (50.11 $\Omega^{-1}cm^2$).[35] In fact, most studies reported in the literature use 6 M potassium hydroxide solution as the electrolyte, which exhibits sufficiently high ionic mobility and relatively low solution viscosity. The main drawback of using alkaline electrolytes is the accumulation of carbonate species due to the reaction of carbon dioxide in the air with the hydroxide ions in the electrolyte.[23] This reduces the concentration of hydroxide ions needed for discharging the battery, which leads to a lowered cell capacity. Additionally, the accumulated carbonate species in the electrolyte precipitate inside the pores of the air electrode preventing oxygen to further diffuse into the reaction sites. In attempts to circumvent this, some reports use a "purified" air using a selective membrane that is only permeable to oxygen to feed to the air electrode. However, all rechargeable zinc-air batteries evaluated in this thesis used ambient air (unpurified) to emulate real usage situations and emphasize of the durability of the developed battery.

1.4.4 Air electrode

Using oxygen in ambient air as the source of fuel requires the air electrode to be both catalytically active and highly porous. Active catalyst is required to alleviate the large overpotentials associated with ORR and OER, while porous structure is required to allow diffusion of air. Hypothetically, the only consumed reactants during battery discharge are oxygen and zinc metal, which means the lifetime of the air cathode in principle is unlimited. However, due to electrochemical degradation in strong alkaline electrolytes and carbon dioxide impurities in atmospheric air, air electrodes fail over extended cycling resulting in loss of active surface area and leakage of electrolyte. Typically, an air electrode consist of a gas diffusion layer and a catalytic active layer, prepared by laminating the two together with a metal mesh as a current collector[36], as shown in Figure 2.4.

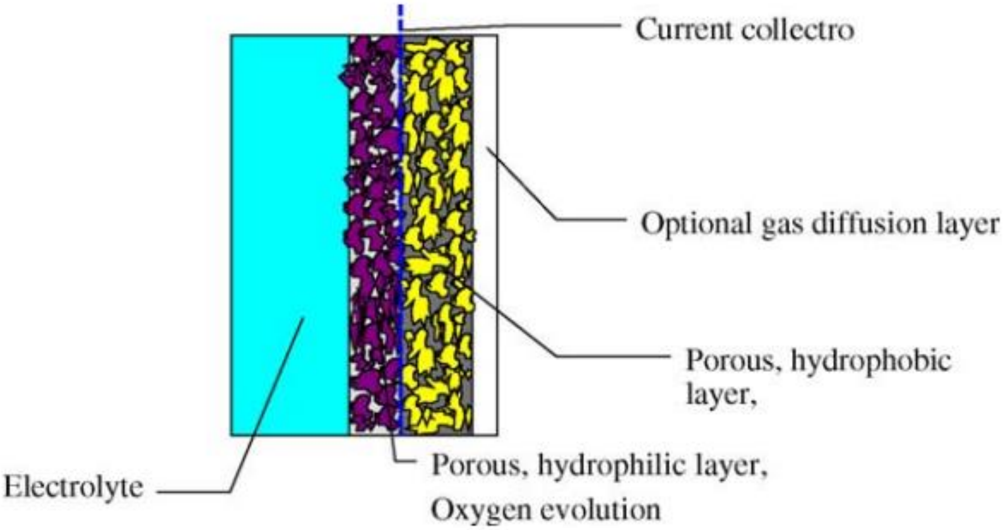

Figure 1.4 Schematic of typical microstructure of an air electrode. Reproduced in adapted form from ref. 23 with permission from Elsevier.

The gas diffusion layer is composed of carbon material on the electrolyte side, and a hydrophobic polymer such as polytetrafluoroethylene (PTFE) on the air side as a wet proofing agent. The PTFE layer allows diffusion of air into the air electrode, while preventing aqueous electrolyte from leaking to the air side. The catalyst layer typically consists of active material mixed with high surface area carbon black and binding polymer to enhance dispersion and enlarge the active surface area. The main drawback of carbon based porous air cathode is that carbon corrosion occurs due to relatively high overpotentials (η) experienced by the electrode during battery charging, as shown in Figure 2.5 of typical charge-discharge loop of a rechargeable zinc-air battery.[23] This again leads to the loss of active catalyst surface area and leakage of electrolyte to the air side, which severely limits the lifetime of the battery.

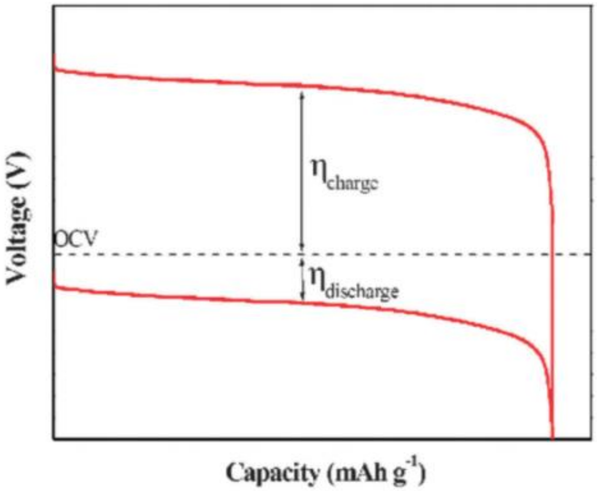

Figure 1.5 Typical charge-discharge loop with corresponding overpotentials of a rechargeable zinc-air battery. Reproduced in adapted form from ref. 37 with permission from the Royal Society of Chemistry.

1.4.5 Oxygen electrocatalyst

Many efforts to overcome the sluggish oxygen electrochemical reactions have been focused on finding highly active bi-functional catalysts to reduce the overpotentials of both ORR and OER. Precious metal based catalysts such as platinum and palladium and their alloys have been shown to exhibit excellent activity for ORR, however, the limited OER activity with high costs associated with these noble metals limit the use in large-scale and practical applications. However, because zinc-air systems utilize alkaline solutions instead of acidic electrolytes, which allows replacement of the precious metals with those of transition metal oxides such as spinels, perovskites, pyrochlores and their mixed oxides as efficient bi-functional catalysts.[7,23,38-40] Generally, the selection of an appropriate electrocatalyst involves a compromise between electrocatalytic activity, thermodynamic stability, corrosion resistance, fabrication and materials cost, and long term stability. These properties can be tuned by changing the composition and geometry of the catalyst. The composition is directly related to electronic properties of the catalyst, which determines the strength of surface-intermediate bonds, hence the electrocatalytic activity, while the geometry is related to the actual surface areas, and active site density, which can be controlled by the catalyst morphology. This proposed research plans to address both of these factors through the synthesis of mixed metal oxide (compositional) having specific nanoscale morphology (geometry), which is further explained in the later chapter.

1.5 Oxygen Electrochemical Reactions

The two main reactions that govern the operation of a rechargeable zinc-air battery are ORR and OER, which correspond to discharge and charge processes of the battery. These reactions must be catalyzed due to the slow kinetics, as mentioned previously, with the use of bi-functional catalysts. The ORR in an air cathode proceeds in several steps: oxygen diffusion from the atmosphere to the catalyst surface, oxygen absorption on the catalyst surface, transfer of electrons from the anode to oxygen, weakening and breaking of the oxygen bond, and the removal of the hydroxide ions from the catalyst surface to the electrolyte.[41] The OER involves the reverse process of the ORR, however, it is very complicated and difficult to describe due to its strong irreversibility as the reaction involves a series of complex electrochemical reactions with multi-step electron-transfer processes.[23,42,43] The following sections discuss the mechanisms of ORR and OER in further detail.

1.5.1 Oxygen reduction reaction (ORR)

The two types of classical oxygen catalysts are metals and metal oxides, and the mechanism of the ORR using these catalysts have been intensively studied. For metal catalysts, such as platinum, a four-electron pathway or a two-electron pathway may proceed for the ORR, depending on the type of oxygen adsorption.[42,44] There are two adsorption types, bidentate O_2 adsorption (two O atoms coordinate with the metal), and end-on O_2 adsorption (one O atom coordinate perpendicularly to the metal) as shown in Figure 2.6, which leads to the direct four-electron pathway, and the two-electron pathway, respectively.

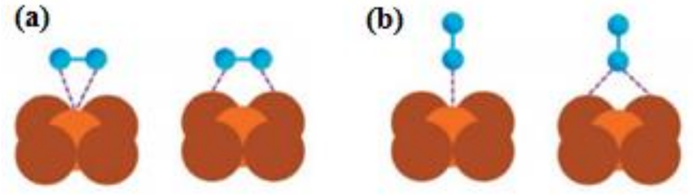

Figure 1.6 O_2 adsorption models on catalyst surfaces: (a) bidentate O_2 adsorption, (b) end-on O_2 adsorption. Reproduced in adapted form from ref. 45 with permission from the Royal Society of Chemistry.

The reactions of the bidentate adsorption are as follows:

$O_2 + 2H_2O + 2e^- \rightarrow 2OH_{ads} + 2OH^-$

$2OH_{ads} + 2e^- \rightarrow OH^{2-}$

Overall: $O_2 + 2H_2O + 4e^- \rightarrow 4OH^-$

For the end-on adsorption, the reactions are as follows:

$O_2 + H_2O + e^- \rightarrow 3OH^-$

$OH_{2,ads} + e^- \rightarrow OH_2^-$

Overall: $O_2 + H_2O + 2e^- \rightarrow OH_2^- + OH^-$

The above two-electron reaction may be followed by either a further two-electron reduction of peroxide or by chemical disproportionation of peroxide as follows:

$HO_2^- + H_2O + 2e^- \rightarrow 3OH^-$ (peroxide reduction)

Or

$2HO_2^- \rightarrow 2OH^- + O_2$ (peroxide disproportionation)

For metal oxide catalysts, such as spinel Co_3O_4, the ORR reaction pathways at the surface follow the same principle, but with a different charge distribution due to the surface cations of stoichiometric oxides that are not fully coordinated with oxygen atoms. In aqueous electrolytes, anion coordination is completed by the oxygen of a water molecule. Consequently, the reduction of a surface cation by an electron from the external circuit is charge-compensated by protonation of a surface oxygen ligand.[46] The reaction pathway of ORR on a metal oxide surface is as follows:

$2M^{m+}—O^{2-} + 2H_2O + 2e^- \rightarrow 2M^{(m-1)+}—OH^- + 2OH^-$

$O_2 + e^- \rightarrow O_{2,ads}^-$

$2M^{(m-1)+}—OH^- + O_{2,ads}^- + e^- \rightarrow 2M^{m+}—O^{2-} + 2OH^-$

The ORR pathways and mechanisms may vary depending on the catalyst used and its electronic structure. For instance, the degree of σ* orbital and the metal-oxygen covalency has influence on the competition between O_2^{2-}/OH^- displacement and OH^- regeneration on the surface of transition metal ions as the rate-determining steps of the ORR. Hence, correctly tuning the electronic structure of metal oxide catalysts by optimization of the composition is crucial for obtaining high performance catalyst.[47]

1.5.2 Oxygen evolution reaction (OER)

The OER pathways and mechanisms are relatively complex. Generally, oxygen is evolved from an oxide phase, rather than a bare metal[23,46], which means the mechanisms may vary depending on the catalyst having different site geometry of metal cations. The multi-valence characteristic of transition metal ions is important for OER because the reaction is induced by the interaction between the metal ions and oxygen intermediates which leads to the formation of a bond by changing in the valence state. The site geometry of metal cations changes the adsorption energy of the oxygen species, which determines the kinetics of OER. For a transition metal oxide catalyst containing surface reactions $M^{m+}\text{-}O^{2-} = M^{(m-1)+}\text{-}O^{-}$ biased towards the right-hand side, the OER in alkaline electrolyte proceeds as follows:

$$M^{m+}—O^{2-} + OH^{-} \rightarrow M^{(m-1)+}—O—OH^{-} + e^{-}$$

$$M^{(m-1)+}—O—OH^{-} + OH^{-} \rightarrow M^{m+}—O—O^{2-} + H_2O + e^{-}$$

$$2M^{m+}—O—O^{2-} \rightarrow 2M^{m+}—O_2^{-} + O_2$$

Typically, precious metal oxides such as RuO_2 and IrO_2 are known to be highly active towards OER due to low redox potential and high electrical conductivity. However, these precious metal based oxides are very costly and only demonstrated limited ORR activity, insufficient for use as bi-functional catalysts for rechargeable zinc-air batteries. Conversely, much cost effective and strongly bi-functional transition metal oxide catalysts such as Co_3O_4 and $NiCo_2O_4$ have been introduced to show high activities for both OER and ORR with electrochemical stability.

1.6 Bi-functional Catalysts

The charge-discharge efficiency of zinc-air batteries is directly related to the kinetics of ORR and OER, which are intrinsically very sluggish without progressing them at practically viable rates using a bi-functional catalyst. In addition, using a bi-functional catalyst on a single air cathode keeps the battery design and architecture very simple for commercialization. As mentioned previously, alkaline electrolytes used in zinc-air batteries allows not only noble metal based catalysts such as platinum and iridium, but also transition metal based oxides such as spinel and perovskite type oxides. Transition metal oxides are stable and less affected by corrosion in alkaline electrolytes, opening the possibility to utilize a wide range of materials for active and durable rechargeable zinc-air batteries.[48] The following sections discuss two classical types of catalysts, noble metals and transition metal oxides, which can be appropriately used for rechargeable zinc-air applications.

1.6.1 Noble metal-based catalysts

Generally, noble metals such as platinum, palladium, and iridium exhibit only uni-functionality towards either ORR or OER, which are not suitable for rechargeable zinc-air battery applications. For example, commercially available carbon supported platinum (Pt/C) catalyst is known to exhibit excellent activity towards ORR but limited OER activity. Effective bi-functional catalysts based on noble metals have usually been achieved by alloying or hybridizing different metallic components, as shown by the Volcano plot in Figure 2.7. For instance, an air cathode consisting of palladium catalyzed porous nickel have been shown to demonstrate acceptable bi-functional performance, even though it shows poor cycle stability lasting only 50 cycles due to dissolution of palladium.[17] Also, silver and platinum catalysts have shown high discharge performance, but results in dissolution during charge process terminating the battery with limited cycle life. Noble metal oxides such as RhO_2 and IrO_2, and their mixed oxides such as $CoIrO_3$ and $NiIrO_3$ have been reported to show high bi-functional activity and reasonable stability, however, their high costs due to the scarcity of these noble metals impedes wide utilization and commercialization.[23]

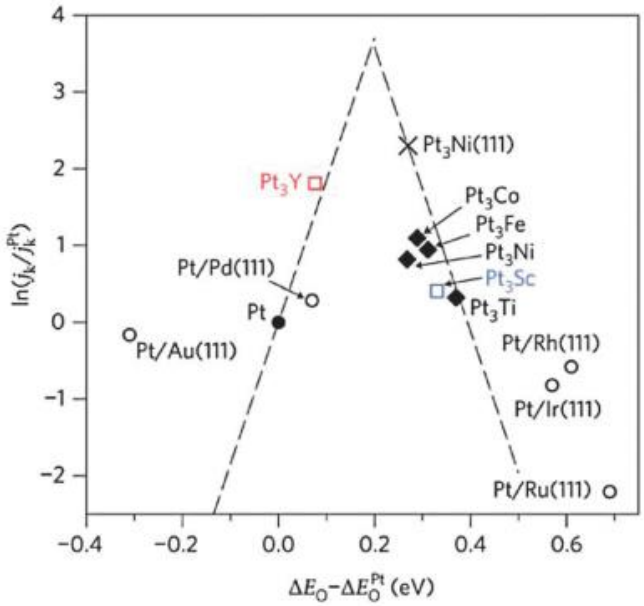

Figure 1.7 Volcano plot of platinum alloys showing theoretical ORR current density as a function of calculated oxygen adsorption energy. Reproduced in adapted form from ref. 45 with permission from the Royal Society of Chemistry.

1.6.2 Non-noble transition metal catalysts

In alkaline electrolytes, non-noble transition metal oxides or mixed transition oxides can be effectively utilized to replace pure noble catalysts with relatively high charge-discharge efficiencies at high current densities and good cycle stability. However, transition metal oxides have intrinsically low electrical conductivity, which impedes transfer of charges during electrocatalytic oxygen reactions, and have limited active surface area, which reduces the number of available reaction sites. However, with a wide range of transition metals available for catalysis of oxygen, the composition, crystal structure, and morphology of transition metal oxides can be properly tailored to obtain a desired electronic structure resulting in good electrical properties and ion mobility. Transition metal oxide catalysts are usually classified into three types depending on their crystal structure, which are perovskites ($LaNiO_3$, $LaCoO_3$, etc), pyrochlores ($Pb_2Ru_2O_{7-x}$, $Pb_2Ir_2O_{7-y}$, etc), and spinels (Co_3O_4, $NiCo_2O_4$, etc.). In particular, spinel type oxides are interesting for facilitating oxygen electrochemical reactions as they exhibit relatively high bi-functionality towards ORR and OER, excellent electrochemical durability, and low electrical resistivity. Additionally, spinel type oxides can be relatively easily synthesized using simple methods such as hydrothermal reaction, and offer morphological flexibility and stability, which are important for nano-engineering the catalyst structure. Among many kinds of spinel oxide, cobalt-based spinels (Co_3O_4 in its simplest form) have been most widely investigated as active and durable bi-functional catalysts that facilitate charge and discharge reactions of a rechargeable metal-air battery.[49] The reason behind this is because the Co ions in Co_3O_4 exist as two different valence states (Co^{2+} and Co^{3+} residing in the tetrahedral and octahedral sites, respectively), which act as donor-acceptor chemisorption sites for reversible oxygen adsorption.[40] This reversible oxygen interaction allows the bi-functional electrocatalysis to happen. Typically, the tetrahedral Co^{2+} ions are known to be the ORR active site, whereas the octahedral Co^{3+} ions that form Co-O bonds are the OER active sites.[50] The exact mechanisms of ORR and OER over spinel oxide surfaces are on-going topics of investigation as they depend on the atomic composition, morphology, and the oxidation state of the active site.

The early studies on bi-functional catalysis using spinel oxides looked at simple Co_3O_4 compositions without doping or catalyst support. For example, Sa et al. demonstrated the synthesis of mesoporous Co_3O_4 using a silica template, and showed that it is possible to achieve high ORR and OER activities with excellent electrochemical durability upon extended cycling test.[51] Later studies on bi-functional catalysis took advantage of compositional flexibility of spinel, demonstrating more complex binary mixed oxide structures, including manganese-cobalt, nickel-cobalt, copper-cobalt, and zinc-cobalt oxides.[52,53] For instance, Cheng et al. demonstrated the synthesis of two different phases of spinel cobalt-manganese nanoparticles at room temperature by reduction-recrystallization method as shown in Figure 2.8.[54] They revealed by electrochemical evaluation that the oxygen electrocatalysis is phase-dependent, showing improved ORR and OER activities with cubic and tetragonal phases, respectively. More recently, Prabu et al. employed a simple electrospinning method to prepare high aspect ratio spinel $NiCo_2O_4$ structures, including porous nano-tubes and nano-rods.[55] These structures were confirmed to demonstrate a smaller overpotential gap between ORR and OER onset potentials than those of benchmark catalysts composed of precious metals such as Pt and Ir. When tested in a rechargeable zinc-air battery, the $NiCo_2O_4$ nanostructures showed very stable charge and discharge voltages with little voltage fading. These examples are just a few from a library of spinel oxide based bi-functional catalysts developed to date with a range of atomic compositions and morphologies. The work presented in this thesis further improves the bi-functional catalytic activity of cobalt-based spinel oxides by engineering the composition and morphology at the nano-scale, and conducting experiments to understand their influence on ORR and OER. Furthermore, as a step forward, this thesis will deal with integration of active bi-functional catalyst into a practically viable rechargeable air electrode assemblies to develop metal-air batteries that are cost- and performance-competitive to other existing energy devices.

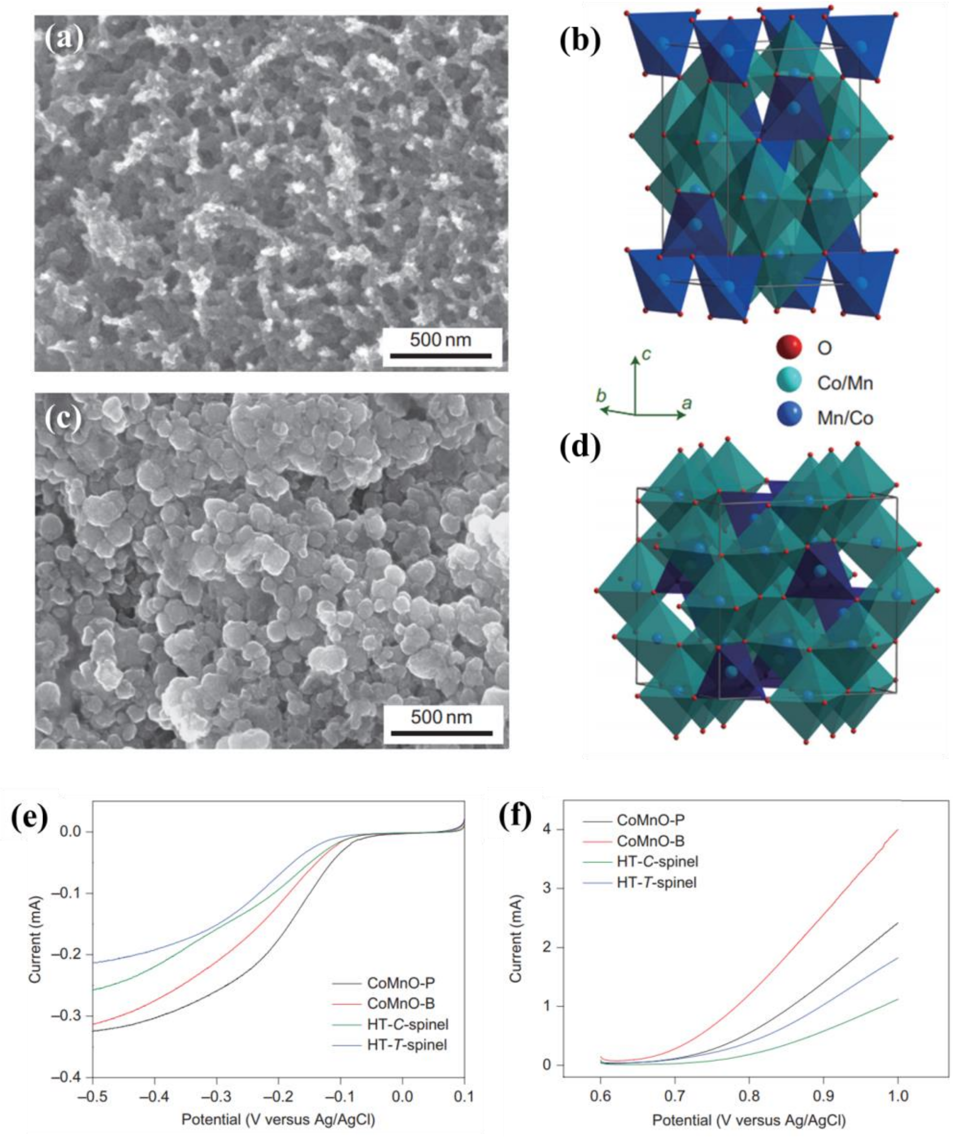

Figure 1.8 SEM images and crystal structures of cobalt-manganese spinel oxides: (a) and (b) tetragonal-phase (RT-t-spinel); (c) and (d) cubic-phase spinel (RT-c-spinel). Voltammograms of the (e) ORR and (f) OER recorded on these catalysts. Reproduced in adapted form from ref. 54 with permission from Nature.

2. Thesis Objectives and Approach

To address the energy challenge mentioned in the introduction, the research conducted for this thesis is focused on the development of highly active and durable bi-functional electrocatalyst systems to facilitate the ORR and OER for electrically rechargeable zinc-air batteries. In terms of catalyst composition, the focus is on utilizing the first-row transition metals, such as nickel, cobalt, and manganese, to synthesize highly cost-competitive non-precious metal catalysts with minimal activity loss. Additionally, facile materials synthesis techniques have been used to fabricate the catalysts with specific nano-scale morphology to expand as much active surface area possible, and facilitate the movement of reactants. To study the bi-functional catalysts developed in this thesis, various physicochemical and electrochemical characterization tools have been used, including realistic rechargeable zinc-air battery prototype fabrication and testing. In overall, the research conducted for this thesis can be divided into three stages as follows.

(i) Design and synthesize active and durable transition metal-based spinel oxide bi-functional catalysts with a high surface area nano-scale morphology by a facile synthesis technique, and conduct physicochemical and electrochemical evaluations.

(ii) Introduce metal substituents and carbon supports to improve electrocatalytic activity and/or stability, and elucidate their roles on potential synergistic enhancements.

(iii) Design and fabricate active catalyst/current collector assemblies for facile integration into single-cell rechargeable zinc-air battery systems, and conduct post-durability analysis to study degradation mechanism and formulate mitigation strategies.

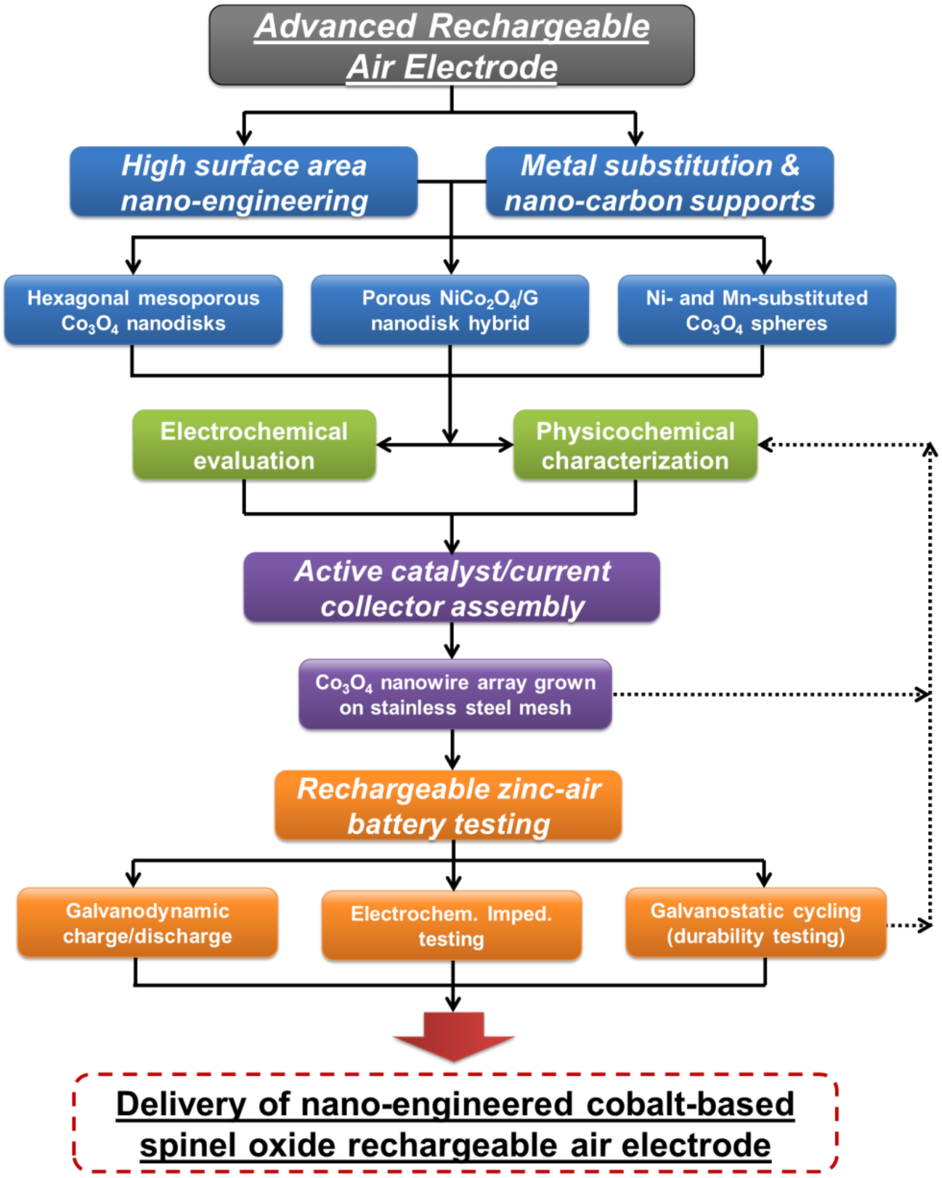

Figure 2.1 Schematic diagram of thesis work flow

2.1 Thesis outline

As provided above, Chapter 1 introduces background information and provides a brief literature review of the work relevant to the bi-functional catalyst development research conducted for this thesis. Chapter 2 provides an outline of research objectives, and how this thesis is organized.

In Chapter 3, background information on various experimental procedures is provided, including physicochemical characterization tools, materials synthesis methods, and device fabrication and testing protocols employed for the completion of the thesis. Chapter 4 starts with an early development of a bi-functionally active catalyst system, mesoporous cobalt oxide hexagonal nanodisks (Co_3O_4 ND), which demonstrated charge and discharge zinc-air battery performance that exceeded those of simple granular nanoparticle Co_3O_4. As an extension of this work, Chapter 5 introduces nickel cobalt oxide hexagonal nanodisks supported on graphene nanosheets ($NiCo_2O_4$/G), which demonstrated electrocatalytic improvements over the previous catalyst. To further study and understand the effects of transitional metal substituents, such as nickel and manganese, on the bi-functional activity and durability, the work in Chapter 6 focuses on the synthesis of self-assembled porous spheres with different atomic compositions and the evaluation of electrochemical activity by both experiment and computational analysis. The technical challenges associated with integrating nanostructured bi-functional catalysts into rechargeable air electrodes is addressed in the work of Chapter 7 by using a synthesis method to directly grow 3-dimensional cobalt oxide nanowire (Co_3O_4 NW) arrays onto a current collector made of stainless steel mesh. This unique active catalyst/current collector assembly was found to demonstrate a remarkable long-term durability as a rechargeable zinc-air battery electrode lasting over 600 hours of charge/discharge cycling. Finally, Chapter 8 summarizes the main conclusions of all research conducted during the PhD program, and outlines suggestions for future work to further progress bi-functional catalyst developments and improve performance and life-time of rechargeable zinc-air batteries.

3. Characterization Techniques

This chapter provides general details and descriptions of characterization techniques used for the completion of the thesis, including both physicochemical and electrochemical evaluation methods. For more details on specific nanomaterials synthesis procedures and electrochemical performance methods/parameters, the reader is directed to the Experimental Methods section included in each of the next four following chapters.

3.1 Physicochemical characterization tools

3.1.1 Scanning electron microscopy (SEM)

Scanning electron microscopy (SEM) is an important characterization technique which allows high resolution inspection of the morphology of a material in the micro and nanoscale. Unlike an optical microscope which uses a visible light as the source of interaction in creating magnified images, SEM utilizes an electron beam focused on the sample's surface to characterize its topology and the sample's morphology. This technique is particularly useful as the electron source has an extremely small wavelength, which allows production of high resolution images of nanostructured materials. The electron beam is focused on the sample by a set of electromagnetic lenses similar to optical lenses in a light microscope. Upon interaction of the electron beam with the sample's surface, secondary and backscattered electrons are either generated or reflected, which are then captured by the detector above the sample. The focused electron beam is scanned over an area in a raster fashion, and the detected electrons are converted into an electric signal and processed by a computer to produce the final image.

3.1.2 Transmission electron microscopy (TEM)

Transmission electron microscopy (TEM) is one of the essential physical characterization techniques, which allows direct visualization of the sample's morphology similar to SEM. TEM also utilizes an electron beam as the source to create high resolution images. However, unlike in SEM which detects backscattered or reflected electrons above the sample, TEM detects electrons which are transmitted through a thin sample which are then converted to an electric signal to produce the final image. This allows TEM to resolve features in the atomic range including the visualization of crystal orientation in ordered metal or transition metal oxide samples.

3.1.3 Energy dispersive x-ray spectroscopy (EDS)

Energy dispersive X-ray spectroscopy (EDS or EDX) is an elemental analysis technique which allows identification and quantification of the sample's chemical composition. This technique is commonly coupled to an SEM or TEM system to be conducted simultaneously with microscopic analysis. The EDS signal is obtained by detecting x-rays emitted from the sample during the interaction with the electron beam. The binding energy of the emitted x-ray is specific to each element which provides blue print for elemental identification. A typical EDS results is displayed as a spectrum with x-ray counts versus binding energy to show various elements found in the sample. The EDS can also be used to create elemental "maps", which shows the distribution of localized elements over a selected area of the sample. The maps show varying intensities depending on the amount of the localized elements. This is particularly interesting for hybrid catalysts consisting of organic and inorganic constituents to clearly identify the elements and their distribution in a sample.

3.1.4 X-ray diffraction (XRD)

X-ray diffraction (XRD) is a versatile characterization technique which allows the determination of crystal structure. The x-rays from the source interact with the sample to produce diffraction patterns at the angles corresponding to specific crystal planes. The x-ray source is swept over a range of angles and the diffracted x-rays at specific angles are collected and processed by the detector. The angle of diffraction is related to the specific crystal orientation of the sample by Bragg's law as shown by Equation (1) below,

$$2d\sin\theta = n\lambda \qquad (1)$$

where n, λ, d, and θ represent the order of the spectrum (any integer), the wavelength of the X-rays, the spacing between diffracting planes, and the incident angle, respectively. The diffraction pattern at specific angles obtained by XRD can be compared to the theoretical diffraction pattern calculated by the crystal planes to help identify the material. Having said this, XRD patterns cannot be produced by amorphous materials as they do not have ordered crystal planes that interact with X-rays to produce diffracted patterns. In this research, XRD is used to identify the developed catalysts and confirm their crystal structures.

3.1.5 X-ray photoelectron spectroscopy (XPS)

X-ray photoelectron spectroscopy (XPS), also known as electron spectroscopy for chemical analysis (ESCA), is a surface elemental composition characterization technique which allows the user to identify and quantify elements present at the surface up to a probing depth of 5 nm.[56] Additionally, XPS allows investigation of electronic (oxidation) states of an element making prediction of empirical chemical formula possible. This technique works by irradiating X-ray on the material under investigation to induce emission of electrons by photoelectric effect. The detected kinetic energy and the number of electrons from the samples surface up to 10 nm in depth are analyzed to produce a pattern with intensity versus binding energy similar to that of XRD. The specific binding energy of the electron acts as the blue print for identifying the composition of the sample with the intensity corresponding to the quantity of elements. For the purpose of this research, XPS is used to identify and quantify the elements in the developed catalyst as well as their electronic states.

3.1.6 *Brunauer-Emmett-Teller (BET) surface analysis*

This characterization technique a type of gas sorption technique which relies on physical adsorption and desorption phenomena of gases onto surfaces and pores of a solid material to quantify the amount of specific surface area and to analyze the nature of surface/pores. Typically inert gas such as nitrogen and argon are used so that they do not chemically react with the surface being investigated. Gas sorption analyses work on the basis that the adsorption occurs on well-defined surfaces, the adsorbed layers do not interact with each other, and the number of layers adsorbed goes to infinity at the saturation pressure.[57] Generally, the BET surface analysis is useful for materials development as it allows to describe and quantify the nature of surface and pores. For instance, the shape of the curve obtained from the adsorption-desorption isotherm is classified into several types that indicate different surface features and porosity of a material. In particular, nanostructured and/or porous catalyst studies rely on this surface analysis tool since all electrochemical reactions that are facilitated are surface reactions, including the oxygen reduction and oxygen evolution reactions. Increasing the specific surface area of an electrocatalyst through materials and nano-engineering is one of the main goals of the research since catalytic active sites exposure can be greatly enhanced. It is then important to be able to accurately measure and describe the catalyst’s surface to elucidate the effect of nanostructured materials design on the activity and durability of the catalyst.

3.2 Half-cell electrochemical evaluation

Half-cell electrochemical evaluation of the catalysts developed in the thesis is conducted to observe and understand electrochemical behaviours and catalytic activities. This is particularly important for transition metal oxide based catalysts as the surface active sites undergo Faradaic reduction and oxidation reactions within operating potential range of an electrical rechargeable battery. For example, the redox of surface species allows understanding of the nature of active sites depending on the amount of current measured and the potential at which the redox occurs. Similarly, the oxygen reduction and oxygen evolution activities of the catalysts are evaluated based on the current generated at certain potentials, which will be explained in detail later. Specific half-cell testing preparation, procedure, and parameters depend on the catalyst under investigation. This includes the catalyst loading, catalyst to carbon to ionomer (polymer binder) ratio, type of solvent, etc. The activity of the catalysts developed in the thesis are compared based on the best possible half-cell activity obtained from optimizing the mentioned variables, but there are no dramatic differences as they are all spinel oxide based materials. Testing each catalyst at its best possible condition is generally done in the literature, particularly when comparing different types of catalysts (precious metal based catalyst for instance), since they would be used at their optimal activity level in practical applications. For more specific details, the reader is guided to the Experimental Methods section of the following chapters.

3.2.1 Linear sweep voltammetry (LSV) and cyclic voltammetry (CV)

Cyclic voltammetry (CV) is a potentiodynamic electrochemical measurement technique used to analyze the redox properties of the sample. CV measurements are done by sweeping the potential of the working electrode linearly at a certain scan rate within a desired potential window. The measured current over a potential window is characteristic of the material's redox property, which can be compared to the theoretical values calculated by the standard potentials. This enables identification of redox reactions in a catalyst and degree of reversibility. In this research, CV is used to confirm the potentials at which ORR and OER occur as well as to identify redox pairs of transition metal oxide catalysts.

3.2.2 Rotating disk electrode (RDE) testing

The half-cell electrochemical testing via rotating disk electrode (RDE) is a fundamental technique widely used to analyze the electrochemical reactions of a catalyst. The RDE works as a hydrodynamic working electrode connected to a rotating rod to allow mass transport of active species by convection. The speed of the rotating rod is systematically controlled to create a set of data for the analysis of catalytic reaction pathway. RDE, which consists of conductive glassy carbon embedded in an insulating outer layer, is loaded with an active catalyst layer. Typically, active catalyst mixed with 0.3 wt. % Nafion binder dissolved in ethanol is coated on the glassy carbon area of the RDE with a desired amount of catalyst loading. In a three electrode electrochemical setup, saturated calomel electrode (SCE) and platinum wire are used as reference and counter electrodes, respectively. In this research, the RDE setup is used to conduct linear sweep voltammetry measuring current over a range of applied voltage at rotation rates of 100, 400, 900, and 1600 rpm. This elucidates the reaction pathway of ORR by determining the number of electrons transferred during the catalytic reaction, allowing quantitative analysis of the ORR kinetics of the catalyst. The number of electrons transferred is calculated by creating a Koutecky-Levich plot based on the following equations.[58]

$$\frac{1}{\mathrm{i}} = \frac{1}{\mathrm{i_k}} + \frac{1}{\mathrm{i_d}} \qquad (2)$$

$$\mathrm{i_k} = \mathrm{nFkC_o} \qquad (3)$$

$$\mathrm{i_d} = 0.62\mathrm{nFD_o^{2/3}}\upsilon^{-1/6}\mathrm{C_o}\omega^{1/2} \qquad (4)$$

where i_k and i_d is the kinetic current and limiting current, respectively, F is the Faraday constant (96 485 C mol^{-1}), k is the rate constant for ORR (m s^{-1}), D_o is the diffusion coefficient of O_2 (1.9 x 10^{-5} cm^2 s^{-1}) in 0.1 M KOH, υ is the kinematic viscosity of 0.1 M KOH (0.01 cm^2 s^{-1}), C_o is the concentration of O_2 in the electrolyte (1.1 x 10^{-6} mol cm^{-3}) and ω is the angular frequency of the rotation (rad s^{-1}). By linearly fitting the Koutecky-Levich plot drawn i^{-1} versus $\omega^{-0.5}$, one can use the slope of the best fit line and Equation (4) to deduce the number of electrons transferred, n, during the ORR as shown in Figure 3.1.

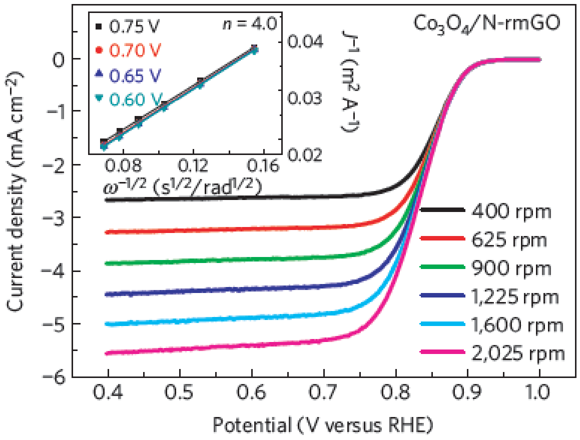

Figure 3.1 RDE measurements of Co_3O_4 hybrid catalyst in O_2-saturated 0.1 M KOH electrolyte at different rotation rates with the inset showing corresponding Koutecky–Levich

plot at various potentials. Reproduced in adapted form from ref. 20 with permission from the Royal Society of Chemistry.

3.2.3 Accelerated degradation testing (ADT)

Accelerated degradation testing (ADT) is conducted to investigate the durability of the catalyst in a shortened period of time. The testing is done by conducting CV in the potential range that includes ORR and OER in an Ar-saturated electrolyte for a repeated number of cycles up to 3000 at electrolyte temperature up to 50 ^{o}C. The durability of the catalyst is simulated by the repeated cycles and the degree of performance degradation is determined by comparing the activities of ORR and OER before and after ADT.[21]

3.3 Single-cell rechargeable zinc-air battery performance evaluation

3.3.1 Galvanodynamic charge and discharge

The galvanodynamic technique allows investigation of charge and discharge behaviours of the catalyst being studied in a single-cell zinc-air battery. Briefly, a single-cell zinc-air battery consists of zinc anode and air cathode on each side with 6.0 M KOH alkaline electrolyte and a separator in between the electrodes. The galvanodynamic technique is conducted by increasing the applied current from 0 A up to a desired value with a fixed current rate (A/s), and monitoring the change in the cell potential of the air cathode versus the zinc anode. The polarization curves obtained from this technique are used to identify overpotentials associated with the catalytic oxygen reactions and resistances that arise from the battery operation in a single-cell environment.

3.3.2 Galvanostatic cycling

Galvanostatic cycling is carried out to investigate the durability of the catalyst by applying a repeated cycles of fixed current in alternating polarity for a fixed amount of time, and measuring the cell potential of the battery. A single cycle consists of charge and discharge regimes obtained by applying a fixed current of the same magnitude but opposite polarity and this is repeated for a number of desired cycles to observe any change in the cell potential profile over a certain number of cycles. The time interval for each cycle can be adjusted to simulate either pulse cycling (10 minutes per cycle) or extended cycling (10 hours per cycle). The pulse cycling technique is an excellent diagnostic tool for evaluating the battery's rechargeability by switching the polarity in short intervals, and extended cycling gauges more practical cycling capabilities of the battery. The durability of the catalyst is then determined by the degree of retention of the cell potential over a number of cycles.

3.3.3 Electrochemical impedance spectroscopy (EIS)

Electrochemical impedance spectroscopy (EIS) allows direct analysis of the resistances associated with a single-cell battery operation such as internal resistance, solid-electrolyte interface resistance, and charge transfer resistance. In this research, a hybrid technique is used where a fixed cell potential at which either ORR or OER occurs is applied with AC amplitude ranging from low (10 Hz) to high frequency (1 MHz). The obtained EIS signal is drawn into a Nyquist plot which is then fitted by an equivalent circuit consisting of relevant circuit elements that correspond to the resistances associated with aforementioned single-cell zinc-air battery operation, including the charge transfer resistance which is directly related to the kinetics of the oxygen reactions.

4. Morphologically Controlled Co_3O_4 Nanodisks as Practical Bi-Functional Catalyst

This chapter is reprinted in adapted form from the below article[59] with permission from Elsevier.

D. U. Lee, J. Scott, H. W. Park, S. Abureden, J. Y. Choi, Z. Chen, "Morphologically controlled Co_3O_4 nanodisks as practical bi-functional catalyst for rechargeable zinc–air battery applications", Electrochemistry Communications, 43 (2014) 109-112.

4.1 Introduction

As mentioned previously, the most active catalysts for the ORR and OER are precious metal Pt- and Ir-based catalysts, respectively. However, their prohibitively high costs and electrochemical instability make them not suitable for commercialization of rechargeable zinc-air batteries. One research direction to reduce the precious metal catalyst dependency is to develop highly active and cost-competitive non-precious metal based catalysts and try to minimize the activity sacrifice as much as possible.

As mentioned above, oxide crystals made of the first-row transition metals such as Ni, Fe, Co, and Mn are known to be excellent choice for bi-functional catalysis due to their multi-valent nature. The availability of different oxidation states opens up possibilities for researchers to fine-tune the valency of the active metals at the catalyst's surface to enhance the interaction with oxygen adsorbates and their intermediate species during the oxygen reactions. For instance, it is well known that active Co metals at the surface must sufficiently transition from 3+ to 4+ oxidation states in order to demonstrate high OER activity. For this to occur, a careful catalyst design and synthesis must be done to expose as much active cobalt surface as possible. The knowledge from nanostructured materials engineering has allowed synthesis of various high surface area cobalt oxide materials with unique morphologies such as nano-particles, nano-wires, nano-ribbons, etc. In addition to morphology, the crystal structure of cobalt oxide and the crystal orientation which is exposed to the electrolyte for the reactions are found to be important. As such, various nano-morphologies of cobalt oxide mentioned above are found to be linked with having exposed specific crystal orientation to the electrolyte.

In this present chapter, spinel cobalt oxide with composition of Co_3O_4 synthesized by facile surfactant-assisted hydrothermal reaction method is introduced. The resulting cobalt oxide has been characterized to be in the form of hexagonal-shaped nano-disk (ND) structures. The surfactant polyvinylpyrrolidone (PVP), dissolved in the precursor solution for the hydrothermal reaction has been found to play two important roles. First, it works as a capping agent to facilitate anisotropic growth of spinel cobalt oxide into two-dimensional nanodisks. Second, PVP that was adsorbed on the top and bottom surfaces of nanodisks decomposes during the heat treatment, leaving behind pores in the structure. The porous morphology is particularly interesting for progressing the ORR and OER efficiently because the mass transport can be improved with reactants in the electrolyte flowing through the pores. Nano-structured materials in general have a strong tendency to agglomerate due to high surface energies, but the pores in the nano-disks should help in moving the electrolyte even in the case the nanodisks overlap.

Both the morphology and crystal structure of Co_3O_4 ND satisfy the pre-requisite of a bi-functionally active catalyst for ORR and OER. Its performance has been tested using an air electrode prepared with Co_3O_4 ND in a rechargeable zinc-air battery testing setup. The air electrode was prepared by physically depositing a mixture of Co_3O_4 ND and carbon black onto the gas diffusion layer via spray-coating. This is a widely accepted method also used to fabricate air electrodes for fuel cells. The role of the carbon black is a catalyst support which helps to distribute the active Co_3O_4 ND as uniformly as possible throughout the gas diffusion layer. Also, particularly for catalysts with intrinsically low electrical conductivities such as oxides, carbon black works as conductive linkers that transport charges in and out of the electrode during the reactions. To highlight the advantages of Co_3O_4 ND in a rechargeable zinc-air battery, its performance has been directly compared to that of Co_3O_4 nanoparticles (NP) with random granular morphology. To observe the effects of specific nano-morphology, the composition of both catalysts was kept constant. The specific surface area, which roughly translates to the number of active sites available, was kept constant by utilizing a nano-sized randomly shaped particles as opposed to bulk (micro-sized) particles. The battery testing has reveal that Co_3O_4 ND significantly outperformed the NP counterpart in terms of both charge and discharge voltages over a charge-discharge cycling up to 60 cycles. The details of the experiment and the obtained data are presented and discussed in the following sections below.

4.2 Experimental

4.2.1 Preparation of Co_3O_4 nanodisks

In a typical synthesis, a solution of 10 mL mixture of double deionized (DDI) water and ethanol in a 1:1 volume ratio containing 1.65 g of 24,000 molecular weight polyvinylpyrrolidone (PVP) and 1.252 g of $Co(NO_3)_2 \cdot 6H_2O$ is dissolved by magnetic stirring and bubbled with N_2 for 30 minutes. Then, 0.213 mL of 1.0 M NaOH solution is added drop-wise at a rate of 0.56 mL min^{-1} resulting in color change of the solution from pink to dark blue as the precipitation reaction proceeds. The mixture is transferred to a sealed Teflon-lined autoclave and heated at 120 ^oC for 6 hours. The resulting precipitate is centrifuged three times with DDI water and another three times with acetone at 5000 rpm then freeze-dried for 24 hours. Finally, the obtained black powder is calcined in air at 300 °C for 3 hours to obtain Co_3O_4 nanodisks.

4.2.2 Rechargeable zinc–air battery fabrication and performance testing

The single-cell catalytic activity is tested by fabricating a home-made zinc-air battery and a multichannel potentiostat (Princeton Applied Research, VersaSTAT MC). For the anode and cathode of the battery, a polished zinc plate (Zinc Sheet EN 988, OnlineMetals) and a catalyst-deposited gas diffusion layer (GDL) (SGL Carbon 10 BB, Ion Power Inc.) are used, respectively. The GDL is prepared by spray-coating a catalyst ink consisting of 10 mg of Co_3O_4 nanodisks and 67 µl of 5 wt. % Nafion (LIQUion^{TM} solution, Ion Power Inc.) dispersed in 1.0 ml of isopropyl alcohol. Similarly, Co_3O_4 nanoparticle (Sigma-Aldrich) is spray-coated on a GDL with the same loading as a comparison. After spraying, the electrode is dried in an oven at 60 °C for 1 hour. All electrodes are prepared to achieve a loading of ca. 1.5 mg cm^{-2} with catalytically active surface area of 2.834 cm^2. The gap between the cathode and anode is 1.0 cm. For the electrolyte and separator, 6.0 M KOH and microporous membrane (Celgard 5550) are used, respectively. The battery charge and discharge voltages are measured by the galvanodynamic method scaling the current from 0 to 200 mA at a rate of 5 mA s^{-1}. The charge-discharge pulse cycling is tested by the recurrent galvanic pulse method using an applied current of 50 mA with each cycle consisting of 5 min discharge followed by 5 min charge. Electrochemical impedance spectroscopy (EIS) is conducted by operating the battery at constant cell potential of 0.8 V and alternating current (AC) amplitude of 20 mV with its frequency ranging from 100 kHz to 0.1 Hz.

4.3 Results and Discussion

The Co_3O_4 catalyst consists of two-dimensional nanodisk structures with relatively characteristic hexagonal geometry having an average diameter and thickness of 500-600 and 20-40 nm, respectively **(Figure 4.1a)**. The nanodisk morphology is created by confined growth only into two dimensions using PVP as the capping agent which specifically adsorbs and inhibits growth of certain crystal planes [60]. Some nanodisks are observed to be partly overlapping, which likely creates pathways for effect charge transfer during the electrocatalytic reactions. On the other hand, Co_3O_4 nanoparticles exhibit non-uniform morphologies with a broad particle size distribution of 10 to 100 nm **(Figure 4.1b)**. Co_3O_4 nanodisks exhibit porosity on the two-dimensional surface **(Figure 4.1c)**, which likely enhances active site exposure and mass transport properties. The TEM characterization also confirms two-dimensional nanodisk morphology with surface porosity **(Figure 4.1d)**, and the SAED analysis reveals a pattern that corresponds to spinel crystal structure **(Figure 4.1d, inset)** [61]. In fact, the observed fringes correspond to the (111) *d*-spacing (d = 0.46 nm) of spinel Co_3O_4 **(Figure 4.1e)** [61]. The FFT pattern is also characteristic of the (111) plane of spinel Co_3O_4 **(Figure 4.1e, inset)** [61]. Lastly, XRD patterns show characteristic spinel oxide peaks for both nanodisks and nanoparticles **(Figure 4.1f)** [61].

To emphasize the practicality of Co_3O_4 nanodisks in a real environment, all single-cell battery tests are performed utilizing air in ambient conditions instead pressurized pure oxygen. The charge and discharge battery voltages of Co_3O_4 nanodisks obtained by the galvanodynamic testing clearly show significantly reduced overpotentials at all current densities measured compared to those of Co_3O_4 nanoparticles **(Figure 4.2a)**. Particularly at higher current densities, Co_3O_4 nanodisks significantly outperform the nanoparticles for both charge and discharge, consistent with the conjecture that the nanodisk morphology and partly overlapped interactions

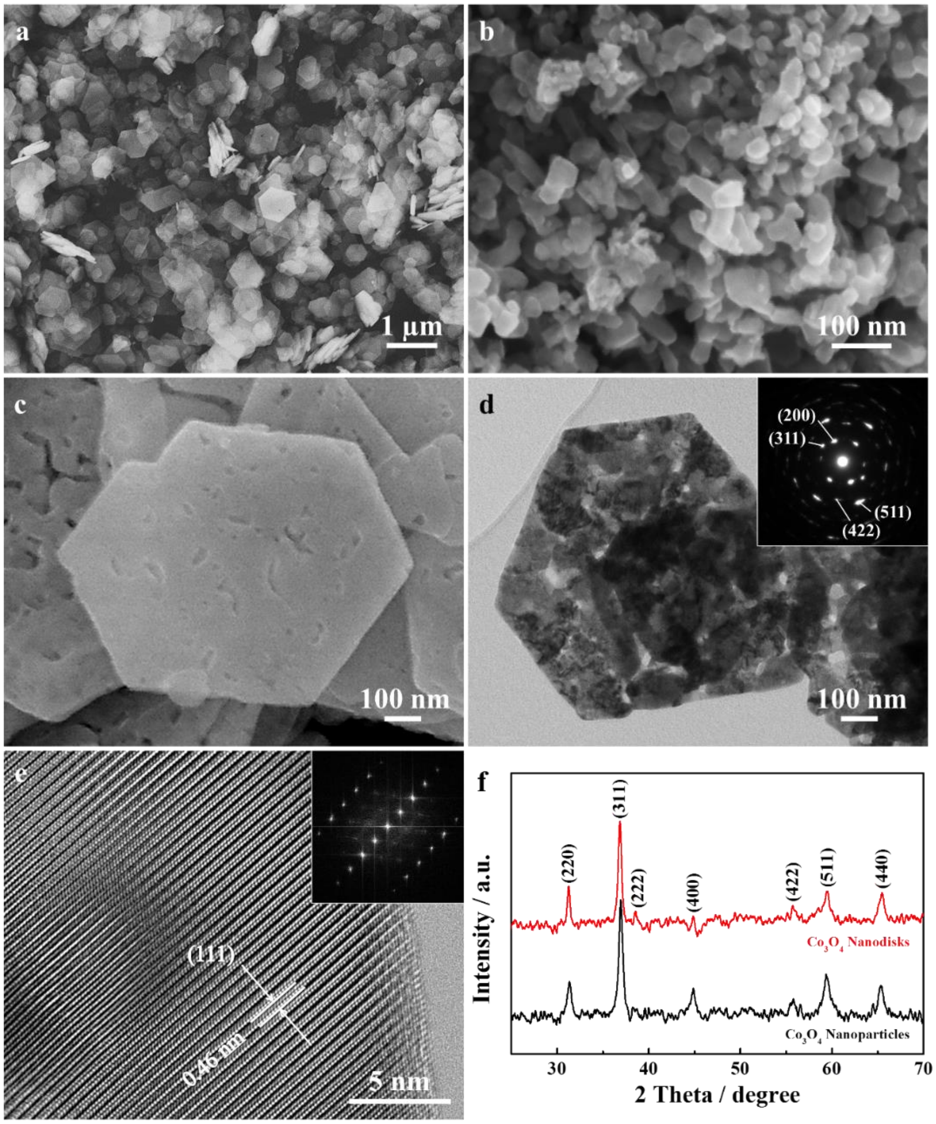

Figure 4.1 SEM images of Co_3O_4 (a) nanodisks, (b) nanoparticles, and (c) surface morphology of Co_3O_4 nanodisks. (d) TEM image of Co_3O_4 nanodisks. Inset: SAED pattern. (e) HR-TEM of (111) crystal plane of Co_3O_4 nanodisk. Inset: FFT pattern. (f) XRD patterns of Co_3O_4 nanodisks (red) and nanoparticles (black). Reproduced in adapted form from ref. 59 with permission from Elsevier.

improve the charge transport properties which in turn mitigates observed overpotentials. In fact, the lower battery resistances of Co_3O_4 nanodisks are directly evaluated from the Nyquist plots by conducting EIS **(Figure 4.2b)**. The Nyquist plot of a single-cell battery modeled by an equivalent

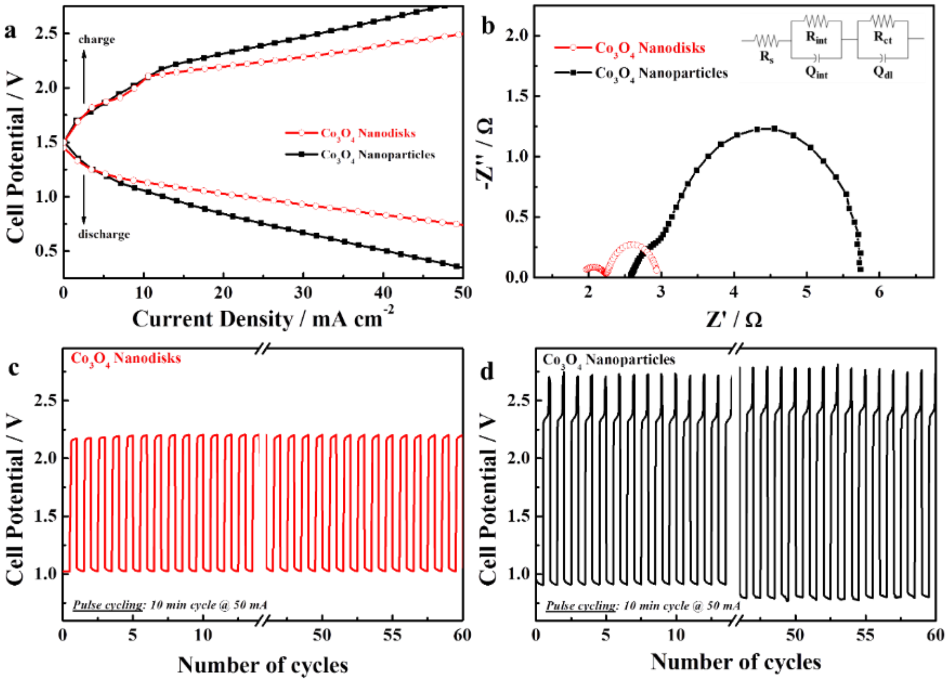

Figure 4.2 (a) Galvanodynamic charge/discharge profiles, (b) Nyquist plots (inset: equivalent circuit), and (c, d) galvanostatic pulse cyclings of Co_3O_4 nanodisks (red), and Co_3O_4 nanoparticles (black). Reproduced in adapted form from ref. 59 with permission from Elsevier.

circuit with internal (R_s), solid-electrolyte interface (R_{int}), and charge transfer (R_{ct}) resistances **(Figure 4.2b, inset)** [62] results in lower values for Co_3O_4 nanodisks compared those of the nanoparticles **(Table 4.1)**. In particular, significantly lower R_{ct} is indicative of superior electrical properties during the electrocatalytic reaction over the two-dimensional porous surface. Furthermore, the rechargeability of Co_3O_4 nanodisks is evaluated by pulse cycling where virtually no voltage fading has been observed even after 60 cycles **(Figure 4.2c)**, whereas the nanoparticle has exhibited voltage losses for both charge and discharge by 3.9 and 11 %, respectively **(Figure 4.2d)**. The excellent rechargeability of Co_3O_4 nanodisks is attributed to the reduced overpotentials particularly for the charge voltage, which significantly lessens the electrochemical degradation of the air cathode [63,64]. The high charge voltages observed with the nanoparticles, however, most likely have led to the carbon corrosion of GDL and oxidation of the catalyst [63,64]. These result in the loss of catalytically active surface area and deactivation of the catalyst, which negatively affect the battery voltages significantly over the course of cycling.

Table 4.1: Equivalent circuit element values of Co_3O_4 nanodisk and nanoparticle electrodes in a single-cell zinc-air battery. Reproduced in adapted form from ref. 59 with permission from Elsevier.

Elements	**R_s**	**R_{int}**	**R_{ct}**	**Q_{int}**	**Q_{dl}**
Nanodisks	1.88	0.384	0.698	0.00514	0.197
Nanoparticles	3.66	0.861	2.97	0.00312	0.00165

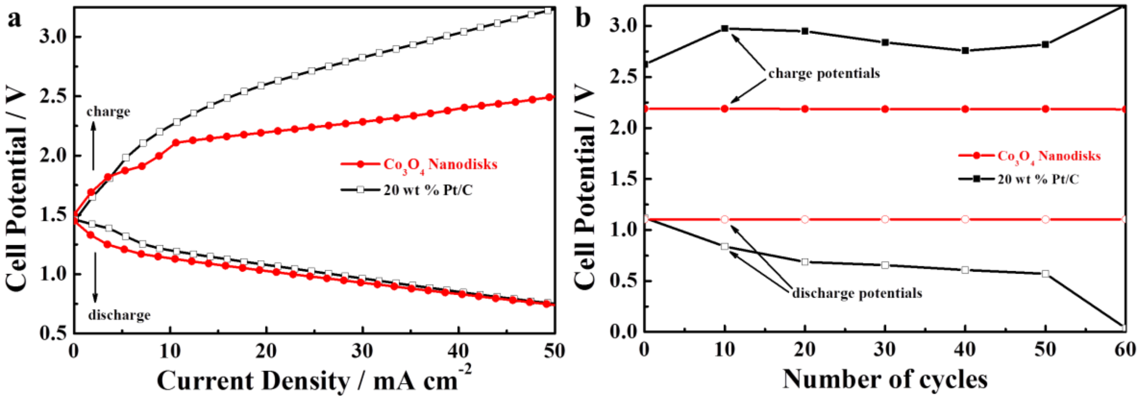

Figure 4.3 (a) Galvanodynamic charge/discharge profiles, and (b) battery voltages obtained by galvanostatic pulse cycling of Co_3O_4 nanodisks (red) and commercial Pt/C (black). Reproduced in adapted form from ref. 59 with permission from Elsevier.

The commercial viability of Co_3O_4 nanodisks as highly efficient electrocatalyst is apparent from comparable galvanodynamic discharge and much improved charge voltages compared to those of state-of-art 20 wt % Pt/C **(Figure 4.3a)**. Furthermore, Co_3O_4 nanodisks demonstrate excellent rechargeability with negligible voltage fading, whereas Pt/C shows significant drops for both discharge and charge over 60 pulse cycles, likely due to the carbon degradation of GDL, and Pt dissolution and agglomeration **(Figure 4.3b)** [64,65]. These results emphasize Co_3O_4 nanodisks as highly efficient and stable bi-functional catalyst facilitated by the reduced overpotentials, attributed to the morphological effect of enhanced mass diffusion and charge transfer of the nanodisks.

4.4 Summary

Highly active and durable Co_3O_4 nanodisk catalyst with bi-functionality towards both oxygen reduction and evolution reactions have been successfully synthesized for rechargeable zinc-air batteries utilizing ambient air. The galvanodynamic testing of Co_3O_4 nanodisks reveals superior charge and discharge voltages with excellent rechargeability demonstrated by 60 pulse cycles with no voltage fading. These advantages of Co_3O_4 nanodisks are attributed to the two-dimensional porous nanodisk morphology that facilitates mass diffusion and charge transport during electrocatalysis. This reduces the electrical resistances associated with the battery operation as confirmed by electrochemical impedance spectroscopy. Furthermore, the discharge performance of Co_3O_4 nanodisks is comparable to that of state-of-art Pt/C catalyst with much improved rechargeability demonstrated by pulse cycling, results of which highlight the practicality of Co_3O_4 nanodisks as efficient and stale bi-functional catalyst for rechargeable zinc-air battery applications.

5. One-pot Synthesis of Mesoporous $NiCo_2O_4$ Nanoplatelet and Graphene Hybrids

This chapter is reprinted in adapted form from the below article[66] with permission from the Royal Society of Chemistry.

D. U. Lee, B. J. Kim, Z. Chen, "One-pot synthesis of a mesoporous $NiCo_2O_4$ nanoplatelet and graphene hybrid and its oxygen reduction and evolution activities as an efficient bi-functional electrocatalyst", *Journal of Materials Chemistry A*, 1 (2013) 4754-4762.

5.1 Introduction

As demonstrated in the previous chapter, Co_3O_4 spinel oxide has been known to be highly efficient towards bi-functionally catalyzing the electrochemical ORR and OER in aqueous alkaline electrolytes.[23,67-69] However, one of the main challenges that all oxide based catalysts face is their relatively low electrical conductivity, which hampers charge transport during the electrochemical reactions. To improve the electrochemical activity of Co_3O_4 electrocatalysts, researchers have incorporated Ni atoms into the spinel structure to form $NiCo_2O_4$, which enhances electrical conductivity of the metal oxide and increases the number of catalytically active sites.[70,71] In addition, nanostructured $NiCo_2O_4$, specifically nanowires, have been studied extensively to investigate the morphological effect on its electrochemical activity.[70-74] However, to the best of our knowledge, there has not been any report on two-dimensional mesoporous $NiCo_2O_4$ nanoplatelets for the investigation as an electrocatalyst. Furthermore, there is no report on the combination of spinel $NiCo_2O_4$ nanostructures with carbon-based materials to improve the electrochemical properties of the metal oxide electrocatalyst. Graphene, with its intriguing properties such as large surface area, high electrical conductivity, and thermal and chemical stability,[75-78] have been reported as an excellent support material as well as an active and stable electrocatalyst itself.[79-81] For instance, extensive studies on graphene sheets have been reported as a support material for precious metal catalysts such as Pt, which demonstrated excellent electrochemical activity and stability.[10,82] Also, graphene sheets as a metal-free catalyst have been shown to demonstrate excellent performance in a hybrid electrolyte lithium-air battery.[83] We speculate that by combining a transition metal oxide catalyst with a carbon-based support via a one-pot synthesis method as opposed to simple physical mixing will lead to a strong hybridization with synergistic catalytic contributions from both of their unique properties.

Having said above, this chapter focuses on the synthesis of a novel hybrid material composed of mesoporous $NiCo_2O_4$ nanoplatelets and graphene ($NiCo_2O_4$/G) as an active bi-functional electrocatalyst for ORR and OER. This hybrid material is synthesized via a one-pot method where the precursors of the metal-oxide (Ni and Co) and graphene sheets are mixed into a single reaction to produce the final material. The one-pot synthesis utilizes facile methods based on precipitation reaction and hydrothermal process, which are very simple, cost effective, and highly efficient for producing large quantities of material. The evaluation of electrochemical activities of the hybrid towards ORR and OER is conducted by employing half-cell testing. We investigate the hybrid effect of combining $NiCo_2O_4$ nanoplatelets with graphene sheets by comparing its performance to that of $NiCo_2O_4$ itself without graphene sheets. The importance of PVP on the electrocatalytic activity is investigated by comparing the performance $NiCo_2O_4$/G to that of a hybrid created without the addition of PVP during synthesis—a capping agent that is responsible for controlling the morphology of $NiCo_2O_4$ nanostructures. We also demonstrate the advantages of incorporating Ni atoms into the spinel crystal structure by comparing the electrocatalytic activities to un-doped Co_3O_4/G.

5.2 Experimental Methods

5.2.1 Graphene oxide (GO) synthesis

GO is synthesized from natural graphite flakes by the modified Hummers' method.[84] In a typical GO preparation, 2 g of graphite powder (Alfa Aesar) is stirred in 46 mL of concentrated sulphuric acid (Fisher Scientific) for 10 hours. The mixture is put into an ice bath and 1 g of sodium nitrate (Aldrich) is added followed by the addition of 6 g of potassium permanganate (EMD) under stirring. The mixture is removed from the ice bath and stirred for 1 hour. Then 92 mL of distilled de-ionized (DDI) water is added drop-wise and stirred for another 30 minutes followed by the addition of 280 mL of warm DDI water (40 ^{o}C) and 40 mL of 30 % H_2O_2 (Fisher Scientific). The mixture is filtered and washed with 3 L of 5 % HCl solution, then centrifuged five times at 4000 rpm for 10 min. The product is collected and dried in room temperature.

5.2.2 One-pot synthesis of mesoporous $NiCo_2O_4$ nanoplatelet and graphene hybrid

The one-pot synthesis of mesoporous $NiCo_2O_4$/G hybrid is carried out by concurrent precipitation and hydrothermal reactions. In a typical synthesis, 1.65 g of polyvinylpyrrolidone (PVP) with a molecular weight of 24,000 is dissolved in a 10 mL mixture of double deionized (DDI) water and ethanol with a 1:1 volume ratio. Then, 0.419 g and 0.833 g of $Ni(NO_3)_2 \cdot 6H_2O$ and $Co(NO_3)_2 \cdot 6H_2O$, respectively, were dissolved in the PVP solution, and magnetically stirred for 30 minutes with the mixture bubbled with N_2. Next, 0.213 mL of a 1.0 M NaOH aqueous solution was added dropwise at a rate of 0.56 mL/min to induce a precipitation reaction, followed by the addition of 100 mg of GO. Then, 6 mL of NH_4OH is added and stirred vigorously for 30 minutes. The suspension was then transferred to into a Teflon-lined autoclave, sealed and then heated at 120 ^{o}C for 6 hours. The autoclave is naturally cooled to room temperature, then the precipitate is collected and centrifuged three times with DDI and another 3 times with acetone at 5000 rpm to remove any impurities and excess PVP. The obtained black slurry is freeze dried for 24 hours, turning into a fine powder, which is calcined in air at 300 ^{o}C for 3 hours to obtain the final product.

5.2.3 Three-electrode half-cell test

The electrochemical activities of the materials developed in the present work were tested in an aqueous electrolyte (0.1 M KOH) using a standard three-electrode electrochemical cell via rotating disk electrode (RDE) voltammetry for ORR and cyclic voltammetry (CV) for OER. The setup for RDE and CV consists of a potentiostat (Pine Instrument Co., AFCBP-1) and a rotation speed controller (Pine Instrument Co., AFMSRCE). All electrochemical testing was performed at room temperature using a Saturated Calomel Electrode (SCE) as a reference electrode. A platinum wire was used as the counter electrode. A glassy carbon electrode (5 mm OD) coated with 20 uL of 4 mg mL^{-1} suspension made by mixing $NiCo_2O_4$/G and a solution of 0.5 wt% Nafion in ethanol was used as the working electrode. The same preparation of the working electrode was used for all other comparison materials. ORR curves were recorded from -1.0 to 0.2 V at a scan rate of 10 mV s^{-1} with O_2-saturated electrolyte under various electrode rotation speeds (100, 400, 900, 1600 rpm). The ORR polarization curves were background corrected by subtracting the currents obtained under the same testing conditions in N_2-saturated electrolyte. The OER curves were record from 0 to 1.0 V at a scan rate of 50 mV s^{-1} with N_2-saturated electrolyte with a rotation speed of 900 rpm in order to spin off the oxygen evolved during voltammetry testing.

5.3 Results and Discussion

The structure and surface morphology of mesoporous $NiCo_2O_4$/G hybrid formed by a one-pot synthesis method are characterized using SEM. During synthesis, PVP plays two important roles in controlling the final morphology of the hybrid. First, PVP is well-known to coordinate to the surface of metal ions such as cobalt ions through -N and/or C=O groups of the pyrrolidone ring.[85] Hence, PVP acts as a capping agent in a mix of H_2O and ethanol solution by selectively adsorbing onto specific crystallographic planes to provide spatial confinements for anisotropic growth of $NiCo_2O_4$ into 2-dimensional nanoplatelets[60,86] **(Figure 5.1a)**. Second, the surface adsorbed PVP decomposes upon calcination process in air at 300 ^{o}C for 3 h to leave behind meso-sized pores in the nanoplatelets **(Figure 5.1b)**. A detailed inspection of the nanoplatelets using TEM clearly shows well-distributed mesopores in the nanoplatelets with a variety of size and shape **(Figure 5.1c)**. This unique porous structure is likely to create more active sites with increase surface area and facilitate in the transport of reactant species during electrocatalysis. $NiCo_2O_4$ nanoplatelets exhibit highly crystalline structure as confirmed by distinct diffraction dots observed in the FFT pattern **(Figure 5.1c, inset)**. Further analyzing the FFT pattern have revealed characteristic crystallographic orientations of (111), (220), and (311) for the spinel $NiCo_2O_4$. In addition, calculation of the d-spacing using the fringes observed in the HR-TEM image of the nanoplatelets has resulted in 0.46 nm **(Figure 5.1d)**, which very closely match with the theoretical d-spacing for the (111) orientation of a cubic spinel $NiCo_2O_4$ (0.46 nm) [JCPDS: 20-0781]. The high crystallinity of the nanoplatelets has also been confirmed by SAED, which shows a clear diffraction pattern for various crystallographic planes of the spinel **(Figure 5.1d, inset)**.

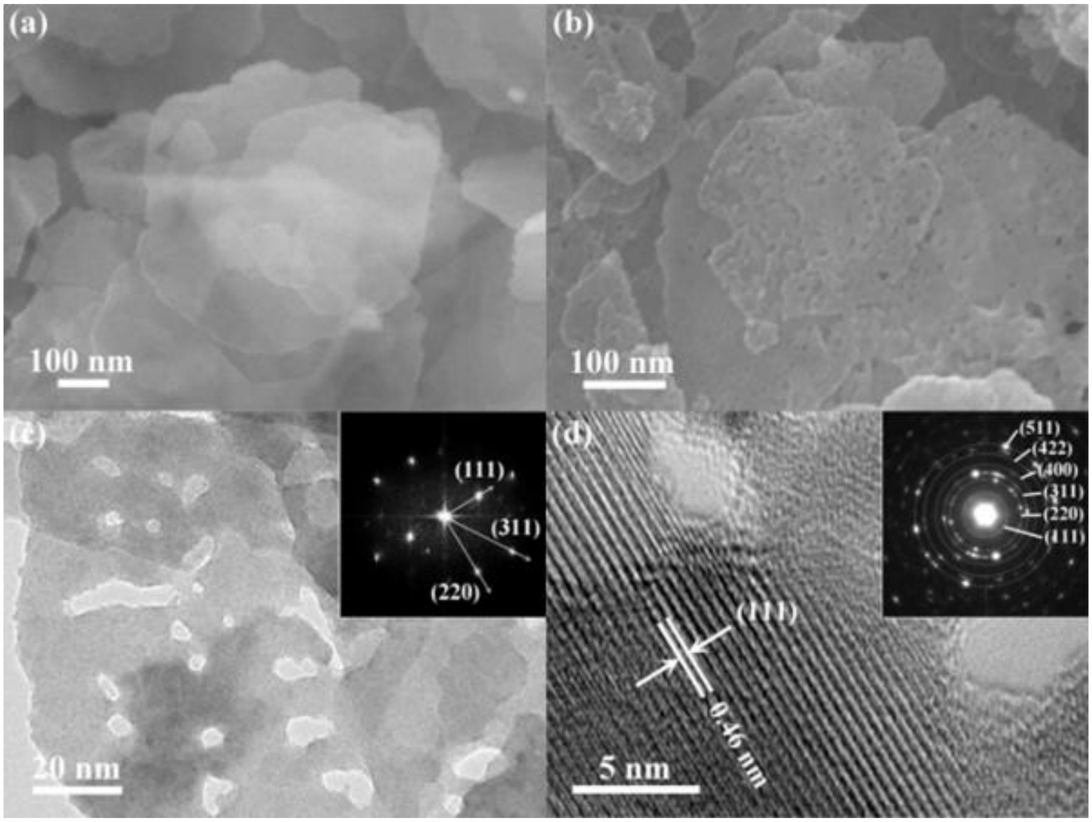

Figure 5.1 (a) SEM image of uncalcined $NiCo_2O_4$/G prior to the formation of mesopores on the nanoplatelets. (b) SEM image of calcined $NiCo_2O_4$/G with mesoporous on the nanoplatelets. (c) TEM image of $NiCo_2O_4$/G uniformly distributed mesoporous. Inset, FFT pattern of cubic spinel $NiCo_2O_4$ nanoplatelets in the hybrid. (d) HRTEM image of (111) crystal plane of spinel $NiCo_2O_4$ nanoplatelets. Inset, SAED pattern of spinel $NiCo_2O_4$ nanoplatelets in the hybrid. Reproduced in adapted form from ref. 66 with permission from the Royal Society of Chemistry.

The BET characterization has been carried out to confirm the mesoporous nature of $NiCo_2O_4$/G. The nitrogen adsorption-desorption curves demonstrates a Type IV isotherm, and a distinct hysteresis loop in the P/P^o range of 0.6 to 1.0 **(Figure 5.2a)**, which are strong indications of capillary condensation and multilayer adsorption, hence the presence of mesopores. The BET specific surface area is found to be 77 m^2 g^{-1}, higher than that of previously reported graphene-

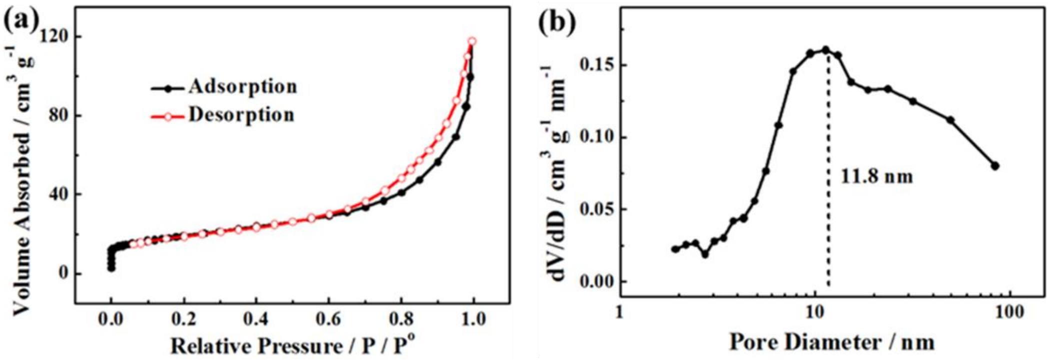

Figure 5.2 (a) Nitrogen adsorption-desorption isotherm loop and pore size distribution curve calculated by BJH model of $NiCo_2O_4$/G. Reproduced in adapted form from ref. 66 with permission from the Royal Society of Chemistry.

nickel cobaltite nanocomposite.[87] The higher specific surface area enhances the exposure of active sites available for reaction on the surface. The outstanding electrocatalytic activity of $NiCo_2O_4$/G is most likely ascribed to this increased number of active sites as both the ORR and OER are surface reactions. The pore size distribution calculated by the BJH model shows a predominant peak in the meso-scale of 5 to 15 nm with an average pore diameter of 11.8 nm **(Figure 5.2b)**, consistent with pore sizes observed by HRTEM analysis **(Figure 5.1c)**. The broad pore distribution in the range of 15 to 100 nm is probably due to the interlayer spacings formed between nanoplatelets and graphene sheets. Hence, it can be concluded from the isotherm and the pore size distribution that $NiCo_2O_4$/G consists of mesopores which enhances the electrocatalytic activity by increasing surface exposure of the active sites.

The crystal structure of $NiCo_2O_4$/G is further investigated by XRD **(Figure 5.3)**, and the characteristic peaks are well indexed to those of spinel $NiCo_2O_4$ [JCPDS: 20-0781]. The XRD pattern of $NiCo_2O_4$/G compared to that of Co_3O_4/G, which is synthesized using the same procedure but the Co metal precursor replacing that of Ni, also demonstrates spinel crystallinity. However, the peaks are relatively broad in the case of $NiCo_2O_4$/G, which is indicative of smaller crystallites

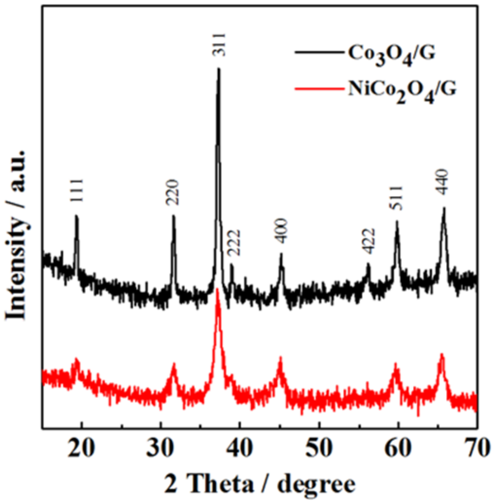

Figure 5.3 XRD patterns of spinel crystal structure in $NiCo_2O_4$/G and Co_3O_4/G hybrids. Reproduced in adapted form from ref. 66 with permission from the Royal Society of Chemistry.

formed due to the change in the structure with the addition of Ni atoms into the spinels of Co_3O_4. The d-spacing of each crystal orientation observed in the XRD pattern is calculated based on the diffraction angle using Bragg's law, and they match closely with those calculated with the SAED pattern from the TEM characterization **(Table 5.1)**, signifying a successful synthesis of $NiCo_2O_4$ spinels. Additionally, using the d-spacing of the (400) plane, the lattice parameter (a_0) of the cubic spinel structure is determined to be 0.803 nm. This is slightly larger than 0.801 nm of Co_3O_4/G, which is consistent with the literature where the incorporation of Ni into the Co_3O_4 spinel is known to expand the elementary spinel lattice.[88,89]

The surface elemental compositions and electronic configurations of the atoms in the hybrid are investigated by employing XPS. As expected, the full survey of $NiCo_2O_4$/G revealed peaks corresponding to the existence of Ni 2p, Co 2p, O 1s, and C 1s **(Figure 5.4a)**. The de-convolution of the Ni 2p peaks shows the atoms in $2P_{1/2}$ and $2P_{2/3}$ electronic configurations at

Table 5.1 Calculated values of d-spacing for each crystal orientation observed in SAED pattern obtained from TEM and diffraction angles obtained from XRD of $NiCo_2O_4$/G. Reproduced in adapted form from ref. 66 with permission from the Royal Society of Chemistry.

	TEM		XRD	
Crystal Orientation	**diffraction radius (nm^{-1})**	**d-spacing (nm)**	**2 theta (degree)**	**d-spacing (nm)**
440	7.00	0.143	65.50	0.142
511	6.91	0.146	59.60	0.155
422	6.02	0.166	56.22	0.163
400	4.90	0.204	45.10	0.201
311	4.06	0.246	37.21	0.241
220	3.53	0.283	31.70	0.282
111	2.18	0.459	19.34	0.458

872.78 eV and 855.38 eV, respectively **(Figure 5.4b)**. Similarly, the de-convoluted Co 2p shows the electronic configuration of Co atoms in $2P_{1/2}$ and $2P_{2/3}$ states at 795.28 eV and 779.98 eV, respectively **(Figure 5.4c)**. The binding energies of these peaks are consistent with the literature and signify the formation of cubic spinel $NiCo_2O_4$. The O 1s shows a large M-O-M peak at 529.48 eV which is indicative of most of the oxygen in the lattice, with the other two peaks C=O and O-C=O bonds, at 532.83 and 531.15 eV, respectively, that correspond to oxygen groups of the graphene sheets most likely due to an incomplete reduction and also due to the moisture adsorbed onto the graphene sheets in the ambient condition **(Figure 5.4d)**. The comparison of XPS spectra of $NiCo_2O_4$ and $NiCo_2O_4$/G for the elements Ni, Co, and C have revealed no shift in the binding energy of the peaks after the hybridization of the metal oxide and graphene sheets. However, a positive shift in the binding energy for the O 1s peak is observed for $NiCo_2O_4$/G compared to that

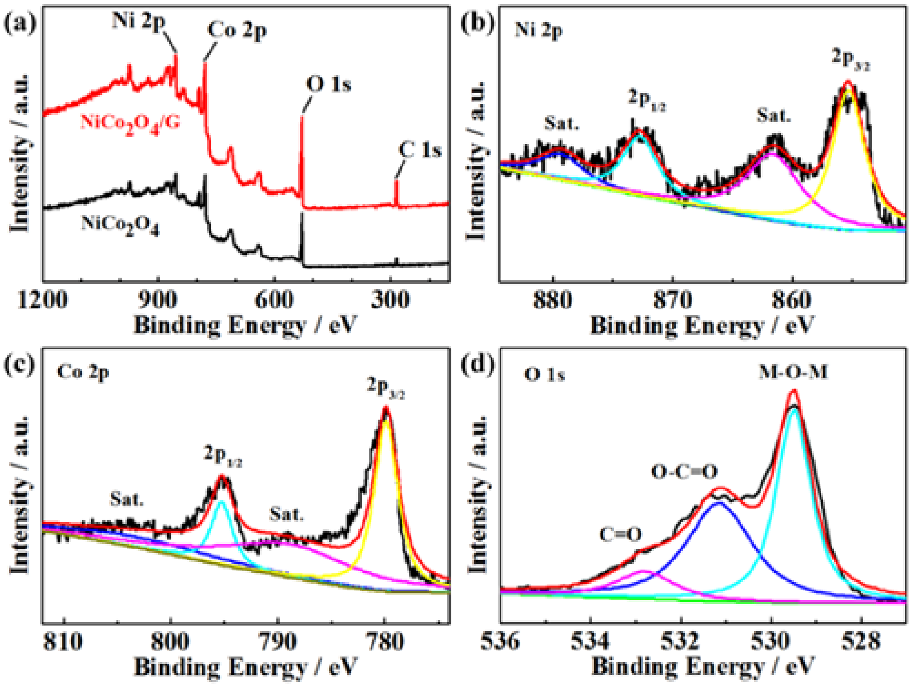

Figure 5.4 (a) Full XPS spectra of NiCo$_2$O$_4$/G hybrid and graphene-free NiCo$_2$O$_4$. (b) High-resolution Ni 2p XPS spectra of NiCo$_2$O$_4$/G. (c) High-resolution Co 2p XPS spectra of NiCo$_2$O$_4$/G. (Note for (b) and (c): The black line is the original signal, and the red curve is the result of the curve fit. Yellow and cyan peaks correspond to 2p$_{3/2}$ and 2p$_{1/2}$ species, respectively, and pink and blue peaks corresponds to the associated satellite species, after de-convolution.) (d) High-resolution O 1s XPS spectra of NiCo$_2$O$_4$/G. (The black line is the original signal, and the red curve is the result of the curve fit. Cyan, blue, and pink peaks correspond to lattice oxygen, Yellow and cyan peaks correspond to 2p$_{3/2}$ and 2p$_{1/2}$ species, respectively, and pink and navy peaks corresponds to the associated satellite species, after de-convolution.) Reproduced in adapted form from ref. 66 with permission from the Royal Society of Chemistry.

of NiCo$_2$O$_4$. This is an indication that the hybridization is probably occurring through the oxygen species of GO, which most likely have reacted with the metal precursors at the time of the one-pot synthesis.

The electrochemical characterization of $NiCo_2O_4$/G is conducted by performing three electrode half-cell testing in 0.1 M KOH. The catalysis of ORR using $NiCo_2O_4$/G hybrid as the electrocatalyst is studied by RDE voltammetry. As expected, the polarization curves of the hybrid obtained at various rotation speeds show a well-defined drop in the current density for oxygen reduction in the mixed kinetic- and diffusion-limiting region followed by a plateau at a stable current density in the diffusion-limited region **(Figure 5.5a)**. Using these polarization curves, several potential points are selected between 0.65 and 0.90 V (vs. SCE) to determine the Koutecky-Levich slope, which is used to calculate the number of electrons transferred, *n*, during the ORR **(Figure 5.5a, inset)**. The analysis of the plot have resulted in $n = 3.9$ confirming that the ORR catalyzed by the hybrid occurs in a highly desirable pseudo four-electron reduction pathway ($O_2 + 2H_2O + 4e^- \rightarrow 4OH^-$). This excellent electrochemical activity of the hybrid towards ORR is attributed to the incorporation of Ni atoms into the spinel structure as observed by much enhanced ORR polarization curve of $NiCo_2O_4$/G at the rotation rate of 900 rpm compared to that of Co_3O_4/G with the same structure and surface morphology **(Figure 5.5b)**. In terms of the onset potential, the hybrid exhibits a much higher value of -0.12 V compared to -3.00 V of Co_3O_4/G. Furthermore, the half-wave potential (HWP) of the hybrid demonstrated a much higher value of -0.27 V compared to -0.41 V of Co_3O_4/G. These enhancements observed in the onset potential and HWP are strong indications of highly efficient active sites of $NiCo_2O_4$/G towards ORR. In addition, a significant increase in the stable current density obtained at the diffusion-limited region is indicative of increased accessibility of O_2 onto the active sites for enhanced ORR activity, which could be attributed to the smaller crystallite size of $NiCo_2O_4$/G hybrid observed from the broad peaks of XRD pattern.

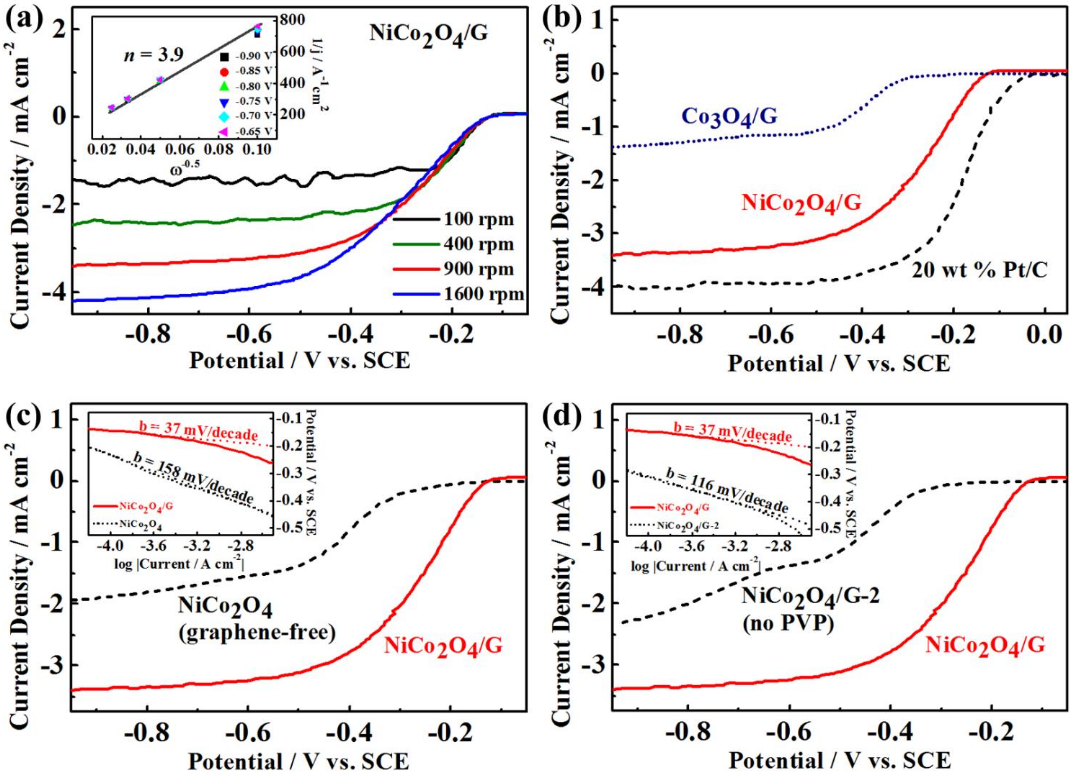

Figure 5.5 (a) ORR polarization curves of $NiCo_2O_4$/G obtained by RDE voltammetry in O_2-saturated 0.1 M KOH at various rotation rates. Inset, Koutecký-Levich plot of $NiCo_2O_4$/G at potentials -0.65, -0.70, -0.75, -0.80, -0.85, -0.90 V (vs. SCE). (b) ORR polarization curves of $NiCo_2O_4$/G, Co_3O_4/G, and 20 wt % Pt/C at a rotation rate of 900 rpm. ORR polarization curves and Tafel plots (inset) of (c) $NiCo_2O_4$ and $NiCo_2O_4$/G, and (d) $NiCo_2O_4$/G-2 and $NiCo_2O_4$/G at a rotation rate of 900 rpm. Reproduced in adapted form from ref. 66 with permission from the Royal Society of Chemistry.

The excellent ORR activity of the hybrid is ascribed to the formation of highly efficient active sites created by Ni cations in the spinel lattice. Also, previous literatures have shown that the insertion of Ni into the octahedral sites of the spinel increases the electrical conductivity, which is highly desirable for fast charge transfer during ORR.[71] Even though some spinel metal oxides are known to exhibit high electrocatalytic activities,[40] metal oxides have relatively lower electrical conductivity than carbon-based materials such as graphene sheets. This may prevent efficient utilization of active sites of the metal oxide that available for electrocatalytic activity. Hence, by combining $NiCo_2O_4$ with graphene sheets into a hybrid, a much enhanced ORR polarization curve is observed compared to that of graphene-free $NiCo_2O_4$ itself **(Figure 5.5c)**. Graphene-free $NiCo_2O_4$ is synthesized the same way as the hybrid but without the addition of GO during the one-pot synthesis. The polarization curve of the hybrid clearly shows a significantly higher (more negative) limiting current density, which is an indication of increased number of active sites for ORR. In the hybrid, graphene sheets most likely facilitate the distribution of the metal oxide nanoplatelets to prevent agglomeration of particles, thereby increasing the number of active sites. Furthermore, the enhancement in the onset potential of the hybrid may be an indication that the graphene sheets themselves are catalytically active, which have been reported in the literature as an ORR-active catalyst,[83,90] since the ORR kinetics of $NiCo_2O_4$ should be the same in the case of both the hybrid and the metal oxide itself. The analysis of the Tafel plot have resulted in a much lower slope for the hybrid in the lower overpotential region compared to the metal oxide itself. This is indicative of enhanced ORR kinetics with the addition of graphene sheet, which is consistent with the previous observation **(Figure 5.5c, inset)**. The PVP effect of the nanoplatelets is investigated by comparing ORR polarization curve of $NiCo_2O_4$/G hybrid with that of a hybrid synthesized by the same procedure as $NiCo_2O_4$/G but without the addition of PVP ($NiCo_2O_4$/G-2) **(Figure 5.5d)**. The observation of the ORR polarization curve of $NiCo_2O_4$/G-2 suggests that the oxygen reduction proceeds in a two-electron reduction pathways, which is highly undesirable due to an inefficient catalytic activity and the formation of peroxide species which may promote electrocatalyst degradation. $NiCo_2O_4$/G hybrid exhibits increased (more negative) limiting current density in the diffusion-limited region most likely due to higher surface area from the mesopores in the nanoplatelets, which would be absent in the case of $NiCo_2O_4$/G-2. In addition, improved onset potential and HWP are observed for $NiCo_2O_4$/G with a significantly lower Tafel slope compared to that of $NiCo_2O_4$/G-2 (116 mV/decade) **(Figure 5.5d, inset)**. These enhanced ORR characteristics are ascribed to more efficient active sites created with the addition of PVP during the synthesis of $NiCo_2O_4$/G.

The oxygen evolution activity of $NiCo_2O_4$/G hybrid is investigated by analyzing CV curves obtained by half-cell testing. The CV curve of $NiCo_2O_4$/G shows the anodic peak at 0.49 V (and its corresponding cathodic peak at 0.28 V), which corresponds to the transition of the redox couple Ni(III)/Ni(IV). This redox couple is known to be the cation in the octahedral site of the spinel that responsible for the catalysis of OER.[70,71] This anodic peak is followed by the onset of oxygen evolution and the dramatic increase in the current density due to the excellent OER activity of the hybrid. Peaks that correspond to the redox couple Ni(II)/Ni(III) and Co(ll)/Co(lll) are not visible in the CV curve because these cations located in the tetrahedral sites of the spinel are much more difficult to oxidize or reduce than those in the octahedral sites.[89,91] In order to elucidate the effect of graphene in the hybrid, the OER activity of the hybrid is compared to that of $NiCo_2O_4$ itself **(Figure 5.6a)**. The onset potential of the oxygen of graphene-free $NiCo_2O_4$ (0.62 V), indicative of much lower activation energy for OER with the addition of graphene sheets. Furthermore, the hybrid exhibits a much higher current density at 0.95 V of 35.4 mA cm^{-2} compared to only 18.6 mA cm^{-2} for the graphene-free $NiCo_2O_4$. This excellent OER activity of the hybrid is attributed to the high electrical conductivity provided by graphene sheets which facilitate charge transfer during the reaction at the surface of the metal oxide. The investigation of OER kinetics via the Tafel analysis in the low overpotential region have confirmed a much faster OER activity indicated by a much lower slope of 161 mV/decade of the hybrid compared to 205 mV/decade of the metal-

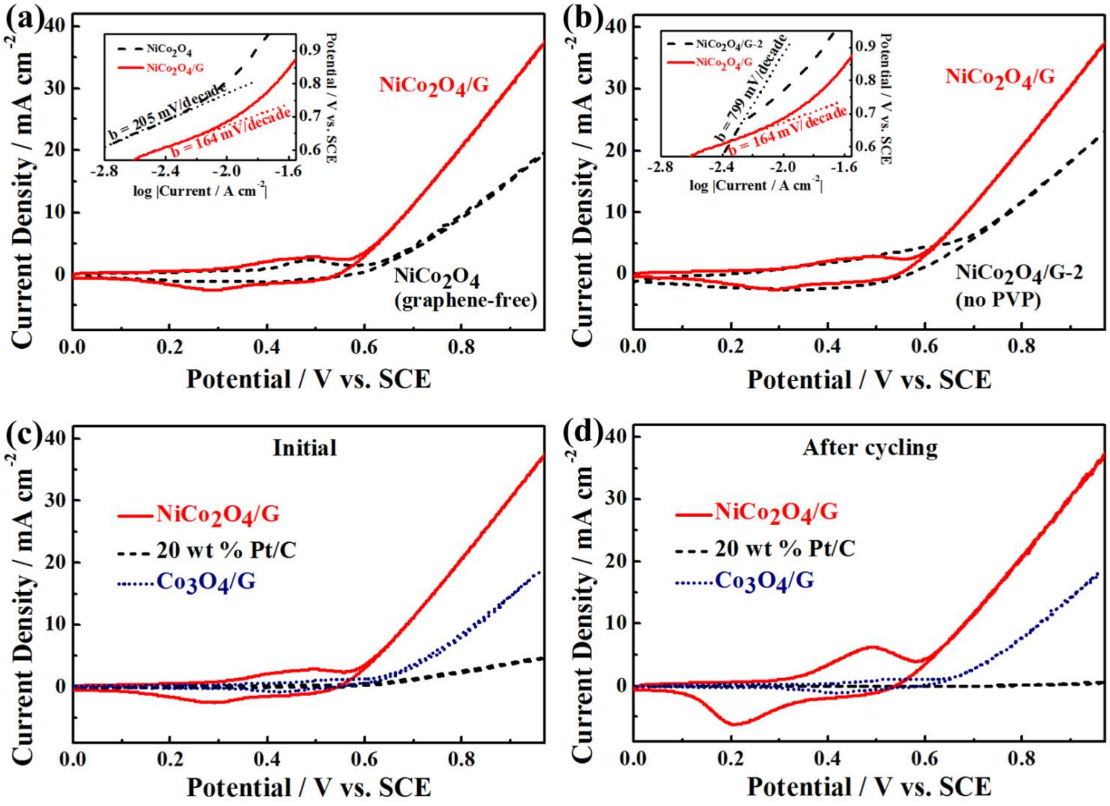

Figure 5.6 OER CV curves and Tafel plots (inset) of (a) $NiCo_2O_4$ and $NiCo_2O_4$/G, and (b) $NiCo_2O_4$/G-2 and $NiCo_2O_4$/G obtained by N_2-saturated 0.1 M KOH act a rotation rate of 900 rpm. OER CV curves of $NiCo_2O_4$/G, Co_3O_4/G and 20 wt % Pt/C (c) initial cycle and (d) after 1000 CV cycles. Reproduced in adapted form from ref. 66 with permission from the Royal Society of Chemistry.

oxide itself **(Figure 5.6a, inset)**. In addition, the effect of adding PVP during the synthesis is highly beneficial for the OER activity of $NiCo_2O_4$/G as a significantly higher OER current density of 35.4 mA cm^{-2} is observed at 0.95 V compared to only 21.4 mA cm^{-2} of $NiCo_2O_4$/G-2 **(Figure 5.6b)**. The analysis of Tafel plot of $NiCo_2O_4$/G-2 has resulted in an unusually high Tafel slope of 799 mV/decade, which is indicative of very slow OER kinetics **(Figure 5.6b, inset)**. The enhanced OER performance of $NiCo_2O_4$/G is again ascribed to more efficient active sites with much lower energy barrier created with the addition of PVP during the synthesis $NiCo_2O_4$/G. Furthermore, to study the effect of the addition of Ni species into the spinel crystal structure, the OER activity of $NiCo_2O_4$/G is compared to that of Co_3O_4/G **(Figure 5.6c)**. Without the addition of Ni, Co_3O_4/G is observed to exhibit much lower current density of 18.35 mV cm^{-2} at 0.95 V compared to that of 36.4 mV cm^{-2} for $NiCo_2O_4$/G. Similar to ORR performance, this enhancement in OER activity is due to the Ni species in the octahedral sites of the spinel that create active sites for OER with much lower activation potential compared to that of Co cation. The electrochemical durability of the hybrid is evaluated by repeating the CV cycle 1000 times **(Figure 5.6d)**. After cycling, the current density retention at 0.95 V is 99.6 % for the hybrid. The cobalt oxide hybrid have also exhibited a very stable OER durability with 98.6 % current density retention, however, the commercial Pt/C have degraded much heavily, resulting in a very low current density retention of 8.0 %. This excellent durability demonstrated by $NiCo_2O_4$/G attributed to the graphene sheets in the hybrid acting as a support for the electrocatalyst to provide fast charge transfer and prevent agglomeration of the nanoplatelets.

5.4 Summary

In summary, we have synthesized mesoporous $NiCo_2O_4$ nanoplatelet/graphene hybrid as a highly active bi-functional catalyst for oxygen reduction and oxygen evolution reactions by a one-pot precipitation reaction and hydrothermal process. The hybrid effect of $NiCo_2O_4$/G on ORR and OER activities confirmed by RDE and CV measurements, respectively, are attributed to much faster charge transfer facilitated by graphene sheets as a support material. Also, the addition of PVP during synthesis is highly beneficial for enhanced ORR and OER activities most likely due to the formation of highly efficient active sites of the nanoplatelets. Finally, the incorporation of

Ni atoms into the spinel lattice is found to significantly improve both ORR and OER performances of Co_3O_4/G. This is ascribed to the increased electrical conductivity and the creation of new active sites by Ni incorporation into the octahedral sites of the spinel crystal structure.

6. Self-Assembled Mesoporous Spheres as Bi-functionally Active Electrocatalysts

This chapter is reprinted in adapted form from the below article[92] with permission from Wiley.

D. U. Lee, J. Li, M. G. Park, M. H. Seo, W. A, I. Stadelmann, L. Ricardez-Sandoval, Z. Chen, "Self-Assembly of Spinel Nanocrystals into Mesoporous Spheres as Bifunctionally Active Oxygen Reduction and Evolution Electrocatalysts", ChemSusChem, 10 (2017) 2258-2266.

6.1 Introduction

Soaring energy demands during the past few decades have led to continued burning of fossil fuels, producing greenhouse gases that contribute to increasing global warming. To address the energy demands and reduce carbon emissions, advance energy storage conversion and storage systems that produce energy in a clean and sustained route have recently been investigated by many researchers. Rechargeable metal-air batteries are considered one of the most promising future generation energy systems due to their extremely high energy density and flat discharge potentials.[5,93,94] These advantages of rechargeable metal-air batteries make them particularly interesting for applications in electric drive vehicles for improving insufficient driving range, as well as in electrical energy storage (EES) systems for coupling intermittent renewable wind and solar energy sources into smart energy-grids.

Rechargeable metal-air batteries, however, require active bi-functional electrocatalysts to accelerate the kinetics of intrinsically sluggish oxygen reduction reaction (ORR) and oxygen evolution reaction (OER), which are the fundamental electrochemical reactions that govern the discharge and charge processes, respectively.[95] For the development of practically viable rechargeable metal-air batteries, bi-functional electrocatalysts residing in the air electrode must be sufficiently catalytically active towards both ORR and OER.[96-98] Currently, the state-of-the-art catalyst, platinum on carbon (Pt/C) demonstrates the ORR highest activity. However, it is very costly due to its scarcity, and is only mono-functionally active towards ORR, making it unsuitable for the production of cost-competitive rechargeable metal-air batteries.[66,99] For instance, primary (non-rechargeable) zinc-air batteries are the only type of metal-air battery that is currently available in the market for niche applications such as hearing-aids, and it utilizes inexpensive earth-abundant Mn-based catalysts. Despite its affordability and excellent discharge characteristics, primary zinc-air batteries cannot be recharged efficiently due to insufficient OER activity (charge performance) of the catalyst.

Recently, numerous non-precious bi-functional catalyst developments have been reported in the literature including transition metal oxides[51,100], nanostructured carbons[101-103], and hybrid catalysts[21,104,105]. For example, a novel metal-free transition metal oxide such as mesoporous Co_3O_4 synthesized by silica templating method has been shown to be highly active and durable as a bi-functional catalyst, demonstrating a comparable total overpotential of 1.034 V and superior methanol-tolerance than noble-metal counterparts.[51] Nanostructured carbon based catalysts have also been developed, Tian et al. reporting coaxial nanocables with surface nitrogen groups that are capable of catalyzing both ORR and OER with significantly reduced overpotentials for both oxygen reactions.[101] Recently, hybrid catalysts composed of non-precious metal oxide and nanocarbons have received a tremendous attention due to their improved catalytic activity through synergistic enhancements between the two components. Notably, Co_3O_4 nanocrystals decorated nitrogen-doped carbon nanotubes have been shown to be bi-functionally very effective for rechargeable zinc-air batteries, demonstrating stable charge and discharge voltages over a total of 100 hours without any voltage degradation.[106]

Despite these efforts, much work is still needed for non-precious bi-functional catalyst developments to understand the exact reaction mechanisms and degradation pathways of mixed spinel oxides, such as $NiCo_2O_4$, $MnCo_2O_4$, $FeCo_2O_4$. Specifically, the work presented here utilizes both experimental and first-principles density functional theory (DFT) computational approaches to investigate the bi-functional electrocatalytic behaviours of spinel structured oxides of varying compositions, including Co_3O_4, $(Ni,Co)_3O_4$, and $(Mn,Co)_3O_4$. These spinel oxides fabricated by a facile solvothermal technique demonstrates self-assembled mesoporous spherical morphology with varying degrees of catalytic activities towards both ORR and OER depending on the type of transition metals (Co, Ni, and Mn) inserted into the octahedral sites of the spinel lattice. The first-principles DFT computational method has been employed to find the potentials at which all oxygen intermediate steps proceed spontaneously, to verify the experimentally obtained electrochemical results. The outcomes of this study opens the door for designing affordable non-precious bi-functional catalysts with tailored ORR and OER activities depending on the modification of the composition of spinel metal oxides for rechargeable metal-air battery applications.

6.2 Experimental

6.2.1 Synthesis of Spinel Oxide Spheres

The metal oxide spheres were prepared by a facile solvothermal technique, where a total of 3.0 mmol of cobalt nitrate hexahydrate (2:1 mass ratio of cobalt nitrate hexahydrate and either nickel nitrate hexahydrate or manganese nitrate tetrahydrate for the synthesis of $(Ni,Co)_3O_4$ or $(Mn,Co)_3O_4$) was dissolved in a mixed solution of 30 mL of ethylene glycol and 10 mL double de-ionized (DDI) water by stirring for 30 minutes. Then 30 mmol of ammonium bicarbonate was added to the mixture and dissolved by stirring for 30 minutes. The solution was then transferred to a Teflon cup inside a stainless steel autoclave reactor and heated in the oven at 200 ^{o}C for 24 hours. The resulting solid product was centrifuged five times, three times with DDI water and two times with ethanol, then dried overnight in a 60 ^{o}C oven. Finally, the dried product was calcined using a furnace in air at 350 ^{o}C for two hours.

6.2.2 Electrochemical Evaluation

The half-cell electrochemical evaluation of the metal oxides was conducted via rotating disk electrode (RDE) voltammetry using a three-electrode glass cell, potentiostat (CH Instruments 760D), and rotation speed controller (Pine Instruments Co., AFMSRCE). To prepare the working electrode, the ink solution prepared by mixing metal oxide and carbon black (Vulcan Carbon XC-72) in a 1:1 mass ratio in an ethanol-diluted AS-4 (Tokuyama Corp.) ionomer solution having a total active material concentration of 4 mg mL^{-1} was coated onto a polished glassy carbon disk electrode (5 mm OD) resulting in active material loading of 0.20 mg cm^{-2}. As the counter and reference electrodes, a platinum wire and saturated calomel electrode (SCE) were used, respectively, and as the electrolyte, 0.1 M potassium hydroxide was used. To activate the working electrode, cyclic voltammetry (CV) was conducted for 20 cycles at the scan rate of 50 mV s^{-1}, and the background current was measured at the scan rate of 10 mV s^{-1} within the potential range of 0 to -1.0 V vs SCE in the N_2-saturated electrolyte. The oxygen reduction, and oxygen evolution activities were then measured in the oxygen-, and nitrogen-saturated electrolyte, respectively, at the scan rate of 10 mV s^{-1}. To measure double layer capacitance, CV of the working electrode was obtained at various scan rates (2.5, 5, 10, 20, 40 mV s^{-1}) over a potential window of 60 mV around the open circuit potential in 0.1 M tetrabutylammonium hexafluorophosphate in acetonitrile.

6.2.3 Computational Details

Density Functional Theory (DFT) calculations were carried out using the program BAND[107], where the electron wave functions were developed on a basis set of numerical atomic orbitals (NAOs) and of Slater type orbitals (STOs). The triple polarization (TZP) basis of Slater-type orbitals was used. The calculations were performed by using Revised Perdew-Burke-Ernzerhof (RPBE) generalized gradient approximation (GGA) for the exchange and correlation energy terms.[108] This is a widely accepted function for various applications including metal oxide systems, producing reliable energetics.[109,110] The BAND program performs numerical integrations for all matrix elements.[111] The accuracy of the integration in real space (*Accuracy*) and the sampling of the Brillouin zone (KSpace) for the integration accuracy in *k-space* are two key major numerical parameters in the present DFT calculations. In the present study, the *Accuracy* parameter was set to 4, which is a reasonable value based on previous analysis[112-114], whereas the *k-space* parameter was set to 3[115,116], which indicates that the quadratic tetrahedron method[117] was chosen to perform the k-space numerical integration. The calculations performed on this study were spin-unrestricted. For modelling, the ORR/OER behaviours were predicted on the (110) surface of the spinel crystal using periodic six atomic layer slabs with a (2×2) unit cell. The (110) surface was chosen because it has been predicted to be one of the most stable plane exposed in a number of cubic spinel Co_3O_4 specimens prepared by various methods.[118-120] The bottom two atomic layers of the slab was fixed in its bulk positions, whereas the remaining atomic layers and the adsorbed species were set free to relax. On the basis of fully relaxed structures, free energy of each oxygen intermediate reaction (ΔG) during ORR/OER on Co_3O_4, $(Ni,Co)_3O_4$, and $(Mn,Co)_3O_4$ surfaces was calculated. Specifically, the following oxygen intermediate reactions were considered for alkaline electrolyte conditions expressed in terms of OH^-.

$$O_2(g) + 2H_2O(l) + 4e^- \leftrightarrow OOH^* + H_2O(l) + OH^- + 3e^- \quad (2)$$

$$OOH^* + H_2O(l) + OH^- + 3e^- \leftrightarrow O^* + H_2O(l) + 2OH^- + 2e^- \quad (3)$$

$$O^* + H_2O(l) + 2OH^- + 2e^- \leftrightarrow OH^* + 3OH^- + e^- \quad (4)$$

$$OH^* + 3OH^- + e^- \leftrightarrow 4OH^- \quad (5)$$

Using the expression for ΔG as defined below

$$\Delta G = \Delta E + \Delta ZPE - T\Delta S \quad (6)$$

where ΔE, ΔZPE, and ΔS represent the difference in the DFT calculated ground state energy, zero point energy, and entropy corrections, respectively, the free energy of each intermediate reaction was calculated. As an example, the free energy of Reaction (2) (ΔG_2) was calculated as a function of the reversible potential U^o using the following equations

$$\Delta G_2 = \Delta G_{OOH^*} - \Delta G_{O_{2,g}} - \frac{1}{2}\Delta G_{H_2} - kT \ln a_{H^+} + eU^0 \quad (7)$$

$$\Delta G_{OOH^*} = \Delta E_{OOH^*} + \Delta \mathrm{ZPE}_{OOH^*} - T\Delta \mathrm{S}_{OOH^*} \quad (8)$$

The values of ΔZPE used, and further details of the free energy calculation can be found in the previously published references.[113,121].

6.3 Results and Discussion

The mesoporous spheres have been synthesized by a facile solvothermal technique using ammonium bicarbonate as precipitation and pore-forming agent to promote the formation of metal carbonate nanocrystals self-assembled into spherical structures **(Figure 6.1a)**. The heat treatment process in the presence of oxygen (in air) thermally decomposes metal carbonates into metal oxide spheres, releasing CO_2 gas and leaving pores behind[122] as shown by the following equation:

$$3M\text{-}CO_3 + 1/2O_2 \rightarrow M_3O_4 + CO_2$$

where *M* is one or more transition metals used in this study (Co, or Ni and Co, or Mn and Co). The release of CO_2 gas within the spherical metal oxide phase leaving behind pores is very interesting for enhanced electrocatalysis as it increases the active surface area and facilitates mass transport. The three kinds of porous spinel oxide synthesized in this study, Co_3O_4, $(Ni,Co)_3O_4$, and $(Mn,Co)_3O_4$ analyzed by scanning electron microscopy (SEM) have been to reveal their porous spherical morphology **(Figure 6.1b-d)**. Without the addition of ammonium bicarbonate, randomly oriented sheet-like metal oxide structures of varying sizes have been observed **(Figure 6.2)**. Further inspection of higher magnification SEM images of the sphere oxides has revealed nano-sized crystals that self-assembled into a few micron scale spherical structures **(Figure 6.1e-g)**. Interestingly, despite using the same amounts of reagents during the synthesis, including the total amount of transition metal precursors, slightly different sizes of nano-crystals have been observed, due to changes in the crystal lattice structure with the insertion of Ni and Mn into Co_3O_4. For bi-functional catalysis, high surface area

materials are much desirable since ORR and OER are interfacial reactions that occur on the active catalyst’s surface.[123] The surface area of the metal oxides has been measured by conducting Brunauer-Emmett-Teller (BET) analysis, resulting in very high specific surface areas of 132, 66.3, and 162 m^2 g^{-1} obtained with Co_3O_4, $(Ni,Co)_3O_4$, and $(Mn,Co)_3O_4$, respectively. **(Figure 6.3)**. The nitrogen adsorption-desorption isotherms show a hysteresis loop in the region of high relative pressure (Type IV isotherm) due to the presence of mesopores formed by the

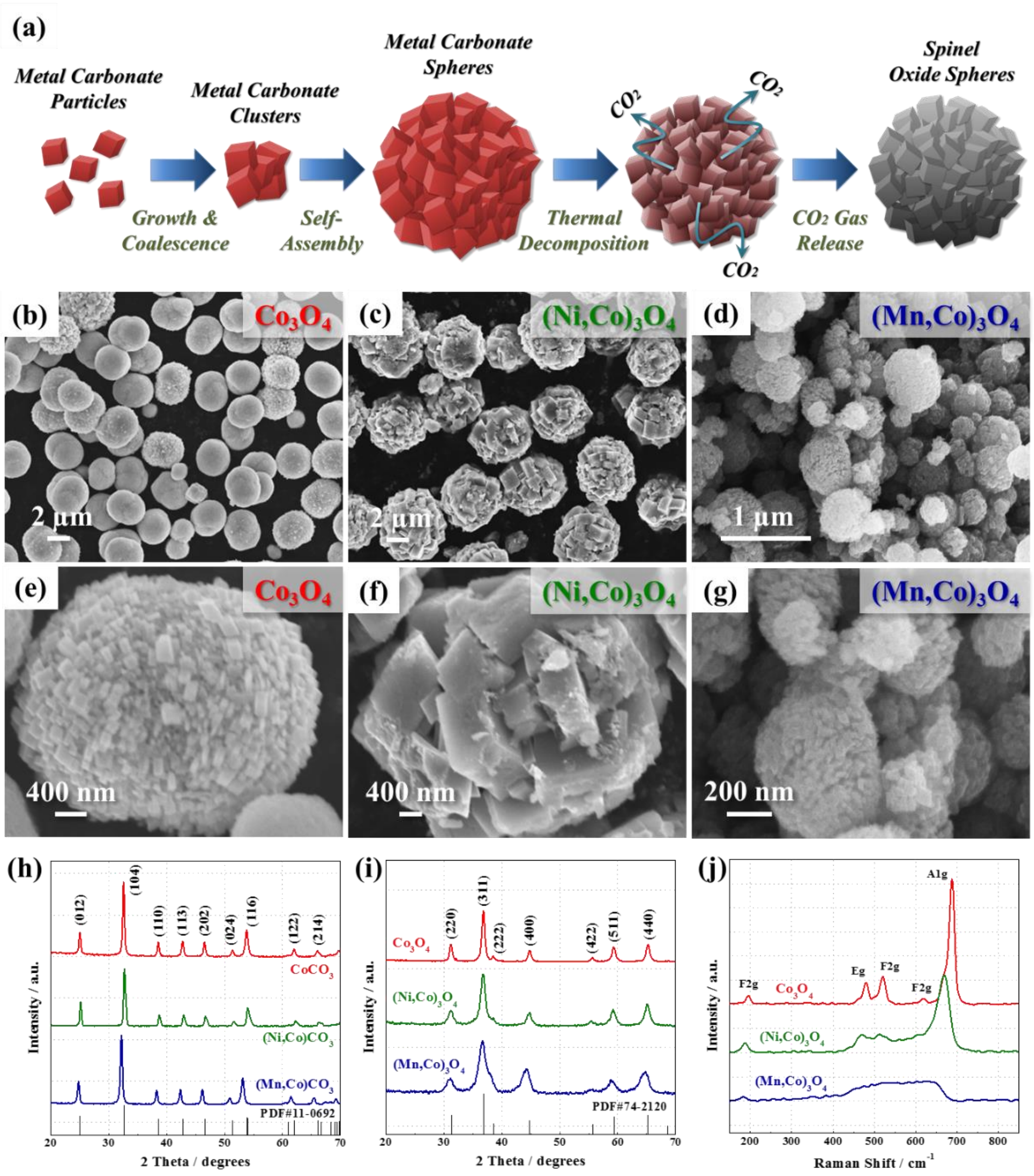

Figure 6.1 (a) Schematic illustration of synthesis of self-assembled mesoporous spinel oxide spheres. SEM images of (b, e) Co_3O_4, (c, f) $(Ni,Co)_3O_4$, and (d, g) $(Mn,Co)_3O_4$ mesoporous spheres. (h) XRD patterns obtained (h) before, and (i) after thermal decomposition, and (j) Raman spectra of Co_3O_4, $(Ni,Co)_3O_4$, and $(Mn,Co)_3O_4$ mesoporous spheres. Reproduced in adapted form from ref. 92 with permission from Wiley.

interparticle spacing between nano-crystals. Based on the pore size distribution obtained by Barrette-Joynere-Halenda (BJH) analysis, the peak pore diameter has been found to be 3.6, 12, and 3.5 nm obtained with Co_3O_4, $(Ni,Co)_3O_4$, and $(Mn,Co)_3O_4$, respectively, which likely corresponds to the size of the interparticle spacing. This mesoporous nature of the sphere is highly beneficial for both ORR and OER since greater specific surface area increases the number of active sites exposed, and the pores can also act as channels to facilitate rapid mass transport of reactants and products during the catalytic reactions. The spinel oxide spheres analyzed by X-ray powder diffraction (XRD) prior to the thermal decomposition of ammonium bicarbonate has resulted in patterns that closely matched with metal carbonates (PDF #11-0692) **(Figure 6.1h)**. After the heat treatment and the release of CO_2, the XRD patterns of the spheres have been found to match very closely with the typical cubic spinel crystal structure (PDF #74-2120) **(Figure 6.1i)**. Interestingly, the peak positions of Ni and Mn have shifted to smaller angles relative to those of Co_3O_4, due to the substitution of Co ions in the native spinel crystal structure with Ni and Mn ions having different ionic radii. As a result, both the *d*-spacing (the (311) orientation used as an example), and the lattice constants (*a*) have been found to increase in the order of Co_3O_4 < $(Ni,Co)_3O_4$ < $(Mn,Co)_3O_4$ **(Table 6.1)**, consistent with observations of other spinel oxides reported in the literature.[124,125] In addition to the XRD analysis, Raman spectroscopy has been conducted to confirm the spinel crystal structure, which showed typical F2g, Eg, and A1g vibrational modes of

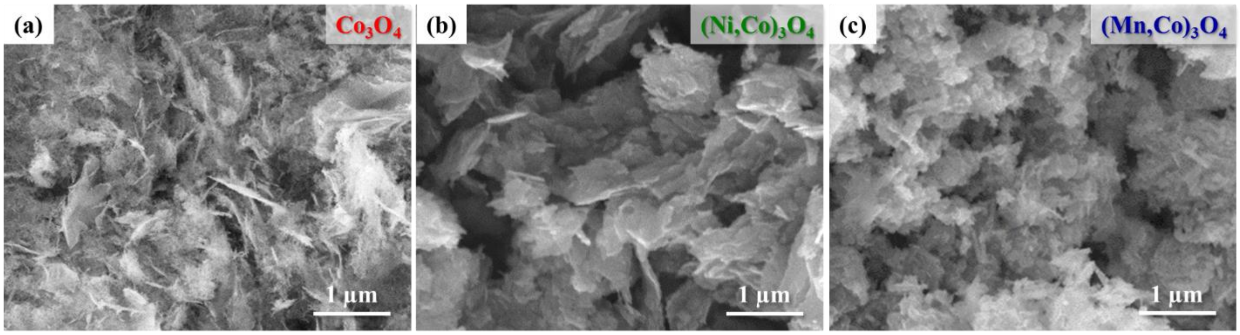

Figure 6.2 (a) Co_3O_4, (b) $(Ni,Co)_3O_4$, and (c) $(Mn,Co)_3O_4$ synthesized without the addition of ammonium bicarbonate. Reproduced in adapted form from ref. 92 with permission from Wiley.

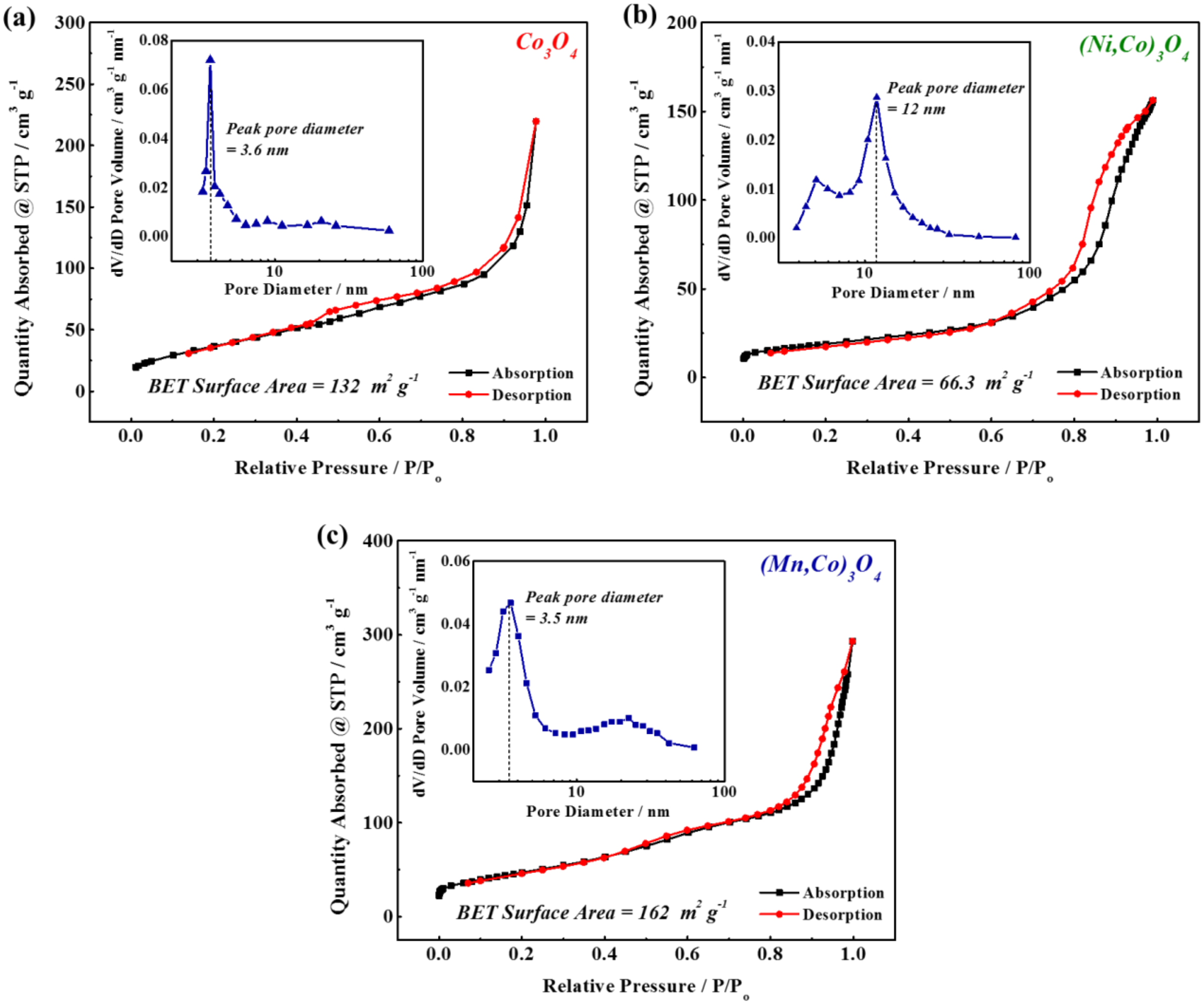

Figure 6.3 Nitrogen adsorption-desorption isotherm and BJH pore size distribution of (a) Co_3O_4, (b) $(Ni,Co)_3O_4$, and (c) $(Mn,Co)_3O_4$. Reproduced in adapted form from ref. 92 with permission from Wiley.

Co_3O_4 **(Figure 6.1j)**.[126] However, these vibrational modes broadened with $(Ni,Co)_3O_4$, and $(Mn,Co)_3O_4$ as a result of less coherent vibrations in mixed transition metal oxides. To verify the composition of the spinel oxide spheres, XPS has been conducted which confirmed the presence of Co 2p with all three spinel oxide spheres in addition to Ni and Mn detected with $(Ni,Co)_3O_4$, and $(Mn,Co)_3O_4$, respectively, based on the XPS survey **(Figure 6.4a)**. Further XPS analysis of these oxides has revealed that the chemical composition at the surface of the catalysts is

Table 6.1 The *d*-spacing of (311) crystal orientation and lattice constants (*a*) of Co_3O_4, $(Ni,Co)_3O_4$, and $(Mn,Co)_3O_4$ based on the results obtained from XRD. Reproduced in adapted form from ref. 92 with permission from Wiley.

	Experimental		Theoretical		
Sample	**(311) plane** *d*-spacing (nm)	**Lattice constant** *a* (Å)	**(311) plane** *d*-spacing (nm)	**Lattice constant** *a* (Å)	**JCPDF** Database Ref.
Co_3O_4	0.2439	8.074	0.2437	8.065	# 74-2120 (Co_3O_4)
$(Ni,Co)_3O_4$	0.2444	8.108	0.2446	8.114	# 73-1702 ($NiCo_2O_4$)
$(Mn,Co)_3O_4$	0.2454	8.192	0.2499	8.290	# 84-0482 ($MnCo_2O_4$)

$Ni_{1.4}Co_{1.6}O_4$, and $Mn_{1.4}Co_{1.6}O_4$. This suggests the transition metal cations occupy both the tetrahedral and octahedral sites. Specifically, de-convoluting the high-resolution Co 2p spectrum of Co_3O_4 (777-811 eV) **(Figure 6.4b)** has revealed splitting of the peak into 2p1/2 (795.0 eV) and 2p3/2 (779.8 eV) doublet due to the presence of cobalt cations having different oxidation states in either the tetrahedral (Co^{II}) or octahedral (Co^{III}) interstitial sites of the spinel lattice.[40] Similarly, the de-convoluted Co 2p and Ni 2p (850-890 eV) of $(Ni,Co)_3O_4$ **(Figure 6.4c, and d, respectively**), and Co 2p and Mn 2p (637-661 eV) of $(Mn,Co)_3O_4$ **(Figure 6.4e, and f, respectively)** have shown peak splitting, confirming the presence of both M^{II} and M^{III} oxidation states of the active transition metal centers. The observation of multiple oxidation states of Co is particularly important for bi-functional catalysis since Co^{II} and Co^{III} are usually considered as the active site for ORR and OER,

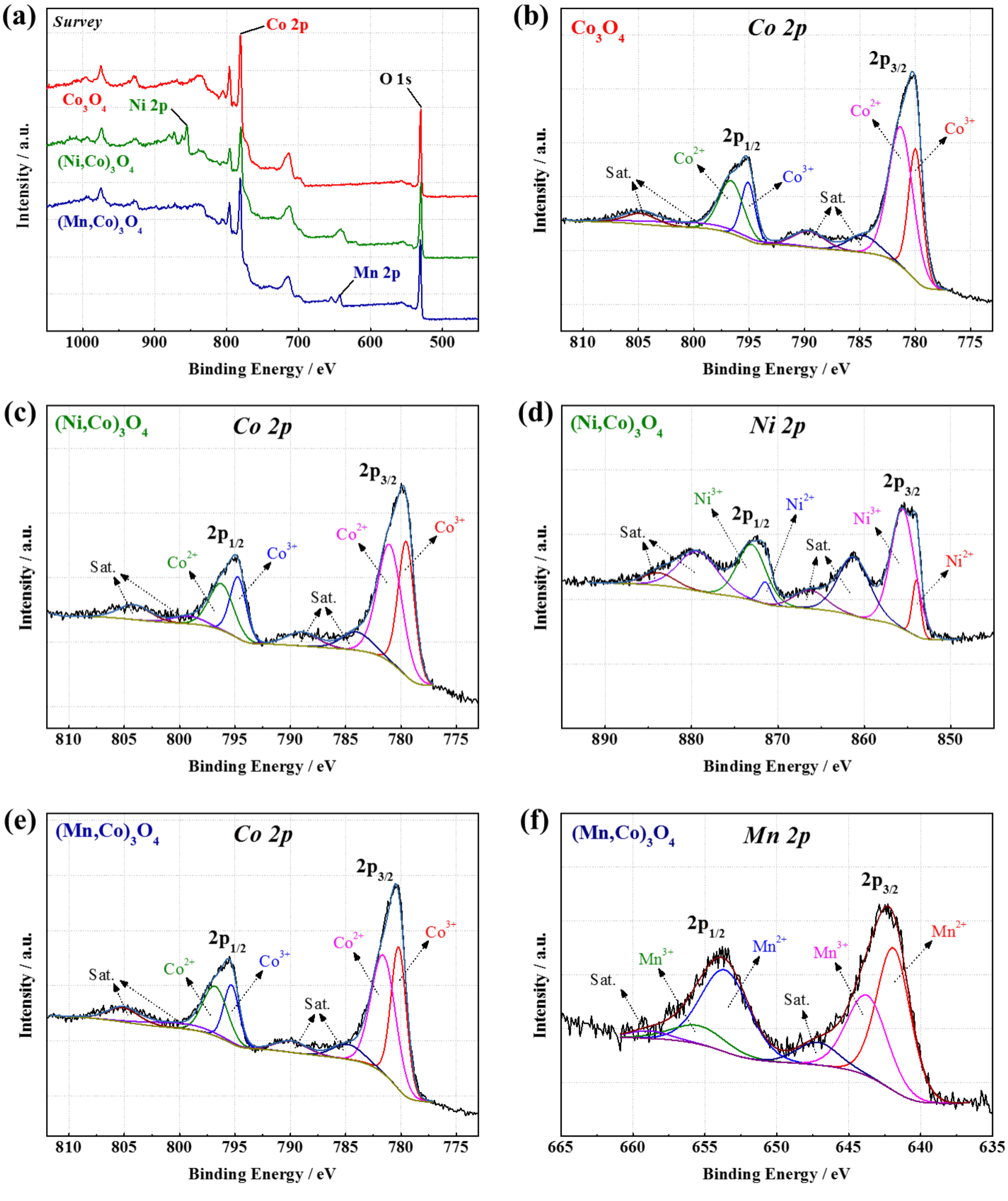

Figure 6.4 (a) Full XPS survey of Co_3O_4, $(Ni,Co)_3O_4$, and $(Mn,Co)_3O_4$. De-convoluted high-resolution XPS spectra: (b) Co 2p of Co_3O_4, (c) Co 2p, and (d) Ni 2p of $(Ni,Co)_3O_4$, and (e) Co 2p, and (f) Mn 2p of $(Mn,Co)_3O_4$. Reproduced in adapted form from ref. 92 with permission from Wiley.

respectively.[105,127] The de-convolution of O 1s spectrum (528-535 eV) obtained with all three spherical oxides has shown three peaks that corresponded to oxygen in the spinel lattice, adsorbed -OH and H_2O, and surface Co^{III} **(Figure 6.5)**, most likely due to the leftover from the thermal decomposition. The peak splitting of the active transition metal centers (Co, Ni, and Mn) observed with all three oxides is important, particularly for bi-functional oxygen catalysis since the multivalent nature of the metal centers in the spinel structure has been consistently reported to allows rapid charge transfer through electron hopping, as well as improved interaction with oxygen intermediates during the oxygen reactions.[40] Having characterized the physical properties of the spinel oxide spheres, their electrochemical activities towards bi-functional ORR and OER have been evaluated by half-cell rotating disk electrode (RDE) voltammetry at various rotation speeds **(Figure 6.6)**. Based on the ORR polarization curves obtained at 1,600 rpm in O_2-saturated 0.1 M

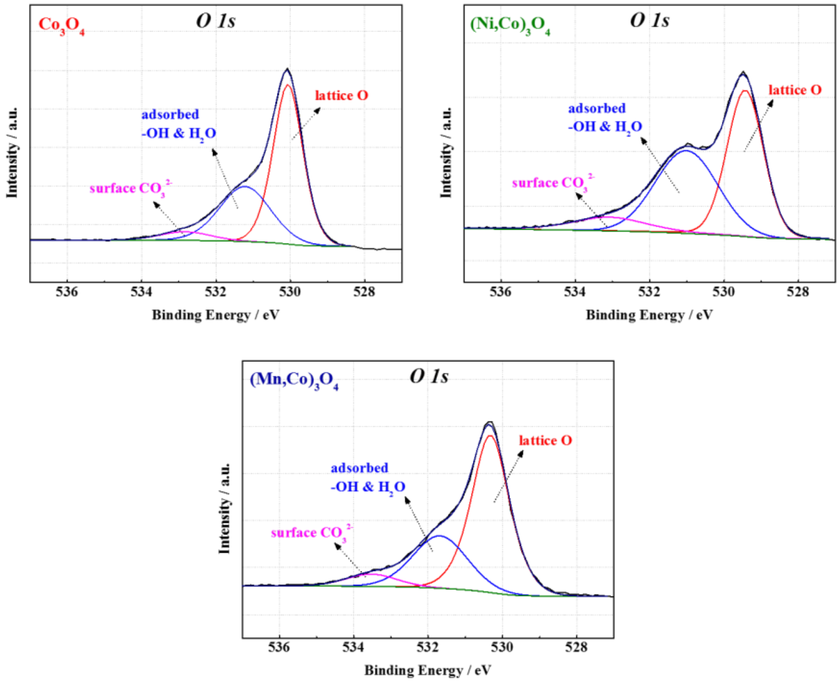

Figure 6.5 De-convoluted high resolution O1s XPS spectra of (a) Co_3O_4, (b) $(Ni,Co)_3O_4$, and (c) $(Mn,Co)_3O_4$. Reproduced in adapted form from ref. 92 with permission from Wiley.

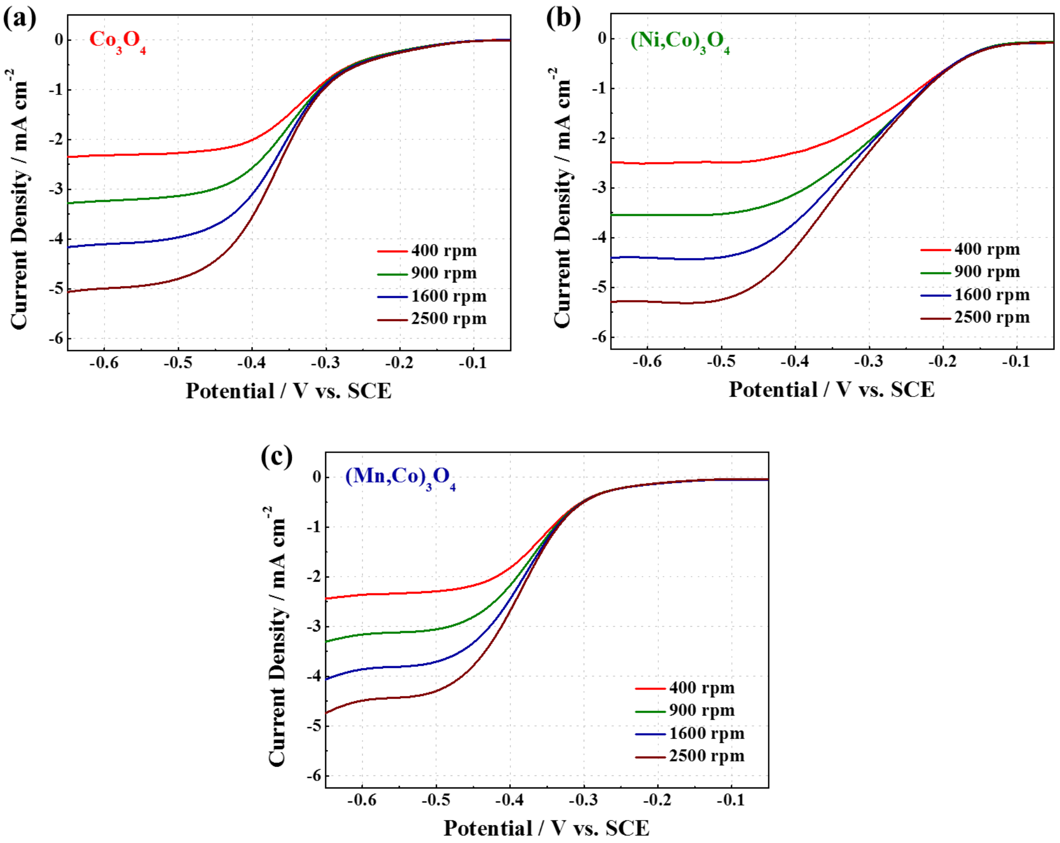

Figure 6.6 ORR polarization curves obtained by RDE voltammetry at various rotation rates in O_2-saturated 0.1 M KOH electrolyte with mesoporous spheres of (a) Co_3O_4, (b) $(Ni,Co)_3O_4$, and (c) $(Mn,Co)_3O_4$. Reproduced in adapted form from ref. 92 with permission from Wiley.

KOH **(Figure 6.7a)**, $(Ni,Co)_3O_4$ is observed to be significantly positive shifted, indicative of superior ORR activity, followed by Co_3O_4 and $(Mn,Co)_3O_4$. In particular, $(Ni,Co)_3O_4$ demonstrates relatively much positive on-set potential (-0.127 V vs. SCE) compared to those of Co_3O_4, and $(Mn,Co)_3O_4$ (-0.171, and -0.217 V, respectively). This signifies a lower activation energy required for $(Ni,Co)_3O_4$ to overcome the barrier of the first electron reaction which is usual known as the rate-limiting step. The same trend is observed with half-wave potentials ($E_{1/2}$), $(Ni,Co)_3O_4$ demonstrating most positively shifted $E_{1/2}$ of -0.292 V compared to -0.355 and -0.378 V obtained

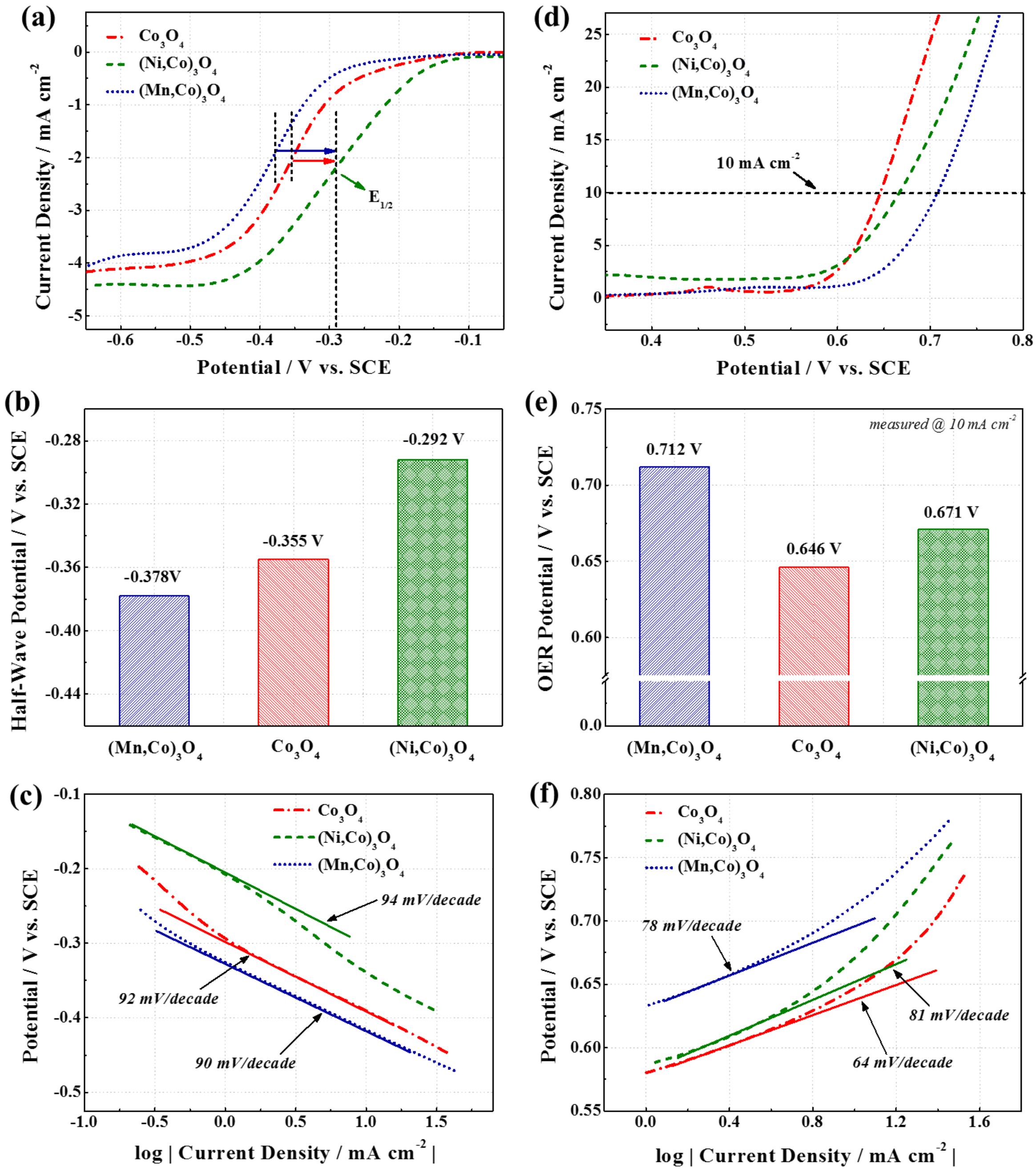

Figure 6.7 (a) ORR polarization curves obtained by RDE voltammetry at rotation rate of 1600 rpm in O_2-saturated 0.1 M KOH, (b) comparison of half-wave potentials, (c) ORR Tafel slopes, (d) OER CV curves obtained in N_2-saturated 0.1 M KOH, (e) comparison of OER potentials at 10 mA cm^{-2}, and (f) OER Tafel slopes of Co_3O_4, $(Ni,Co)_3O_4$, and $(Mn,Co)_3O_4$. Reproduced in adapted form from ref. 92 with permission from Wiley.

with Co_3O_4 and $(Mn,Co)_3O_4$, respectively **(Figure 6.7b)**. Further investigation by Tafel analysis reveals that the three oxides results in comparable slopes in the range of 90 to 94 mV/decade **(Figure 6.7c)**, which suggests that the ORR on these catalysts proceed at similar rates of kinetics even though the energy requirements for overcoming the first electron reaction are different. As such, introducing active metal substituents (Ni, Mn) into the pristine Co_3O_4 spinel lattice affects mostly the degree of binding with oxygen and the formation of first reduced oxygen species[113], while the rest of the intermediate reactions proceed at similar kinetic rates. In addition to the ORR activity, the OER activity of the spinel oxides has been evaluated, resulting in $(Ni,Co)_3O_4$, and Co_3O_4 with very similar on-set potentials (~0.60 V), and $(Mn,Co)_3O_4$ with a more positive shifted (less active) on-set potential (0.65 V) **(Figure 6.7d)**. Despite demonstrating similar on-set potentials, Co_3O_4 has resulted in a slightly more negative (more active) OER potential (E_{OER}) of 0.646 V measured at 10 mA cm^{-2} compared to those of $(Ni,Co)_3O_4$, and $(Mn,Co)_3O_4$ (0.671 and 0.712 V) **(Figure 6.7e)**. The OER Tafel analysis of Co_3O_4 has resulted in the lowest slope of 64 mV/decade, followed by 81 and 78 mV/decade obtained with $(Ni,Co)_3O_4$, and $(Mn,Co)_3O_4$, respectively **(Figure 6.7f)**, indicative of more rapid OER kinetics of Co_3O_4 despite demonstrating similar on-set potential as $(Ni,Co)_3O_4$. For both ORR and OER, relatively lower activity and kinetics observed with $(Mn,Co)_3O_4$ is most likely due to its least favorable interaction with oxygen intermediates as a result of lattice expansion and broadened vibrational modes observed by XRD and Raman analyses, respectively. The differences in the ORR and OER activities of the metal oxides also suggests that they are clearly dependent on the type of transition metal substituent inserted into the spinel oxide structure. To confirm this, double layer capacitance has been measured as the slope of current versus scan rate plot obtained by conducting CV at various scan rates in a potential window where no Faradaic redox occurs **(Figure 6.8)**. The double layer

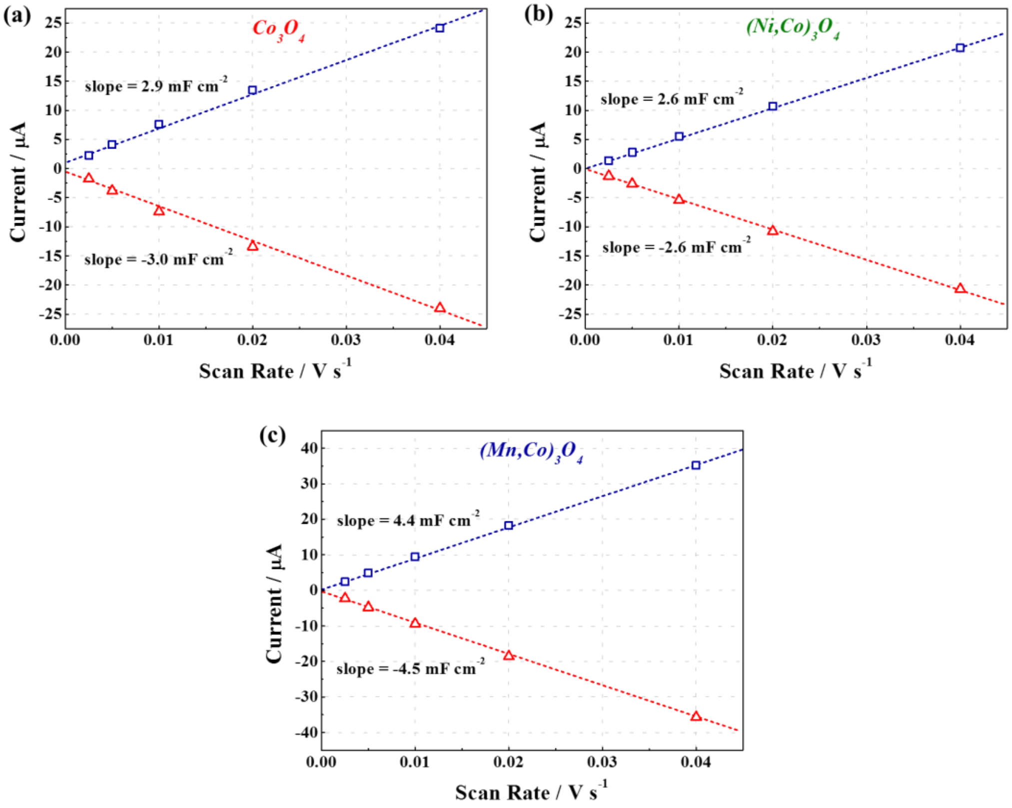

Figure 6.8 Current versus scan rate plots of (a) Co_3O_4, (b) $(Ni,Co)_3O_4$, and (c) $(Mn,Co)_3O_4$ obtained by conducting CV at various scan rates (2.5, 5, 10, 20, 40 mV s^{-1}) in 0.1 M tetrabutylammonium hexafluorophosphate in acetonitrile over a 60 mV potential window around the open circuit potential (blue: positive sweep, red: negative sweep). The slope of the plot is equal to the double layer capacitance normalized to the area of the working electrode, which is related to the electrochemically active surface area (ECSA). Reproduced in adapted form from ref. 92 with permission from Wiley.

capacitance has been reported to be linearly proportional to the electrochemically active surface area (ECSA) of metal oxides.[128-130] Interestingly, the measured capacitance values of 2.9, 2.6, and 4.4 mF cm^{-2} obtained with Co_3O_4, $(Ni,Co)_3O_4$, and $(Mn,Co)_3O_4$, respectively, show the same trend as the BET surface area results ($(Ni,Co)_3O_4 < Co_3O_4 < (Mn,Co)_3O_4$), confirming the validity of the surface areas measured in this study. The differences in the surface area of the metal oxides however are found to have less dominant effect on the catalytic activity towards ORR and OER compared to the compositional effect demonstrated by introducing Ni and Mn transition metal substiuents into the spinel oxide structure. This leads to $(Ni,Co)_3O_4$ demonstraing the least potential difference between ORR and OER despite exhibiting the smallest BET surface area and double layer capacitance. Specifically, $(Ni,Co)_3O_4$ demonstrates the best overall bi-functional catalytic activity with the least potential difference ($\Delta E_{OER-ORR} = 1.01$ V) between the ORR and OER potentials measured at the current densities -3 mA cm^{-2} and 10 mA cm^{-2}, respectively. Based on the literature survey, the ORR/OER potential difference is found to be smaller in comparison to many reports, and even comparable to some of the best published results on non-precious transition metal oxide based bi-functional catalysts.[55,131-133] The activity enhancement is attributed to the insertion of Ni cations into the octahedral sites of the spinel lattice, which has been reported to improve the electrical conductivity of the spinel oxide.[116] On the other hand, the catalytic activity of Co_3O_4 largely favors OER, leading to reduced OER overpotential and the generation of high current densities. This is attributed to relatively weak adsorption energy between oxygen adsorbate and the surface of active Co cations, promoting release of oxygen during OER.[134] This in reverse reduces the ORR activity due to the weak binding and insufficient energy to activate adsorbed oxygen. The high bi-functional catalytic activities of the spinel oxide spheres, in comparison to commercially available Co_3O_4 nanoparticle catalyst, have been highlighted by much improved ORR (positive shifted) and OER (negative shifted) potentials **(Figure 6.9)**. However, in comparison to a mixture of precious metal Pt/C + Ir/C benchmark catalyst, the spinel oxide spheres have demonstrated relatively weaker bi-functional activities. This sacrificed activity is currently the main trade-off of utilizing inexpensive non-precious transition metal based catalysts as

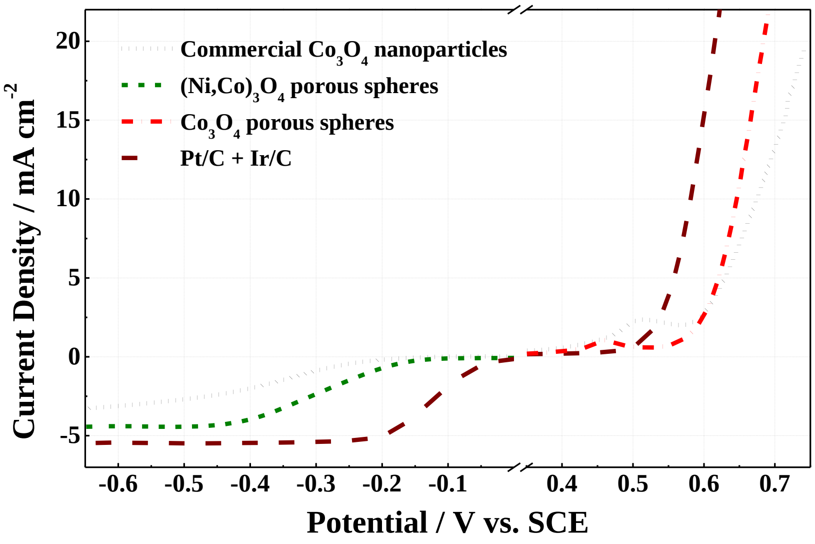

Figure 6.9 Comparison of the ORR and OER activities of $(Ni,Co)_3O_4$ and Co_3O_4, respectively, to commercial Co_3O_4 nanoparticle, and precious-metal Pt/C + Ir/C. Reproduced in adapted form from ref. 92 with permission from Wiley.

opposed to the precious ones, and can be minimized by hybridizing with nanostructured active carbon to synergistically improve both ORR and OER performances.

To provide further insight into the bi-functional electrochemical behaviours of the spinel oxides, the first-principles DFT calculations has been conducted by modeling their cubic Fd3m space group lattice in a periodic two-layer slabs with a (2x2) unit cell **(Figure 6.10)**. In the spinel lattices of $(Ni,Co)_3O_4$ and $(Mn,Co)_3O_4$, Ni and Mn ions are known to preferentially occupy the octahedral interstitials sites, whereas Co ions are distributed over both octahedral and tetrahedral sites. Therefore, $(Ni,Co)_3O_4$ and $(Mn,Co)_3O_4$ have been modeled by exchanging half of the octahedral Co ions with Ni or Mn in Co_3O_4[9]. During ORR and OER, the metal oxide surfaces undergo changes due to the interaction with different oxygen intermediates (i.e. *OOH, *O, and *OH) (Figure 4a, b, and c, respectively). The band diagram shows the changes in the Gibbs free energy (ΔG) of the spinel oxides during interactions with each of these intermediates at zero

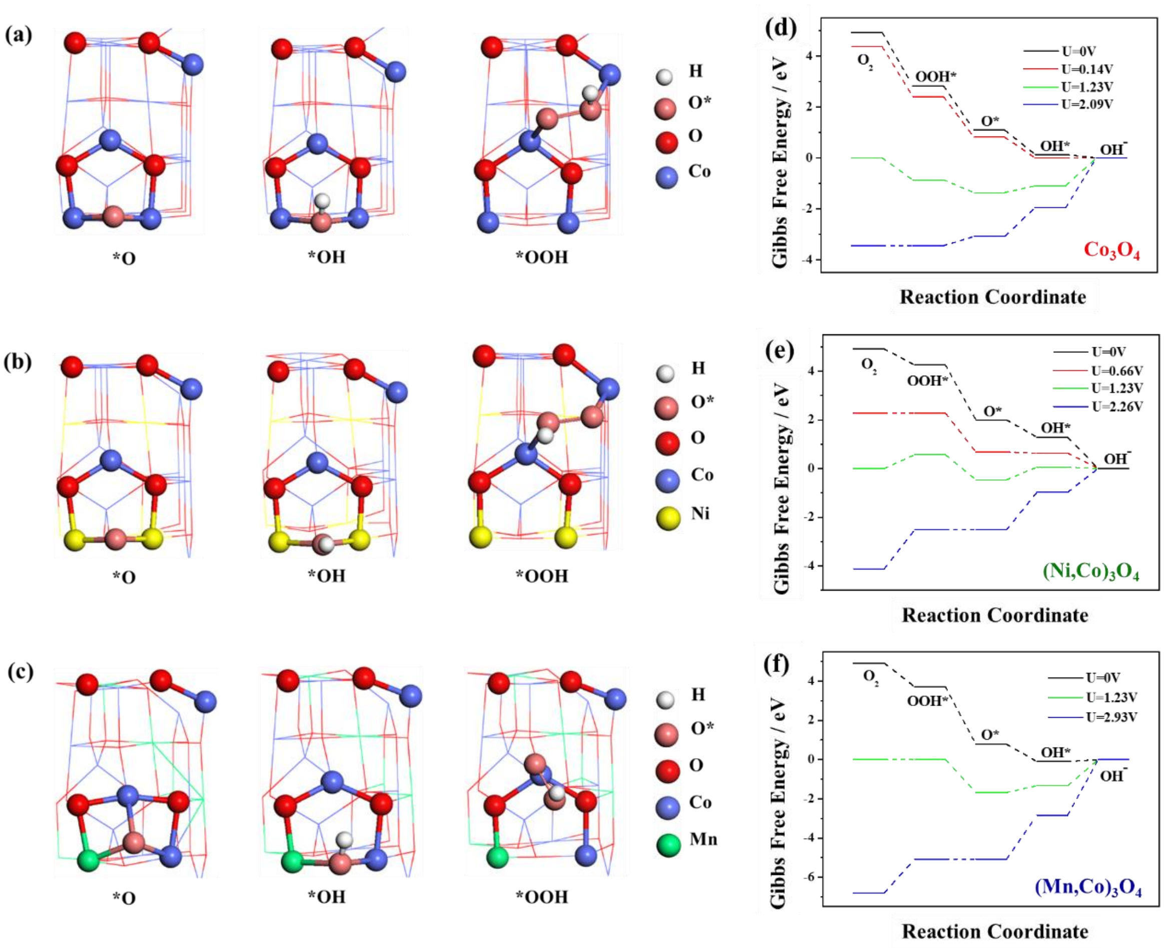

Figure 6.10 Periodic six atomic layer slabs with a (2×2) unit cell of (a) Co_3O_4, (b) $(Ni,Co)_3O_4$, and (c) $(Mn,Co)_3O_4$, depicting interaction between oxygen intermediates and the catalyst surface during ORR/OER. (d-f) Standard free energy band diagrams obtained at zero potential (U = 0 V), equilibrium potential (U = 1.23 V), and the potential at which all intermediates proceed spontaneously at pH 14 and T = 298 K. All potentials are indicated *vs. reversible hydrogen electrode (RHE)* unless otherwise noted. Reproduced in adapted form from ref. 92 with permission from Wiley.

potential (U = 0 V), equilibrium potential (U = 1.23 V), and the potential at which all oxygen intermediates proceed spontaneously **(Figure 6.10d-f)**. Based on this band energy calculations, the limiting thermodynamic potential where all steps proceed downward has been found to be U

= 0.14 and 0.66 V with Co_3O_4 and $(Ni,Co)_3O_4$, respectively. However, with $(Mn,Co)_3O_4$, the energy of the intermediate reaction corresponding to the reduction of OH* to OH^- has remained slightly thermodynamically upward even at U = 0 V. These calculations then predict the degree of the ORR activity of the spinel oxides to be in the order of $(Mn,Co)_3O_4 < Co_3O_4 < (Ni,Co)_3O_4$, which parallels the activity trend observed experimentally **(Figure 6.11a)**. Specifically, $(Ni,Co)_3O_4$ having demonstrated the highest U potential has shown the most positively shifted on-set and half-wave ORR potentials, while a lower U potential of Co_3O_4 matched with relatively negative shifted ORR potentials. Lastly, the lowest U potential obtained with $(Mn,Co)_3O_4$ matched with further negative shifted ORR potentials obtained experimentally. To predict the OER activities of the spinel oxides, potentials greater than 1.23 V have been applied to find the point at which all free energies associated with OER intermediate reactions proceeded spontaneously, resulting in U = 2.09, 2.26 and 2.93 V obtained with Co_3O_4, $(Ni,Co)_3O_4$, and $(Mn,Co)_3O_4$, respectively. The lowest U potential of Co_3O_4 is an indication that it exhibits superior OER activity

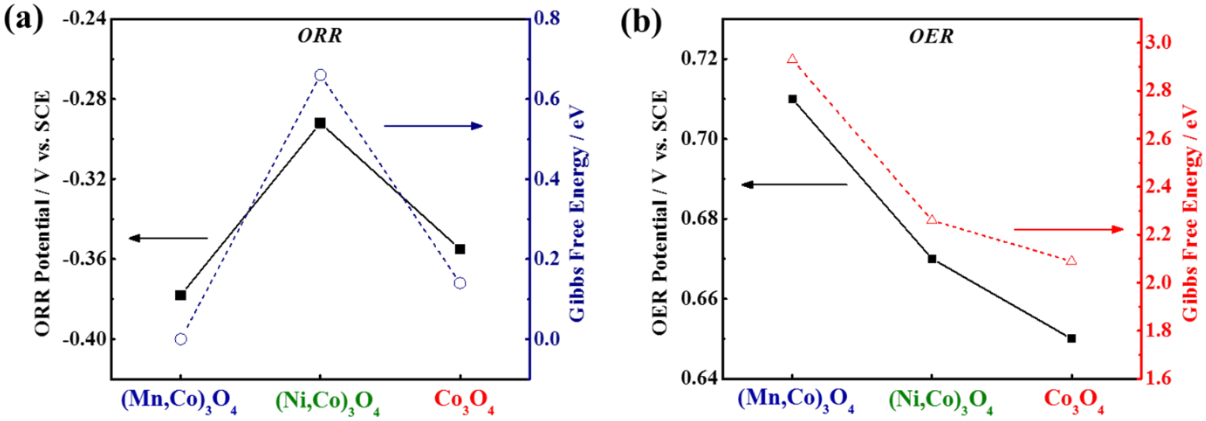

Figure 6.11 Comparisons of (a) ORR half-wave potentials, and (b) OER potentials measured at 10 mA cm^{-2} obtained experimentally with Gibbs free energies obtained from DFT computational analysis of Co_3O_4, $(Ni,Co)_3O_4$, and $(Mn,Co)_3O_4$. Reproduced in adapted form from ref. 92 with permission from Wiley.

followed by $(Ni,Co)_3O_4$ and $(Mn,Co)_3O_4$. These DFT predictions are also in good agreement with the OER potentials obtained experimentally at 10 mA cm^{-2} **(Figure 6.11b)**. Despite relatively smaller activity difference (as well as U potential difference), Co_3O_4 outperforming $(Ni,Co)_3O_4$ suggests that the adsorption strength between oxygen intermediates and active metal cations has a greater effect on the overall OER activity than the electrical conductivity enhancement. As OER is a reverse reaction of ORR, Co_3O_4 which demonstrated a lower ORR activity due to weaker adsorption with oxygen can be expected to more readily release oxygen during OER. $(Mn,Co)_3O_4$ having demonstrated the least ORR and OER activities likely stabilizes oxygen intermediates to the extent that they become inactive for the reactions to further proceed. However, $(Mn,Co)_3O_4$ can still be deemed a suitable catalyst for less energy intensive applications as the abundance of Mn makes it a much more cost-competitive alternative to Co.

6.4 Summary

In this study, spinel oxide structured nano-crystals self-assembled into mesoporous spheres have been synthesized as bi-functional catalysts active towards oxygen reduction reaction (ORR) oxygen evolution reaction (OER). Experimentally, increasing ORR activity trend has been observed in the order of $(Mn,Co)_3O_4 < Co_3O_4 < (Ni,Co)_3O_4$ in terms of on-set and half-wave potentials, while increasing OER activity trend has been observed in the order of $(Mn,Co)_3O_4 < (Ni,Co)_3O_4 < Co_3O_4$ in terms of potential measured at the current density of 10 mA cm^{-2}. The first-principles density functional theory (DFT) analysis of the catalysts has revealed the same activity trends for both ORR and OER based on the Gibbs free energy obtained at the potential for which all intermediate reactions occur spontaneously. The superior ORR activity of $(Ni,Co)_3O_4$ is attributed to the enhanced electrical conductivity due to the insertion of Ni ions into the octahedral interstitials of spinel lattice promoting rapid charge transfer during the electrocatalytic reaction. The superior OER activity of Co_3O_4 is attributed to favorable adsorption strength between oxygen intermediates and active Co cations, facilitating rapid release of evolved oxygen. On the other hand, $(Mn,Co)_3O_4$ has demonstrated relatively lower ORR and OER activities most likely due to lattice expansion and incoherent vibrational modes observed by XRD and Raman analyses, respectively, resulting in over-stabilization and deactivation of oxygen intermediates. The relationship between the composition of spinel oxide catalysts, and the degree of ORR and OER activities investigated in this study by both experiment and computational analysis provides an excellent selection criterion for appropriately choosing a bi-functional catalyst based on the energy requirements of specific applications.

7. Advanced Three-Dimensional Bifunctional Air Electrodes

This chapter is reprinted in adapted form from the below article[49] with permission from Wiley.

D. U. Lee, J. Y. Choi, K. Feng, H. W. Park, Z. Chen, "Advanced Extremely Durable 3D Bifunctional Air Electrodes for Rechargeable Zinc-Air Batteries", Advanced Energy Materials, 4 (2014) 1301389.

7.1 Introduction

The conventional preparation of air breathing cathodes for zinc-air batteries requires physical deposition of active material onto a carbon gas diffusion layer (GDL) by methods such as drop-casting or spray-coating,[135-137] using ancillary materials such as carbon black, pore forming agent and polymer binders. However for rechargeable battery applications, carbon present in the air electrode is subjected to electrochemical oxidation due to the high charging potentials, resulting in electrode degradation, catalyst detachment and overall reduced battery cycle life.[138,139] To address these issues faced by the conventional air electrodes, the use of ancillary materials during electrode preparation has been completely circumvented by directly growing active Co_3O_4 NW arrays onto the surface of stainless steel (SS) mesh current collector. The direct growth has several advantages over the conventional methods. Firstly, Co_3O_4 NW directly grown on SS mesh current collector drastically simplifies the electrode design and fabrication procedure since time-consuming physical deposition processes are no longer required, allowing highly practical and scalable preparation of air electrodes. Secondly, the electrode fabricated without the addition of non-conductive ancillary binding materials demonstrates enhanced electrical property, and improves the electrochemical stability since the decomposition of binding material is completely avoided. Lastly, SS mesh not only acts as a support for the growth of Co_3O_4 NW, but also plays as a current collector. This greatly simplifies the electrode design and in turn reduces the resistance normally associated with interfaces inside an electrode. Using the advanced catalyst/current collector electrode and the atmospheric air as the source of fuel instead of pure purged oxygen, remarkable durability of a practical zinc-air battery has been observed, which will be further discussed in the following sections.

7.2 Experimental Methods

7.2.1 Co_3O_4 Nanowire Growth

A piece of SS mesh (2.5 cm by 4.0 cm) soaked in 6.0 M HCl for 1 hour is rinsed with double de-ionized (DDI) water then dried with nitrogen. The precursor solution is prepared by the addition of $Co(NO_3)_2 \cdot 6H_2O$ (10 mmol) and NH_4NO_3 (5 mmol) into a mix of 35 mL DDI water and 15 mL ammonium hydroxide (30 wt %). The solution is stirred at room temperature for 10 minutes then pre-heated in an oven at 90 ^oC for 2 hours. The pre-treated SS mesh is submerged into the pre-heated precursor solution and kept at 90 ^oC for 12 hours. After the reaction, the mesh removed from the solution is thoroughly rinsed with DDI water then dried with nitrogen stream. The mesh is then heated to 300 ^oC in air at a temperature ramp of 1 ^oC min^{-1} and dwelled for two hours. The furnace is naturally cooled to room temperature then the mesh is ultrasonicated 10 seconds in ethanol before conducting the electrochemical testing.

7.2.2 Rechargeable Zinc-Air Battery Fabrication and Testing

The single-cell battery performance is tested using a home-made practical zinc-air battery and a multichannel potentiostat (Princeton Applied Research, VersaSTAT MC). A polished zinc plate (Zinc Sheet EN 988, OnlineMetals) and Co_3O_4 NW directly grown on SS mesh (Super fine

#500 E-Cig 25 micron, The Mesh Company) are used as the anode and cathode, respectively. A Teflon-coated carbon fibre paper as a backing layer is placed next to the SS mesh to prevent electrolyte leakage. Microporous membrane (25 µm polypropylene membrane, Celgard 5550) and 6.0 M KOH are used as a separator and electrolyte, respectively. The area of the active material layer exposed to the electrolyte is 2.84 cm^2. For comparison, cathodes consisting of Co_3O_4 NW (scrapped off from the SS mesh) and 20 wt % commercial Pt/C are spray-coated using an air brush onto a GDL with a loading of ca. 1.5 mg cm^{-2}, consistent with the average loading of Co_3O_4 NW directly grown on SS mesh. Briefly, 15 mg of active material is dispersed in 1 mL of isopropyl alcohol by sonication for 30 minutes. Then 107 µL of 5 wt. % Nafion solution is added followed by 1 hour of additional sonication. The catalyst mixture is sprayed onto the GDL then dried in an oven at 60 ^oC for 1 hour. The catalyst loading is determined by measuring the weight of the GDL before and after spray-coating. The discharge and charge polarization and power density plots are obtained by a galvanodynamic method with a current density ranging from 0 to 200 mA. The charge-discharge pulse cycling is conducted by a recurrent galvanic pulse method with a fixed current of 50 mA with each cycle being 10 minutes (5 minute discharge followed by 5 minute charge). The extended cycling is carried out by the same method but each cycle being 6 hours (3 hour discharge followed by 3 hour charge). The zinc plate is replaced every 20 cycles to study the durability of air cathode without the failure of battery due to the anode. Electrochemical impedance spectroscopy is conducted with a direct current (DC) voltage fixed at an ORR potential of 0.8 V with an alternating current (AC) voltage of 20 mV ranging from 100 kHz to 0.1 Hz to obtain the Nyquist plots.

7.3 Results and Discussion

The facile template-free method is used to grow mesoporous Co_3O_4 NW array directly onto a SS mesh current collector to be used as an air cathode in rechargeable zinc-air batteries without further processing **(Figure 7.1a)**. The bare SS mesh current collector is observed to be densely coated with Co_3O_4 NW after the growth, creating 3D binder-free, and self-standing NW array **(Figure 7.1b, and c, Figure 7.2a, and b)**. Co_3O_4 NW consists of average diameter and length of 300 nm and 15 µm, respectively, and they exhibit rounded surface modulation, and grow in random directions with some wires crossing each other **(Figure 7.1d)**. The self-standing nature of NW array not only increase the active surface area, but also allow better diffusion of reactants through the empty spaces between the neighbouring NWs[140]. Unlike most template-assisted growth of NW arrays, a simple chemical route employed here produces uniform and dense Co_3O_4 NW array over large areas, which leads to high surface area per unit volume for enhanced electrocatalytic oxygen reactions **(Figure 7.1e)**. Interestingly, the Co_3O_4 NWs are actually tubular with a circular hollow centre of diameter 50 nm **(Figure 7.1f)**, which is ascribed to the Kirkendall effect during the formation of the NW.[141] The inspection of SS mesh edge reveals a directly coupled NW array to the SS current collector **(Figure 7.2c)**. The coupling allows a direct transfer of charges from the site of the electrocatalytic reaction to the current collector, greatly enhancing the charge transfer properties of the electrode.[140] In addition, every NW is able to undergo an efficient electrochemical reaction since they are individually in contact with the current collector, resulting in a high active material utilization.[140,142] Further TEM analysis reveals that the NW is actually mesoporous **(Figure 7.1g, and Figure 7.3a, and b)**, which have been also confirmed by BET analysis by a Type IV isotherm **(Figure 7.4)**, resulting in BET surface area of 22 m^2 g^{-1}. The HR-TEM image reveals fringes in multiple directions **(Figure 7.1h)**, and the crystal structure of the NW analyzed

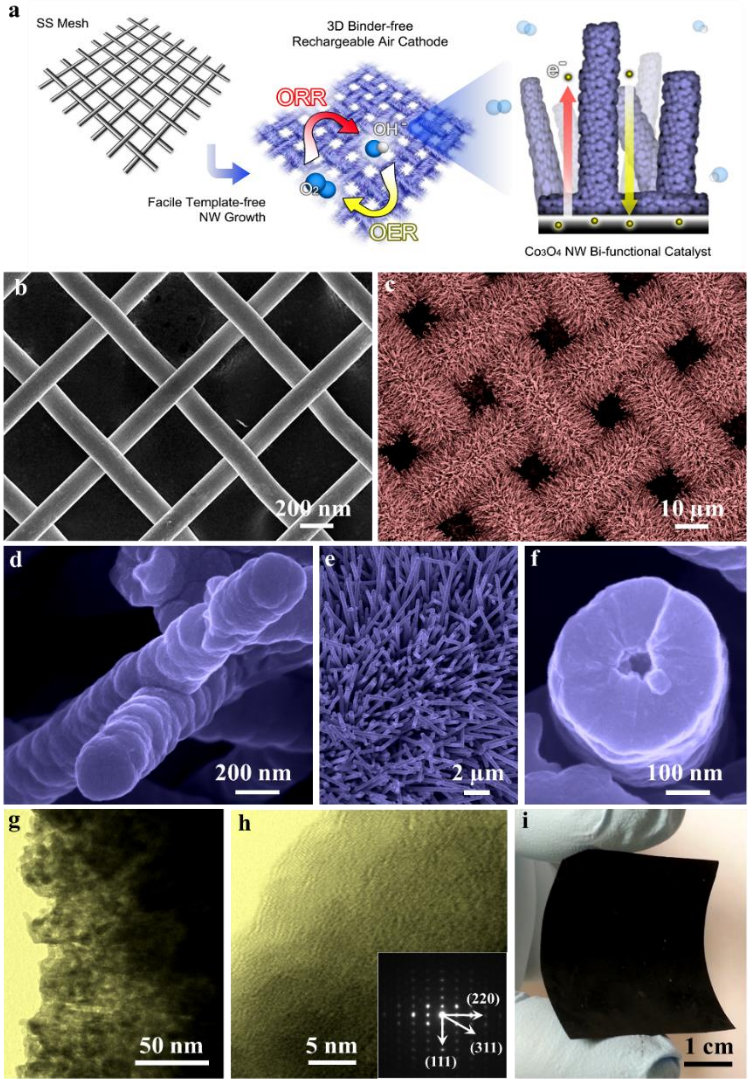

Figure 7.1 (a) Schematic illustration of the growth of 3D rechargeable Co_3O_4 NW air cathode for bi-functional catalysis of ORR and OER. SEM images of (b) SS mesh current collector prior to the growth, (c) densely coated Co_3O_4 NW array, (d) surface morphology of Co_3O_4 NW, (e) self-standing Co_3O_4 NW array, and (f) cross-section of Co_3O_4 NW. (g) TEM image of mesoporous Co_3O_4 NW wall. (h) HR-TEM image of the Co_3O_4 NW wall (inset: FFT pattern of Co_3O_4 NW exhibiting polycrystallinity). (i) Optical image of flexible as-grown Co_3O_4 NW air electrode. Reproduced in adapted form from ref. 49 with permission from Wiley.

by Fast Fourier Transformation (FFT) reveals (111), (211), and (220) crystal orientations of a cubic spinel Co_3O_4 **(Figure 7.1h, inset)**, indicative of the polycrystalline nature of the NW. In addition to the aforementioned advantages, the mechanical flexibility of the SS mesh allows bending of the electrode, which is interesting for the development of flexible device applications **(Figure 7.1i)**. The XRD pattern and Raman spectrum obtained with Co_3O_4 NW array has shown peaks that indicate successful synthesis of cubic spinel crystal structure **(Figure 7.5)**, consistent with the above FFT analysis.[143] Raman spectroscopy has revealed peaks that correspond to the vibration modes of a cubic spinel Co_3O_4 (E_g, F_{2g}, and A_{1g}).[144] These physical characterizations confirm successful growth of Co_3O_4 NW by the facile synthesis technique employed in the present work.

The active sites of Co_3O_4 NW for the catalytic oxygen reactions have been investigated by XPS **(Figure 7.6)**. As expected, the full spectrum of the NW reveals binding energies of the peaks that correspond to the Co 2p (774-812 eV) and O 1s (527-536 eV) species in Co_3O_4, respectively.[3] The de-convolution of high resolution Co 2p spectrum has revealed two spin-orbit of $2p_{1/2}$ and $2p_{3/2}$ configurations each consisting of Co^{3+} and Co^{2+} cation doublet.[4] The bi-functional catalytic activity of Co_3O_4 NW towards both ORR and OER are attributed to the mixed valencies of the Co

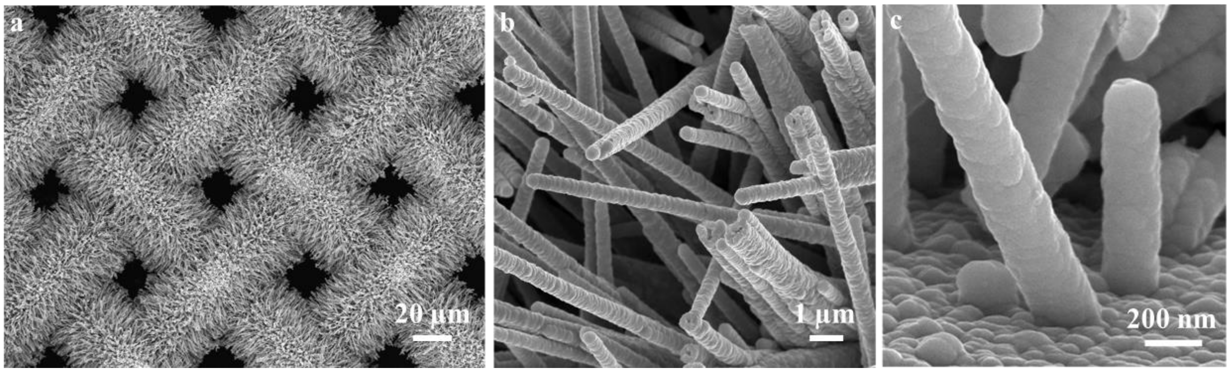

Figure 7.2 SEM images of (a,b) Co_3O_4 NW array prior to heat treatment, and (c) the stem of Co_3O_4 NW directly coupled to the SS mesh. Reproduced in adapted form from ref. 49 with permission from Wiley.

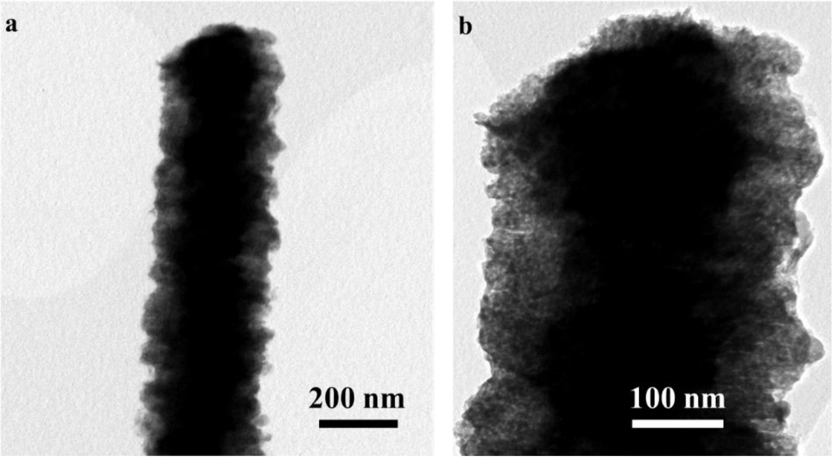

Figure 7.3 (a, b) TEM images of Co_3O_4 NW. Reproduced in adapted form from ref. 49 with permission from Wiley.

cation coexisting in the same cubic spinel providing donor-acceptor chemisorptions sites for the reversible oxygen adsorption and desorption[4]. Furthermore, the electron transfer occurs by hopping processes between the cations of different valencies which has relatively low activation energy, resulting in Co_3O_4 having relatively high electrical conductivity. These excellent electronic properties of cubic spinel Co_3O_4 make it an excellent candidate as a highly efficient catalyst for rechargeable zinc-air battery applications.

To investigate the catalytic activity of the advanced SS mesh electrode, a single-cell practical zinc-air battery has been used to demonstrate its performance in natural air (instead of pure oxygen). Superior discharge and charge potentials of the advanced SS mesh electrode are apparent in the galvanodynamic discharge and charge polarization profiles beyond 20 mA cm^{-2} **(Figure 7.7a)**. However, at lower current densities, the conventional GDL electrode sprayed-coated with Co_3O_4 NW shows a comparable performance to that of the SS mesh electrode due to sufficiently low rate of reaction. The superior performance of the advanced SS mesh electrode at higher current densities is attributed to the hierarchical Co_3O_4 NW array with mesoporous

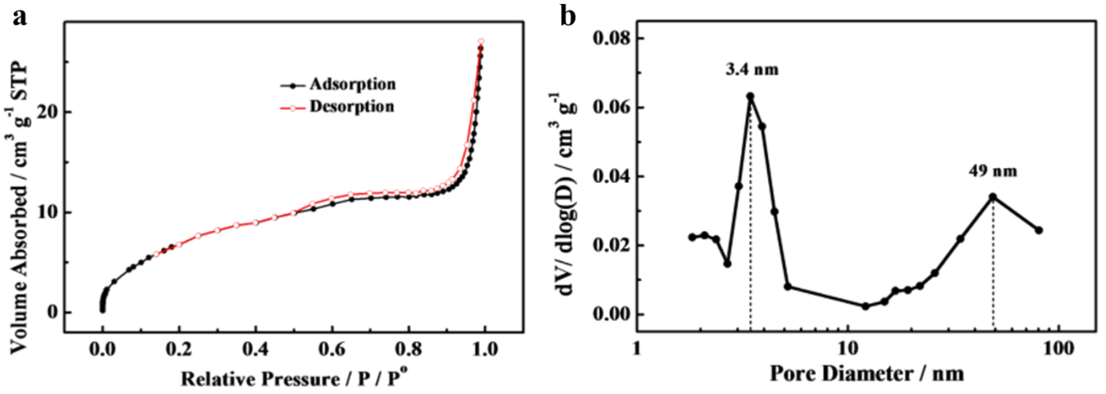

Figure 7.4 (a) Nitrogen adsorption-desorption isotherm, and (b) pore size distribution of Co_3O_4 NW. Reproduced in adapted form from ref. 49 with permission from Wiley.

morphology and the direct coupling of each NW onto the current collector for enhanced active material utilization and rapid charge transfer during the catalytic oxygen reactions. In the conventional GDL electrode, however, polymer binders used during the electrode preparation introduces highly undesirable interfaces, which reduces the surface utilization, resulting in inefficient electrocatalysis. Physically deposited material is also subjected to particle aggregation, which leads to the loss of active surface area and hindering the accessibility of electrolyte to the active material.[145] Furthermore, physical deposition leads to random orientations of the active

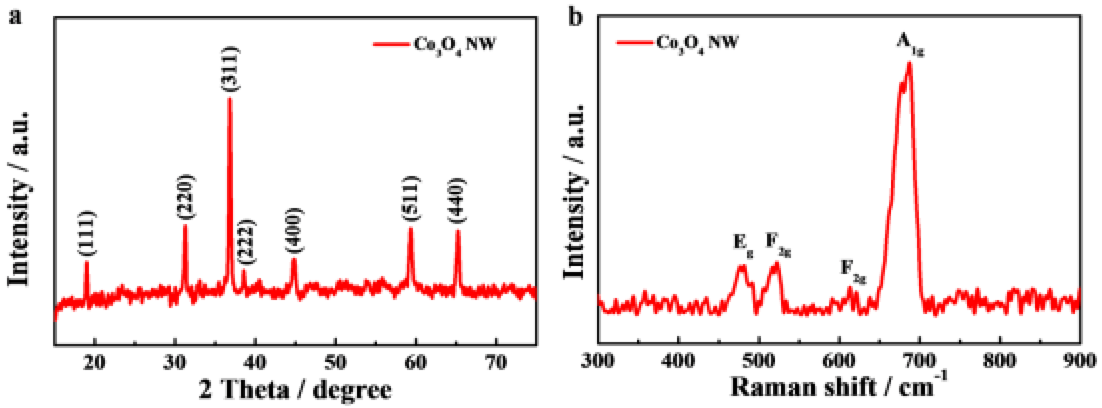

Figure 7.5 (a) The XRD pattern, and (b) Raman spectrum obtained with Co_3O_4 NW array. Reproduced in adapted form from ref. 49 with permission from Wiley.

material, which loses the morphological benefit of nanosized array architecture. The state-of-art commercial Pt/C catalyst sprayed on a GDL demonstrates comparable discharge performance, but a significantly inferior charge performance. The rechargeability of the electrodes have been tested also using air in ambient conditions by the galvanostatic recurrent pulse method with each pulse cycle lasting 10 minutes (5 minute discharge/charge each) at a fixed current of 50 mA. The pulse cycling technique is an excellent diagnostic tool for evaluating the battery's rechargeability by switching the polarity of applied current in short intervals. The SS mesh electrode with directly grown Co_3O_4 NW array exhibits superior initial charge and discharge potentials of 2.0 and 0.98 V, respectively **(Figure 7.7b)**. Even after 100 pulse cycle, the discharge and charge potentials virtually have remained unchanged, which is indicative of excellent rechargeability. In fact, even after 1500 pulse cycles, the performance of the SS mesh electrode shows only a slight decrease in the discharge potential **(Figure 7.8)**. In contrast, the conventional Co_3O_4 NW sprayed and Pt/C sprayed GDL electrodes show significant potential losses after 100 and 60 pulse cycles,

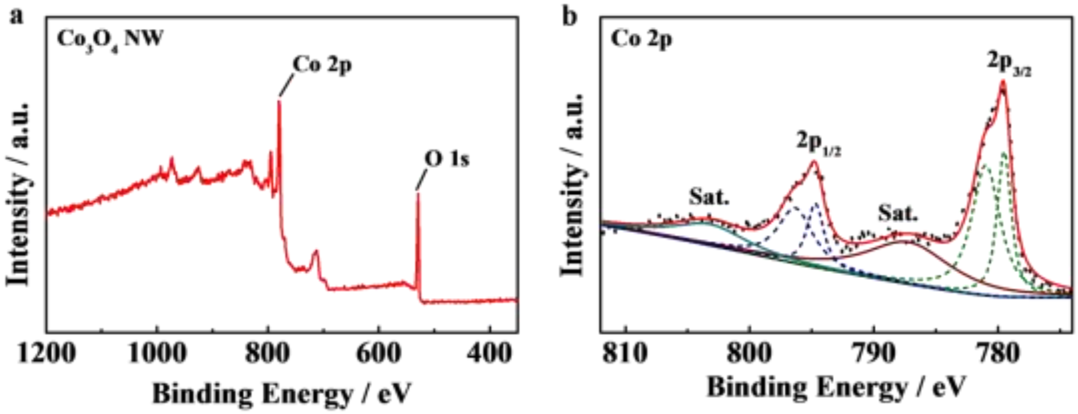

Figure 7.6 (a) XPS survey of Co_3O_4 NW, and (b) de-convoluted high resolution XPS spectrum of Co 2p peak. Reproduced in adapted form from ref. 49 with permission from Wiley.

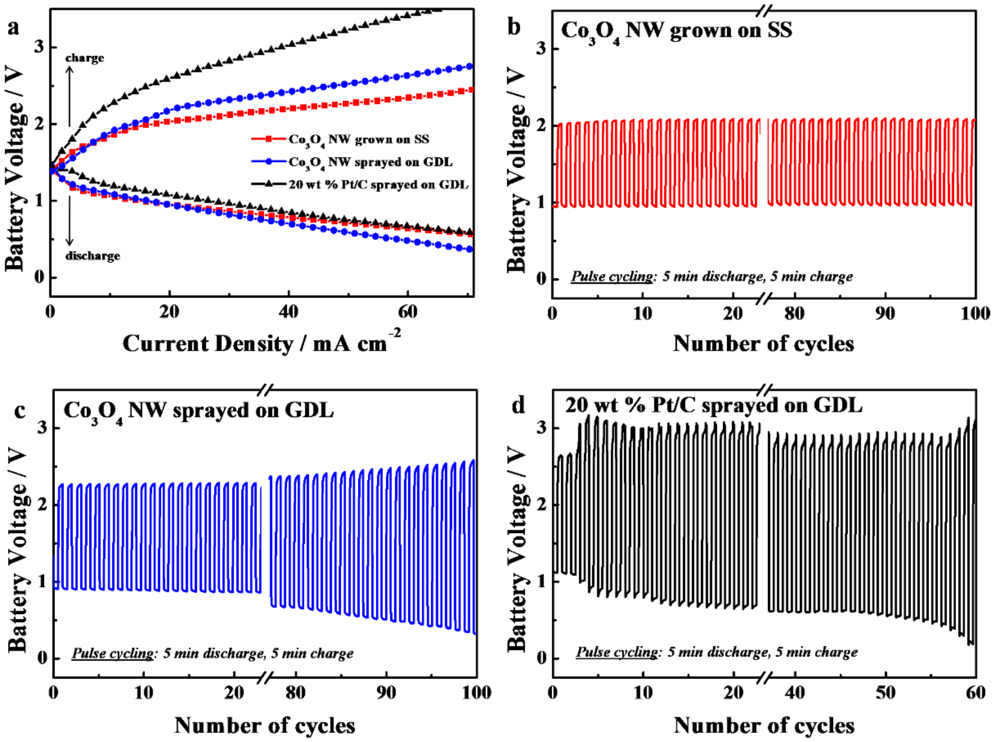

Figure 7.7 (a) Galvanodynamic discharge and charge polarization curves obtained by using air in ambient condition of Co_3O_4 NW grown on SS mesh (red square), Co_3O_4 NW sprayed on GDL (blue circle), and Pt/C sprayed on GDL (black triangle). Galvanostatic pulse cycling at 50 mA using air in ambient condition of (b) Co_3O_4 NW grown on SS mesh, (c) Co_3O_4 NW sprayed on GDL, and (d) Pt/C sprayed on GDL. Reproduced in adapted form from ref. 49 with permission from Wiley.

respectively **(Figure 7.5c and d)**. The carbon-based GDL and the polymer binder used to prepare the electrodes most likely have undergone deterioration.

The evaluation of the enhanced electrical properties and the kinetics of the oxygen reactions of the advanced SS mesh electrode are performed by electrochemical impedance spectroscopy (EIS) **(Figure 7.9)**. A typical Nyquist plot of a single-cell practical zinc-air battery is composed of two semi-circles that correspond to different battery processes well-described by

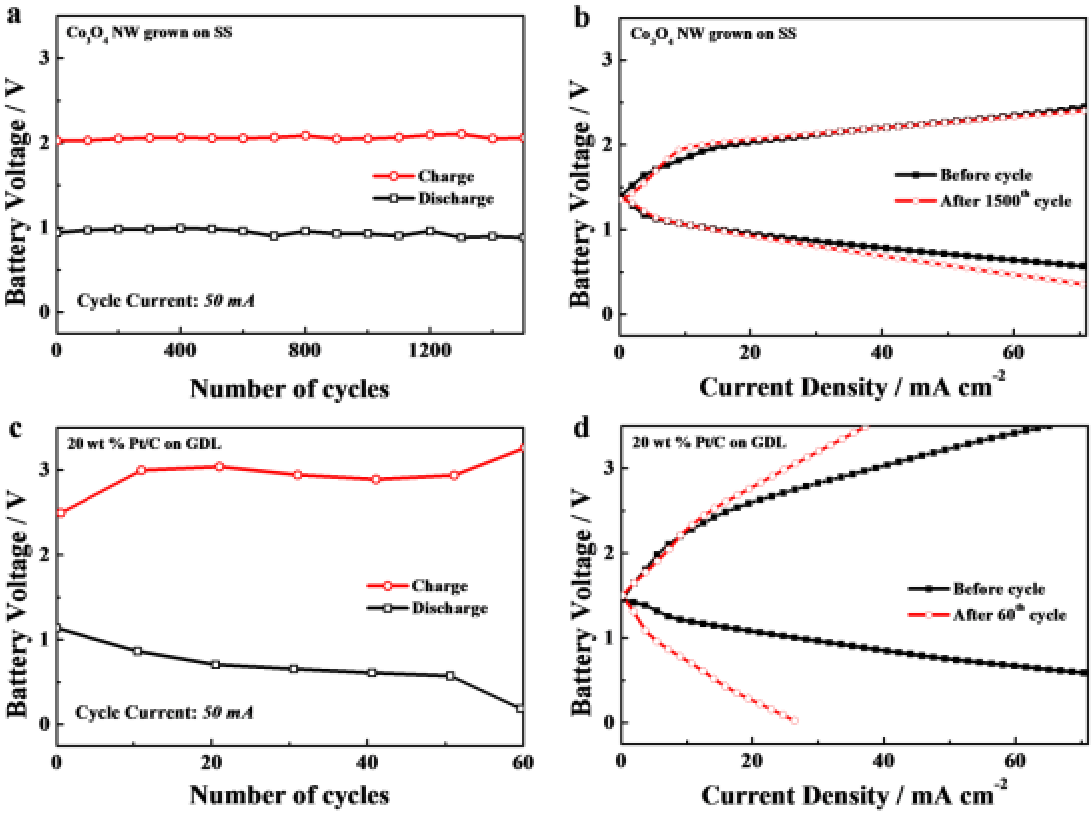

Figure 7.8 The galvanostatic recurrent pulse cycling, and (b, d) galvanodynamic charge and discharge of single-cell practical zinc-air batteries fabricated using the advanced Co_3O_4 NW SS electrode and the conventional 20 wt % Pt/C sprayed GDL electrode. Reproduced in adapted form from ref. 49 with permission from Wiley.

an equivalent circuit with five elements, R_s, Q_{int}, R_{int}, Q_{dl}, and R_{ct} **(Figure 9, inset)**.[62,135] The values of these elements for each electrode investigated are listed in **Table 7.1**. The advanced SS mesh electrode shows significantly lower values for all three resistances, which again highlights the advantages of the hierarchical design of the air electrode. The lowest R_s value is attributed to the reduction of the internal resistance by directly coupling the active Co_3O_4 NW array onto the current collector and reducing the battery components required. In comparison, the conventional GDL electrode sprayed with Co_3O_4 NW exhibits much larger R_s likely due to randomly oriented NW

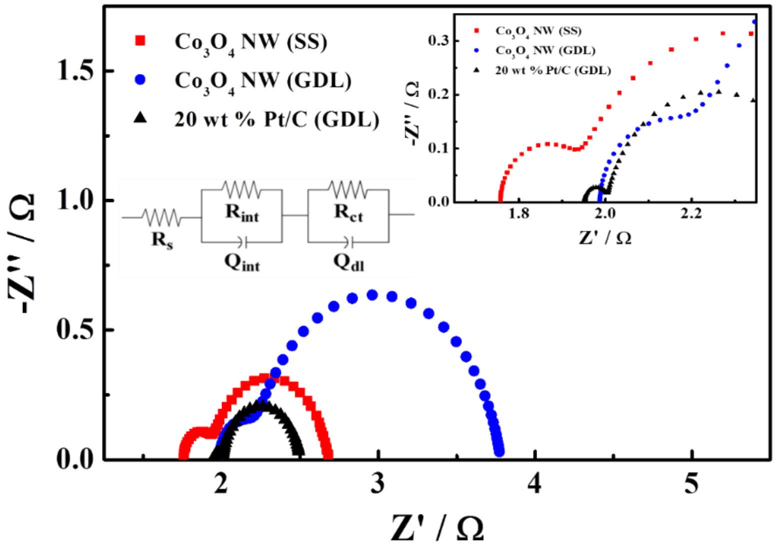

Figure 7.9 Nyquist plots obtained by electrochemical impedance spectroscopy using air in ambient condition of Co_3O_4 NW grown on SS mesh (red square), Co_3O_4 NW sprayed on GDL (blue circle), and Pt/C sprayed on GDL (black triangle). (Inset: High frequency range of the Nyquist plot, and the equivalent circuit) Reproduced in adapted form from ref. 49 with permission from Wiley.

(no longer individually self-standing) with possible particle aggregation. R_{int} of the advance electrode is also much lower than that of the conventional electrodes as the interfacing of the NW array with electrolyte is much easier in the self-standing geometry and without the interference from the polymer binder. In addition, the advanced electrode exhibits much reduced R_{ct} compared to that of the conventional electrode, which is attributed to enhanced transfer of charges and greater active material utilization during the electrochemical reaction.

Building upon the demonstration of high functionality of the advanced electrode, its practicality is demonstrated by investigating the long term durability by the extended cycling test (3 hour discharge followed by 3 hour charge) in a practical zinc-air battery. The advanced SS

Table 7.1 The values of the equivalent circuit elements based on the EIS analysis of Co_3O_4 NW grown on SS mesh, Co_3O_4 sprayed on GDL, and Pt/C sprayed on GDL. Reproduced in adapted form from ref. 49 with permission from Wiley.

Element	**Co_3O_4 NW grown on SS mesh**	***Co_3O_4 NW sprayed on GDL***	***20 wt % Pt/C sprayed on GDL***
R_s [Ω]	1.76	1.987	2.05
R_{int} [Ω]	0.179	0.209	0.050
R_{ct} [Ω]	0.744	1.58	0.498
Q_{int} [$S \cdot s^n$]	0.0378	0.0155	0.207
Q_{dl} [$S \cdot s^n$]	1.49×10^{-3}	9.73×10^{-4}	2.55×10^{-3}

electrode with directly coupled Co_3O_4 NW demonstrates excellent charge and discharge potentials, consistent with the pulse cycling **(Figure 7.10a)**. The discharge profiles show a shallow linear potential drop over the duration of the three hour battery discharge, which is ascribed to the gradual exhaustion of the hydroxide ions in the electrolyte during ORR, not due to the degradation in the performance of the electrode. The lack of hydroxide ions in the electrolyte can be simply refuelled in practice by utilizing a flow electrolyte battery design. The extended cycling test of the advanced SS electrode shows remarkable charge and discharge potential retentions (97 and 94 %, respectively) even after 100 cycles (nearly a month) **(Figure 7.11)**. In comparison, the conventional GDL electrode demonstrates very poor rechargeability, lasting only four cycles **(Figure 7.10b)**. The peaks observed in the charge profiles of the conventional electrode, which are absent in those of the SS mesh electrode, are attributed to the carbon corrosion of the GDL and the

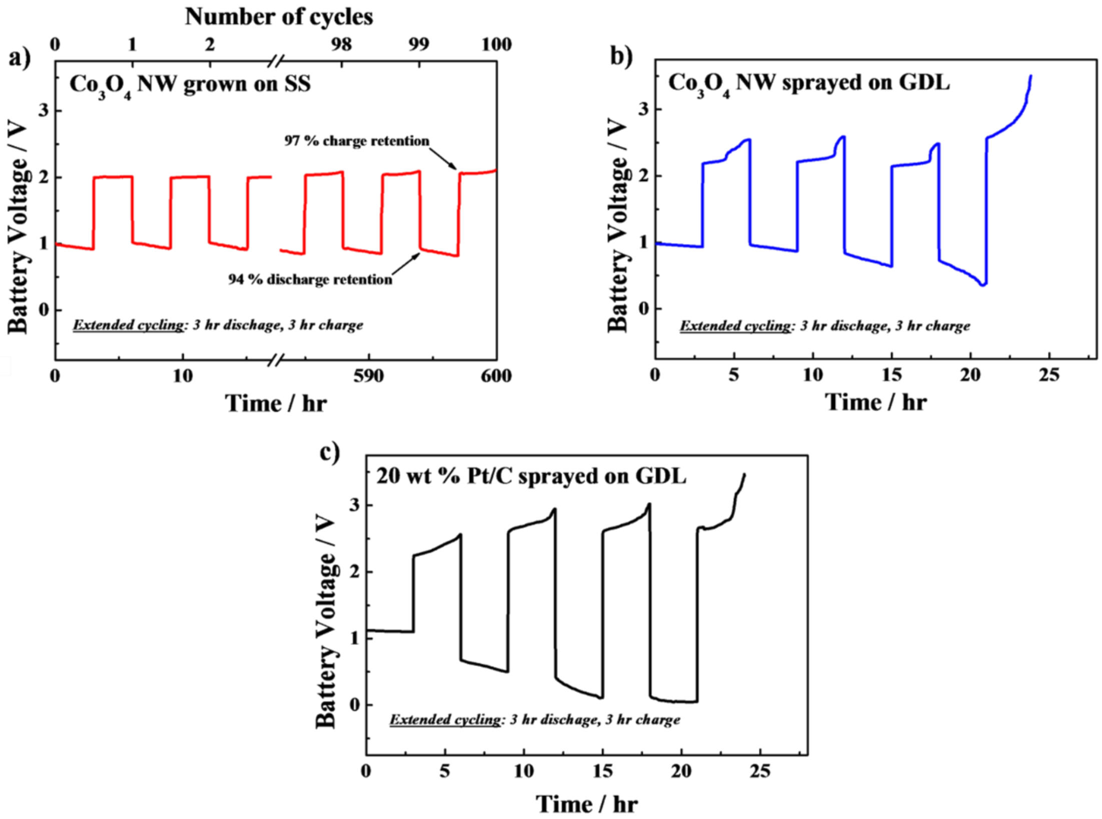

Figure 7.10 The extended practical zinc-air battery cycling tests using air in ambient condition of (a) Co_3O_4 NW grown on SS mesh, (b) Co_3O_4 NW sprayed on GDL, and (c) Pt/C sprayed on GDL. Reproduced in adapted form from ref. 49 with permission from Wiley.

polymer binder at higher charge potentials. This highly undesirable reactions lead to the physical degradation of the air cathode, significantly reducing the rechargeability of the zinc-air battery. The detrimental effect of using the conventional GDL is also observed with Pt/C sprayed electrode, where a significantly limited rechargeability of only four cycles is observed **(Figure 7.10c)**.

After 20 cycles, Co_3O_4 NW have remained almost unchanged from that of the fresh electrode with slight smoothening of the surface, which is attributed to the crystallite dissolution **(Figure 7.12a, and b)**. However, the SS mesh is still densely coated with Co_3O_4 NW array,

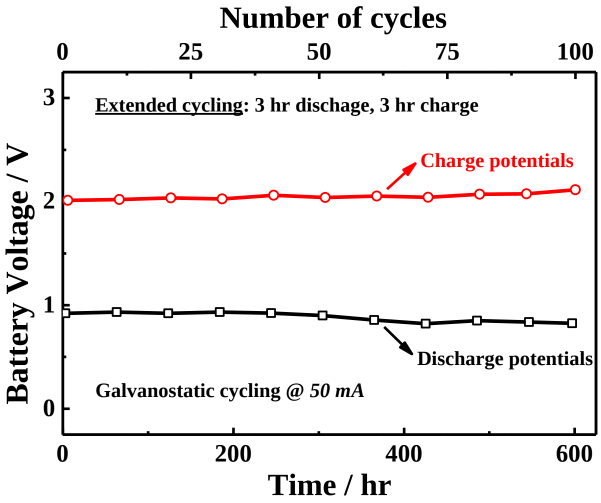

Figure 7.11 Extended galvanostatic cycling of a single-cell practical zinc-air battery using the advanced Co_3O_4 NW SS electrode. Up to 100 cycles, which is equivalent to 25 days, have been demonstrated. Very stable charge and discharge potentials up to 50 cycles are observed then the discharge potential starts to gradually decrease, but still retains much of the initial potential at the end of 100 cycles. The excellent cyclability of the advanced SS electrode using air in the ambient is due to not only the hierarchical self-standing electrode architecture, but also the effectiveness of the mesoporous spinel Co_3O_4 NW as highly efficient bi-functional catalyst for both ORR and OER. Reproduced in adapted form from ref. 49 with permission from Wiley.

maintaining the direct coupling. Remarkably even after 100 extended cycles, Co_3O_4 NW still have retained its nanostructure even though the surface morphology appears to have undergone a considerable dissolution **(Figure 7.12c, and d)**. Also, Co_3O_4 NW array is still densely coupled to the SS mesh current collector, which is probably the reason for retaining such high potential retentions even after extremely long battery operation.

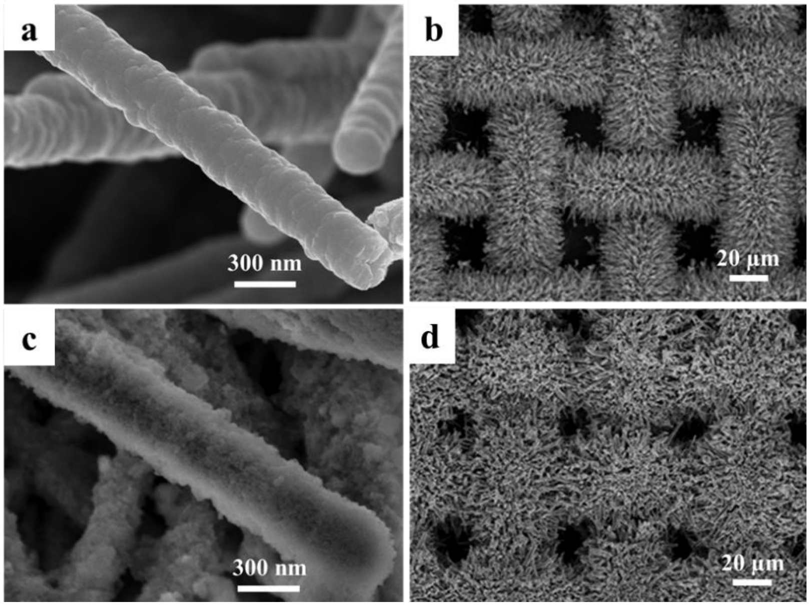

Figure 7.12 Surface morphology of Co_3O_4 NW and structural integrity of the array (a, and b) after 20 cycles, and (c, and d) after 100 cycles. Reproduced in adapted form from ref. 49 with permission from Wiley.

7.4 Summary

In summary, advanced air electrode design has been successfully engineered for extremely durable zinc-air battery applications. The electrode is composed of hierarchical self-standing mesoporous Co_3O_4 NW array as highly active bi-functional catalyst for both ORR and OER. Co_3O_4 NW array is directly coupled to the underlying SS mesh current collector via a facile synthesis, which does not require the use of any ancillary material. The advanced electrode preparation also eliminates conventionally used physical deposition processes such as spray-coating or drop-casting. Compared to the conventional GDL electrodes, the advanced electrode exhibits superior charge and discharge potentials at high currents. Furthermore, 1500 pulse cycles are demonstrated without significant performance degradation, exhibiting excellent rechargeability. In addition, superior internal, interfacial, and charge transfer resistances of the advanced electrode have been confirmed by EIS, attributed to the advantages of directly coupling Co_3O_4 NW onto the current collector. Finally, remarkable electrochemical durability of the advanced electrode is observed utilizing air in ambient conditions, demonstrating extended cycling of 600 hours with charge and discharge potential retentions of 97 and 94 %, respectively. This excellent longevity of the advanced electrode is attributed to the directly coupled Co_3O_4 NW array onto the SS mesh that remains intact and highly active even after extremely long battery operation.

8. Conclusions and Future Work

8.1 Conclusions

In the present thesis, non-precious cobalt based spinel oxide nanostructures have been successfully developed as efficient bi-functional electrocatalysts for rechargeable zinc-air batteries. The main objectives mentioned in the beginning of the thesis have been fulfilled successfully, including nano-structural engineering of cobalt based spinel oxide catalysts to improve overall catalytic activity and durability via transition metal substitution and nano-carbon hybrid formation. Additionally, active nanostructured spinel cobalt oxide catalyst has been successfully integrated into an active catalyst/current collector assembly via a direct chemical growth method to produce rechargeable air electrodes in a facile and scalable manner. With spinel cobalt oxides consistently being reported in the literature as efficient bi-functional ORR/OER catalysts, the hypothesis of this thesis was that nano-engineering methods which enhance the surface area and porosity would lead to significantly improved electrocatalytic activity and durability. Additionally, substituting interstitial sites of the spinel cobalt oxide with various other metals such as Ni and Mn would lead to changes in local electronic properties of the active site which enhances the catalytic activity. Finally, it was hypothesized that the active catalyst directly deposited on a non-carbon current collector such as a piece of stainless steel mesh would result in significantly improved zinc-air battery durability since the corrosion of carbon can be circumvented during the charging process.

Earlier in the thesis work, mesoporous hexagonal nano-disks composed of cobalt oxide was successfully synthesized via a facile surfactant-assisted hydrothermal technique, followed by a thermal annealing process in air. The XRD characterization revealed that the nano-disks had a spinel oxide crystal structure, which is known to be bi-functionally active towards oxygen reduction and oxygen evolution reactions. Additionally microscopic analyses revealed that the nano-disks were characterized with meso-sized pores which improves mass transport of reactants and increases active site exposure during the electrochemical reactions. This unique structure was synthesized with the addition of PVP during the hydrothermal reaction step which acted as a capping agent to allow anisotropic growth of the oxide into two-dimensional nano-disk structures. Additionally, during the heat treatment process, the adsorbed PVP decomposed and left behind pores in the nano-disks further increasing the surface area. The bi-functional catalytic activity of cobalt oxide nano-disks was evaluated using a home-built rechargeable zinc-air battery prototype. Specifically, the nano-disks demonstrated significantly improved charge and discharge voltages of 2.2, and 1.1 V respectively, at the output current density of 20 mA cm^{-2}, compared to nano-particles that have a random granular morphology, which demonstrated 2.3, and 0.8 V at the same current density. Compositionally, both the nano-disks and nano-particles were characterized to be spinel oxides. Therefore, the performance improvements of the nano-disks were attributed to the unique two-dimension porous morphology, which increased the active surface area as well as the mass transport of reactants such as hydroxide ions during the battery reactions.

Having clearly seen the morphological advantage of two-dimensional mesoporous nano-disk structures over randomly shaped nanoparticles for ORR/OER electrocatalysis, composition study was conducted in the next study using the same nano-disk morphology. Specifically, bi-functional catalytic activity of Co_3O_4 nano-disks was further improved by inserting Ni ions into the spinel crystal lattice, as well as by introducing high surface area reduced graphene nano-sheets as the catalyst support, resulting in $NiCo_2O_4$/G hybrid catalyst. Keeping the same nano-disk morphology of the spinel oxide allowed for a comparison between $NiCo_2O_4$/G (doped) and Co_3O_4/G (un-doped) hybrids to study the compositional effect on the bi-functional activity. The only thing that changed in terms of the synthesis was the addition of graphene oxide as the carbon support precursor prior to the hydrothermal reaction. The electrochemical evaluation of the hybrid catalyst first revealed activity enhancements with graphene nanosheet support in terms of both the ORR half-wave potential, and OER current density (over 200 mV, and 15 mA cm^{-2} improvement versus unsupported (graphene-free) $NiCo_2O_4$, respectively). Additionally, inserting Ni ions into the pristine cobalt oxide lattice showed similar degrees of improvement in terms of both ORR half-wave potential, and OER current density. Based on the results obtained in this project, the hybrid catalyst activity enhancements were attributed to two main factors: 1. Graphene nanosheet carbon support improved inter-particle interaction and distribution of the nano-disks, and 2. Ni ions in the spinel oxide lattice enhanced the active site interaction with intermediate oxygen species.

To further understand the effect of replacing some of cobalt ions in the spinel crystal structure with other transition metals on the bi-functional catalytic activity, the next study involved the synthesis and electrochemical evaluation of three kinds of self-assembled mesoporous spheres, Co_3O_4 (un-doped), $NiCo_2O_4$, and $MnCo_2O_4$. The mesoporous sphere morphology was obtained by a solvothermal technique with ammonium bicarbonate added during the synthesis as the pore forming agent. In comparison to the nano-disks obtained using PVP as the capping agent in the two previous studies, the morphology of the self-assembled spheres obtained in this project was vastly different. Electrochemical activity-wise, $(Ni,Co)_3O_4$ spheres formed using ammonium bicarbonate outperformed $NiCo_2O_4$ nano-disks formed using PVP in terms of both ORR and OER based on the half-cell test results. The superior activities of $(Ni,Co)_3O_4$ spheres is attributed to the specific crystal orientation of spinel oxide that formed during the synthesis with ammonium bicarbonate. However, it is important to note that variations exist between the self-assembled sphere and the nano-disks which may also influence the catalytic activity such as the amount of Ni ions inserted into the spinel lattice and their oxidation states. Among the self-assembled spheres synthesized, the ORR activity increased in the order of $(Mn,Co)_3O_4 < Co_3O_4 < (Ni,Co)_3O_4$ in terms of on-set and half-wave potentials, and that of OER increased in the order of $(Mn,Co)_3O_4 < (Ni,Co)_3O_4 < Co_3O_4$ in terms of the potential measured at 10 mA cm^{-2}. To corroborate these experimental results, the first-principles density functional theory (DFT) was used to predict the ORR and OER catalytic activities. Based on the computational analysis, the Gibbs free energy obtained at the potential for which all intermediate reactions occur spontaneously showed the same ORR and OER activity trends as the experiment. Similar to the results of the previous chapter, Ni insertion into the octahedral interstitials of the spinel lattice was found to promote charge transfer leading to enhanced electrical conductivity, resulting in the best overall bi-functional catalytic activity (demonstrated the least overpotential). On the other hand, un-doped Co_3O_4 was found to slightly favour OER due to more favourable interaction with oxygen intermediate that facilitated the release of evolved oxygen. The insertion of Mn, which is a relatively less expensive element compared to Co and Ni, resulted in activity sacrifice for both ORR and OER due to the expansion of the spinel lattice leading to less favourable interaction with the oxygen intermediates. This was a successful compositional study of cobalt based spinel oxides as bi-functional catalysts using methods from both experiment and computational analysis, which provided a good basis for selecting the atomic composition of spinel oxides appropriately depending on the specific energy requirement of the application.

Ultimately, bi-functional catalysts that are developed must be integrated into gas diffusion layers to be used as rechargeable air electrodes for metal-air batteries. Hence, the last study focused on designing and fabricating an advanced catalyst/current collector assembly, which consisted of bi-functionally active three-dimensional cobalt oxide nanowire arrays grown directly on stainless steel mesh current collector. This electrode preparation is very different from the conventional electrode preparation methods which rely on physical deposition of a catalyst mixture composed of catalyst, carbon black, and ionomer dispersed in a solvent via methods such as spray-coating, brush-painting, or drop-casting. In comparison, the advanced catalyst/current collector system developed in this chapter consisted of self-standing mesoporous Co_3O_4 NW arrays directly coupled to the underlying SS mesh current collector fabricated by a low-temperature wet chemical synthesis technique. This method effectively eliminated the use of aforementioned ancillary materials (carbon black and ionomer) that undergo corrosion at high charging potentials and degrade the overall electrical conductivity of the electrode. Additionally, physical deposition methods are no longer required since the active catalyst layer is directly grown on the current collector, greatly simplifying the electrode fabrication process for potential scale-up and mass production. The electrochemical impedance spectroscopy was used to confirm superior internal, interfacial, and charge transfer resistances compared to a comparison air electrode prepared by spray-coating using the same Co_3O_4 NW catalyst. As expected, the advanced electrode demonstrated superior charge and discharge rechargeable zinc-air battery potentials, and remarkably long durability lasting over 600 hours of cycling performance with 97 and 94 % charge and discharge potential retentions, respectively. This excellent longevity of the advanced electrode was attributed to the directly coupled Co_3O_4 NW arrays onto SS mesh CC, which was confirmed to remain intact and bi-functionally active even after the extended battery cycle testing.

8.2 Proposed Future Work

It is imperative that future work to follow this thesis further improves the activity and durability of bi-functional catalysts based on the knowledge gained from the above studies. First, it is suggested that in addition to the durability testing conducted by cycling zinc-air battery, more rigorous and systematic analysis of degradation pathways coupled with post-durability characterizations is conducted to understand the degradation mechanisms and come up with appropriate mitigation strategies to prevent performance fading. Second, synthetic methods to apply the concept of fabricating catalyst/current collector assembly without the use of ancillary materials as demonstrated in Chapter 7 are recommended to be developed for other various nano-scale morphologies and atomic compositions to precisely control the bi-functional catalytic activity. Third, the integration of nanostructured carbon support into the catalyst/current collector assembly is highly recommended to improve the charge transport property of the electrode, as well as to induce synergistic bi-functional electrocatalysis using both spinel oxide and carbon. Specific research directions for each of the mentioned recommendations are discussed in more detail in the following paragraphs.

(1) Elucidation of degradation mechanisms and formulation of mitigation strategies

The durability testing presented in Chapter 7 simply consisted of charge-discharge cycles to observe any changes in charge and discharge voltages, followed by the inspection of the electrode assembly via SEM after cycling. To leverage the progress made in this part of the thesis, three different experimental procedures specifically designed for the elucidation of catalyst degradation mechanisms is recommended. First, extended battery cycling is recommended coupled with extensive post-durability characterization including microscopic investigation (SEM, TEM), and compositional analyses (XRD, XPS). In addition, the durability testing is highly suggested to be conducted under varying humidity and temperature to understand the behaviour of bi-functional catalysts in real-world situations, followed by the above mentioned post-durability characterization. Based on the knowledge gained from this extensive durability analysis, degradation prevention strategies can be designed appropriately.

(2) Morphological and compositional control of catalyst/current collector assembly

Chapter 7 focused on the synthesis of Co_3O_4 nanowire arrays directly on the stainless steel current collector to fabricate active catalyst/current collector assembly. To explore catalysts with different atomic compositions grown on the current collector, other first-row transition metal precursors such as Ni, Mn, and Fe can be incorporated into the spinel oxide structures similar to the studies demonstrated in Chapter 5, and 6. For example, the same synthesis strategy used in Chapter 7 can be used to grow vertically standing nanowires that are made of nickel cobalt or manganese cobalt oxides to investigate their ORR/OER bi-functionality. Morphology-wise, other facile and scalable synthesis techniques can be developed based on high throughput methods such as electrodeposition of spinel oxides to fabricate large-area electrodes for high energy density applications such as EVs. The electrodeposition technique is known in the literature to be highly robust and reproducible method for synthesizing spinel oxide materials with hierarchical nano-scale morphologies such as porous nano-walls and nano-needles.

(3) Hybridization of bi-functional spinel catalysts with nanostructured carbon

Ultimately, the ideal rechargeable air electrode design would consist of layers of nanostructured active catalyst and carbon composite directly coupled to a substrate (i.e. current collector). This design effectively combines all of the ideas presented and discussed in this thesis work. Since carbon is susceptible to electrochemical corrosion at high charging potentials, it can be inserted in between the catalyst layer and the growth substrate. This would allow the carbon layer to act not only as a highly conductive interfacial layer to facilitate charge transport across the electrode, but also as an active electrocatalyst layer itself particularly for facilitating ORR. The OER can be facilitated by the nanostructured spinel oxide layer which will be deposited over the carbon layer. The schematic illustration of the advanced catalyst/carbon/current collector design is shown in **Figure 8.1** below. Specifically, a high surface area carbon layer composed of carbon nanotubes or graphene nanosheets doped with nitrogen can be formed by the injection chemical vapor deposition (CVD) technique. Next, facile and high throughput method such as electrodeposition can be used to grow nanostructured spinel oxides such as mesoporous nanowalls on top of the carbon layer. This design would allow the outer spinel oxide layer to primarily catalyze OER, while the underlying carbon layer to primarily catalyze ORR, and these two layers can work synergistically to further improve the overall bi-functionality. Once the feasibility of this design is confirmed, one-pot synthesis methods can be developed to simultaneously deposit nano-carbon and spinel oxide catalysts to further make the fabrication process for rechargeable air electrodes more practically viable.

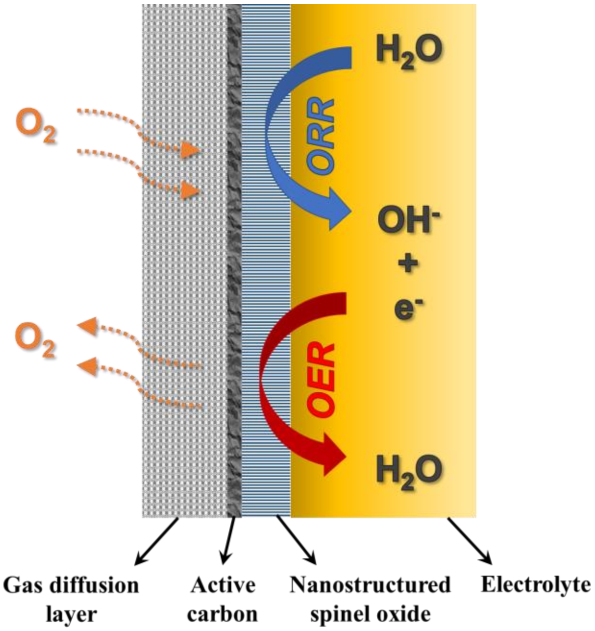

Figure 8.1 Recommended future rechargeable air electrode design based on nano-carbon/spinel oxide hybrid grown on current collector.

REFERENCES

1 Cheng, F. Y. & Chen, J. Metal-air batteries: from oxygen reduction electrochemistry to cathode catalysts. *Chemical Society Reviews* **41**, 2172-2192 (2012).

2 Girishkumar, G., McCloskey, B., Luntz, A. C., Swanson, S. & Wilcke, W. Lithium - Air Battery: Promise and Challenges. *Journal of Physical Chemistry Letters* **1**, 2193-2203 (2010).

3 Lee, J. S. *et al.* Metal-Air Batteries with High Energy Density: Li-Air versus Zn-Air. *Advanced Energy Materials* **1**, 34-50 (2011).

4 Bruce, P. G., Freunberger, S. A., Hardwick, L. J. & Tarascon, J. M. Li-O_2 and Li-S batteries with high energy storage. *Nature Materials* **11**, 19-29 (2012).

5 Rahman, M. A., Wang, X. & Wen, C. High energy density metal-air batteries: a review. *Journal of The Electrochemical Society* **160**, A1759-A1771 (2013).

6 Lee, D. U. *et al.* Recent progress and perspectives on bi-functional oxygen electrocatalysts for advanced rechargeable metal–air batteries. *Journal of Materials Chemistry A* **4**, 7107-7134 (2016).

7 Neburchilov, V., Wang, H. J., Martin, J. J. & Qu, W. A review on air cathodes for zinc-air fuel cells. *J Power Sources* **195**, 1271-1291 (2010).

8 Zhang, S. S. *et al.* A review of platinum-based catalyst layer degradation in proton exchange membrane fuel cells. *J Power Sources* **194**, 588-600 (2009).

9 Morozan, A., Jousselme, B. & Palacin, S. Low-platinum and platinum-free catalysts for the oxygen reduction reaction at fuel cell cathodes. *Energy & Environmental Science* **4**, 1238-1254 (2011).

10 Seo, M. H., Choi, S. M., Kim, H. J. & Kim, W. B. The graphene-supported Pd and Pt catalysts for highly active oxygen reduction reaction in an alkaline condition. *Electrochemistry Communications* **13**, 182-185 (2011).

11 Norskov, J. K. *et al.* Origin of the overpotential for oxygen reduction at a fuel-cell cathode. *Journal of Physical Chemistry B* **108**, 17886-17892 (2004).

12 Sheng, W. C., Chen, S., Vescovo, E. & Shao-Horn, Y. Size Influence on the Oxygen Reduction Reaction Activity and Instability of Supported Pt Nanoparticles. *Journal of the Electrochemical Society* **159** (2012).

13 Lu, Y. C. *et al.* Platinum-Gold Nanoparticles: A Highly Active Bifunctional Electrocatalyst for Rechargeable Lithium-Air Batteries. *Journal of the American Chemical Society* **132**, 12170-12171 (2010).

14 Reier, T., Oezaslan, M. & Strasser, P. Electrocatalytic Oxygen Evolution Reaction (OER) on Ru, Ir, and Pt Catalysts: A Comparative Study of Nanoparticles and Bulk Materials. *ACS Catalysis* **2**, 1765-1772 (2012).

15 Seitz, L. C. *et al.* A highly active and stable $IrO_x/SrIrO_3$ catalyst for the oxygen evolution reaction. *Science* **353**, 1011-1014 (2016).

16 McCrory, C. C. L., Jung, S., Peters, J. C. & Jaramillo, T. F. Benchmarking Heterogeneous Electrocatalysts for the Oxygen Evolution Reaction. *Journal of the American Chemical Society* **135**, 16977-16987 (2013).

17 Chen, Z., Waje, M., Li, W. & Yan, Y. Supportless Pt and PtPd Nanotubes as Electrocatalysts for Oxygen-Reduction Reactions. *Angewandte Chemie* **119**, 4138-4141 (2007).

18 Ioroi, T., Kitazawa, N., Yasuda, K., Yamamoto, Y. & Takenaka, H. Iridium oxide/platinum electrocatalysts for unitized regenerative polymer electrolyte fuel cells. *Journal of The Electrochemical Society* **147**, 2018-2022 (2000).

19 Yang, S. B. *et al.* Efficient Synthesis of Heteroatom (N or S)-Doped Graphene Based on Ultrathin Graphene Oxide-Porous Silica Sheets for Oxygen Reduction Reactions. *Advanced Functional Materials* **22**, 3634-3640 (2012).

20 Liang, Y. Y. *et al.* Co_3O_4 nanocrystals on graphene as a synergistic catalyst for oxygen reduction reaction. *Nature Materials* **10**, 780-78 (2011).

21 Chen, Z. *et al.* Highly Active and Durable Core-Corona Structured Bifunctional Catalyst for Rechargeable Metal-Air Battery Application. *Nano Letters* **12**, 1946-1952 (2012).

22 Chen, Z. *et al.* Manganese dioxide nanotube and nitrogen-doped carbon nanotube based composite bifunctional catalyst for rechargeable zinc-air battery. *Electrochimica Acta* **69**, 295-300 (2012).

23 Jörissen, L. Bifunctional oxygen/air electrodes. *J Power Sources* **155**, 23-32 (2006).

24 Park, J., Park, M., Nam, G., Lee, J. s. & Cho, J. All-Solid-State Cable-Type Flexible Zinc–Air Battery. *Advanced Materials* **27**, 1396-1401 (2015).

25 Fu, J. *et al.* Flexible High-Energy Polymer-Electrolyte-Based Rechargeable Zinc–Air Batteries. *Advanced Materials* **27**, 5617-5622 (2015).

26 Zhang, X. G. Fibrous zinc anodes for high power batteries. *J Power Sources* **163**, 591-597 (2006).

27 McLarnon, F. R. & Cairns, E. J. The Secondary Alkaline Zinc Electrode. *Journal of the Electrochemical Society* **138**, 645-656 (1991).

28 Arora, P. & Zhang, Z. Battery Separators. *Chemical Reviews* **104**, 4419-4462 (2004).

29 Hsu, L. C. & Sheibley, D. W. Inexpensive Cross-Linked Polymeric Separators Made from Water-Soluble Polymers. *Journal of the Electrochemical Society* **129**, 251-254 (1982).

30 Sheibley, D. W., Manzo, M. A. & Gonzalez-Sanabria, O. D. Cross-Linked Polyvinyl Alcohol Films as Alkaline Battery Separators. *Journal of the Electrochemical Society* **130**, 255-259 (1983).

31 Lewandowski, A., Skorupska, K. & Malinska, J. Novel poly(vinyl alcohol)-KOH-H_2O alkaline polymer electrolyte. *Solid State Ionics* **133**, 265-271 (2000).

32 Yang, C. C. & Lin, S. J. Alkaline composite PEO-PVA-glass-fibre-mat polymer electrolyte for Zn-air battery. *J Power Sources* **112**, 497-503 (2002).

33 Dewi, E. L., Oyaizu, K., Nishide, H. & Tsuchida, E. Cationic polysulfonium membrane as separator in zinc-air cell. *J Power Sources* **115**, 149-152 (2003).

34 Sapkota, P. & Kim, H. Zinc-air fuel cell, a potential candidate for alternative energy. *Journal of Industrial and Engineering Chemistry* **15**, 445-450 (2009).

35 Sapkota, P. & Kim, H. An experimental study on the performance of a zinc air fuel cell with inexpensive metal oxide catalysts and porous organic polymer separators. *Journal of Industrial and Engineering Chemistry* **16**, 39-44 (2010).

36 Muller, S., Striebel, K. & Haas, O. $La_{0.6}Ca_{0.4}CoO_3$ - a Stable and Powerful Catalyst for Bifunctional Air Electrodes. *Electrochimica Acta* **39**, 1661-1668 (1994).

37 Wang, Z.-L., Xu, D., Xu, J.-J. & Zhang, X.-B. Oxygen electrocatalysts in metal-air batteries: from aqueous to nonaqueous electrolytes. *Chemical Society Reviews* (2014).

38 Nikolova, V. *et al*. Electrocatalysts for bifunctional oxygen/air electrodes. *J Power Sources* **185**, 727-733 (2008).

39 Wang, B. Recent development of non-platinum catalysts for oxygen reduction reaction. *J Power Sources* **152**, 1-15 (2005).

40 Hamdani, M., Singh, R. N. & Chartier, P. Co_3O_4 and Co- Based Spinel Oxides Bifunctional Oxygen Electrodes. *Int. J. Electrochem. Sci.* **5**, 556-577 (2010).

41 Cao, R., Lee, J.-S., Liu, M. & Cho, J. Recent Progress in Non-Precious Catalysts for Metal-Air Batteries. *Advanced Energy Materials* **2**, 816-829 (2012).

42 Spendelow, J. S. & Wieckowski, A. Electrocatalysis of oxygen reduction and small alcohol oxidation in alkaline media. *Physical Chemistry Chemical Physics* **9**, 2654-2675 (2007).

43 Christensen, P. A., Hamnett, A. & Linares-Moya, D. Oxygen reduction and fuel oxidation in alkaline solution. *Physical Chemistry Chemical Physics* **13**, 5206-5214 (2011).

44 Zinola, C., Arvia, A., Estiu, G. & Castro, E. A quantum chemical approach to the influence of platinum surface structure on the oxygen electroreduction reaction. *The Journal of Physical Chemistry* **98**, 7566-7576 (1994).

45 Cheng, F. & Chen, J. Metal–air batteries: from oxygen reduction electrochemistry to cathode catalysts. *Chemical Society Reviews* **41**, 2172-2192 (2012).

46 Doyle, M., Rajendran, G., Vielstich, W., Gasteiger, H. & Lamm, A. Handbook of Fuel Cells Fundamentals, Technology and Applications. *Fuel cell technology and applications* **3** (2003).

47 Suntivich, J. *et al.* Design principles for oxygen-reduction activity on perovskite oxide catalysts for fuel cells and metal–air batteries. *Nature chemistry* **3**, 546-550 (2011).

48 Chen, Z., Higgins, D., Yu, A., Zhang, L. & Zhang, J. A review on non-precious metal electrocatalysts for PEM fuel cells. *Energy & Environmental Science* **4**, 3167-3192 (2011).

49 Lee, D. U., Choi, J.-Y., Feng, K., Park, H. W. & Chen, Z. Advanced Extremely Durable 3D Bifunctional Air Electrodes for Rechargeable Zinc-Air Batteries. *Advanced Energy Materials* **4**, 1301389 (2014).

50 Xiao, J. *et al.* Surface structure dependent electrocatalytic activity of Co_3O_4 anchored on graphene sheets toward oxygen reduction reaction. *Scientific reports* **3** (2013).

51 Sa, Y. J., Kwon, K., Cheon, J. Y., Kleitz, F. & Joo, S. H. Ordered mesoporous Co_3O_4 spinels as stable, bifunctional, noble metal-free oxygen electrocatalysts. *Journal of Materials Chemistry A* **1**, 9992-10001 (2013).

52 Menezes, P. W. *et al.* Cobalt–Manganese-Based Spinels as Multifunctional Materials that Unify Catalytic Water Oxidation and Oxygen Reduction Reactions. *ChemSusChem* **8**, 164-171 (2015).

53 Tan, Y. *et al.* Insight the effect of surface Co cations on the electrocatalytic oxygen evolution properties of cobaltite spinels. *Electrochimica Acta* **121**, 183-187 (2014).

54 Cheng, F. *et al.* Rapid room-temperature synthesis of nanocrystalline spinels as oxygen reduction and evolution electrocatalysts. *Nat Chem* **3**, 79-84 (2011).

55 Prabu, M., Ketpang, K. & Shanmugam, S. Hierarchical nanostructured $NiCo_2O_4$ as an efficient bifunctional non-precious metal catalyst for rechargeable zinc–air batteries. *Nanoscale* **6**, 3173-3181 (2014).

56 Shackelford, J. F. & Muralidhara, M. K. Introduction to materials science for engineers. (2005).

57 Brunauer, S., Emmett, P. H. & Teller, E. Adsorption of Gases in Multimolecular Layers. *Journal of the American Chemical Society* **60**, 309-319 (1938).

58 Xiao, W., Wang, D. L. & Lou, X. W. Shape-Controlled Synthesis of MnO_2 Nanostructures with Enhanced Electrocatalytic Activity for Oxygen Reduction. *Journal of Physical Chemistry C* **114**, 1694-1700 (2010).

59 Lee, D. U. *et al.* Morphologically controlled Co_3O_4 nanodisks as practical bi-functional catalyst for rechargeable zinc–air battery applications. *Electrochemistry Communications* **43**, 109-112 (2014).

60 Sun, Y. & Xia, Y. Shape-Controlled Synthesis of Gold and Silver Nanoparticles. *Science* **298**, 2176-2179 (2002).

61 Hou, Y., Kondoh, H., Shimojo, M., Kogure, T. & Ohta, T. High-Yield Preparation of Uniform Cobalt Hydroxide and Oxide Nanoplatelets and Their Characterization. *The Journal of Physical Chemistry B* **109**, 19094-19098 (2005).

62 Thiele, D. & Züttel, A. Electrochemical characterisation of air electrodes based on La0.6Sr0.4CoO3 and carbon nanotubes. *J Power Sources* **183**, 590-594 (2008).

63 Roen, L. M., Paik, C. H. & Jarvi, T. D. Electrocatalytic Corrosion of Carbon Support in PEMFC Cathodes. *Electrochemical and Solid-State Letters* **7**, A19-A22 (2004).

64 Wang, X., Li, W., Chen, Z., Waje, M. & Yan, Y. Durability investigation of carbon nanotube as catalyst support for proton exchange membrane fuel cell. *J Power Sources* **158**, 154-159 (2006).

65 Zhang, J., Sasaki, K., Sutter, E. & Adzic, R. R. Stabilization of Platinum Oxygen-Reduction Electrocatalysts Using Gold Clusters. *Science* **315**, 220-222 (2007).

66 Lee, D. U., Kim, B. J. & Chen, Z. One-pot synthesis of a mesoporous $NiCo_2O_4$ nanoplatelet and graphene hybrid and its oxygen reduction and evolution activities as an efficient bi-functional electrocatalyst. *Journal of Materials Chemistry A* **1**, 4754-4762 (2013).

67 Rashkova, V., Kitova, S., Konstantinov, I. & Vitanov, T. Vacuum evaporated thin films of mixed cobalt and nickel oxides as electrocatalyst for oxygen evolution and reduction. *Electrochimica Acta* **47**, 1555-1560 (2002).

68 Singh, S. P., Samuel, S., Tiwari, S. K. & Singh, R. N. Preparation of thin Co_3O_4 films on Ni and their electrocatalytic surface properties towards oxygen evolution. *International Journal of Hydrogen Energy* **21**, 171-178 (1996).

69 Jasem, S. M. & Tseung, A. C. C. Potentiostatic Pulse Study Of Oxygen Evolution On Teflon-Bonded Nickel-Cobalt Oxide Electrodes. *Journal of The Electrochemical Society* **126**, 1353-1360 (1979).

70 Li, Y., Hasin, P. & Wu, Y. $Ni_xCo_{3-x}O_4$ Nanowire Arrays for Electrocatalytic Oxygen Evolution. *Advanced Materials* **22**, 1926-1929 (2010).

71 Lu, B., Cao, D., Wang, P., Wang, G. & Gao, Y. Oxygen evolution reaction on Ni-substituted Co_3O_4 nanowire array electrodes. *International Journal of Hydrogen Energy* **36**, 72-78 (2011).

72 Salunkhe, R. R. *et al.* Chemical synthesis and electrochemical analysis of nickel cobaltite nanostructures for supercapacitor applications. *Journal of Alloys and Compounds* **509**, 6677-6682 (2011).

73 Wang, H., Gao, Q. & Jiang, L. Facile Approach to Prepare Nickel Cobaltite Nanowire Materials for Supercapacitors. *Small* **7**, 2454-2459 (2011).

74 Yuan, C. *et al.* Facile template-free synthesis of ultralayered mesoporous nickel cobaltite nanowires towards high-performance electrochemical capacitors. *Journal of Materials Chemistry* **22**, 16084-16090 (2012).

75 Geim, A. K. & Novoselov, K. S. The rise of graphene. *Nat Mater* **6**, 183-191 (2007).

76 Yang, S., Feng, X., Wang, X. & Müllen, K. Graphene-Based Carbon Nitride Nanosheets as Efficient Metal-Free Electrocatalysts for Oxygen Reduction Reactions. *Angewandte Chemie International Edition* **50**, 5339-5343 (2011).

77 Wang, H. *et al.* Graphene-Wrapped Sulfur Particles as a Rechargeable Lithium–Sulfur Battery Cathode Material with High Capacity and Cycling Stability. *Nano Letters* **11**, 2644-2647 (2011).

78 Yu, G. *et al.* Solution-Processed Graphene/MnO_2 Nanostructured Textiles for High-Performance Electrochemical Capacitors. *Nano Letters* **11**, 2905-2911 (2011).

79 Qu, L., Liu, Y., Baek, J.-B. & Dai, L. Nitrogen-Doped Graphene as Efficient Metal-Free Electrocatalyst for Oxygen Reduction in Fuel Cells. *ACS Nano* **4**, 1321-1326 (2010).

80 Lee, K. R., Lee, K. U., Lee, J. W., Ahn, B. T. & Woo, S. I. Electrochemical oxygen reduction on nitrogen doped graphene sheets in acid media. *Electrochemistry Communications* **12**, 1052-1055 (2010).

81 Geng, D. *et al.* High oxygen-reduction activity and durability of nitrogen-doped graphene. *Energy & Environmental Science* **4** (2011).

82 Seger, B. & Kamat, P. V. Electrocatalytically Active Graphene-Platinum Nanocomposites. Role of 2-D Carbon Support in PEM Fuel Cells. *The Journal of Physical Chemistry C* **113**, 7990-7995 (2009).

83 Yoo, E. & Zhou, H. Li−Air Rechargeable Battery Based on Metal-free Graphene Nanosheet Catalysts. *ACS Nano* **5**, 3020-3026 (2011).

84 Hummers, W. S. & Offeman, R. E. Preparation of Graphitic Oxide. *Journal of the American Chemical Society* **80**, 1339-1339 (1958).

85 Wang, X. *et al.* Synthesis and Lithium Storage Properties of Co_3O_4 Nanosheet-Assembled Multishelled Hollow Spheres. *Advanced Functional Materials* **20**, 1680-1686 (2010).

86 Sui, Y. *et al.* Low Temperature Synthesis of Cu_2O Crystals: Shape Evolution and Growth Mechanism. *Crystal Growth & Design* **10**, 99-108 (2009).

87 Wang, H. *et al.* Graphene-nickel cobaltite nanocomposite asymmetrical supercapacitor with commercial level mass loading. *Nano Res.* **5**, 605-617 (2012).

88 Nikolov, I. *et al.* Electrocatalytic activity of spinel related cobalties $M_xCo_{3-x}O_4$ (M = Li, Ni, Cu) in the oxygen evolution reaction. *Journal of Electroanalytical Chemistry* **429**, 157-168 (1997).

89 Castro, E. B. & Gervasi, C. A. Electrodeposited Ni–Co-oxide electrodes:characterization and kinetics of the oxygen evolution reaction. *International Journal of Hydrogen Energy* **25**, 1163-1170 (2000).

90 Tang, L. *et al.* Preparation, Structure, and Electrochemical Properties of Reduced Graphene Sheet Films. *Advanced Functional Materials* **19**, 2782-2789 (2009).

91 Belova, I. D. *et al.* Co (III) ions high-spin configuration in nonstoichiometric Co_3O_4 films. *Solid State Communications* **47**, 577-584 (1983).

92 Lee, D. U. *et al.* Self-Assembly of Spinel Nanocrystals into Mesoporous Spheres as Bifunctionally Active Oxygen Reduction and Evolution Electrocatalysts. *ChemSusChem* **10**, 2258-2266 (2017).

93 Lee, J. S. *et al.* Metal–air batteries with high energy density: Li–air versus Zn–air. *Adv. Energy Mater.* **1**, 34-50 (2011).

94 Cheng, F. & Chen, J. Metal–air batteries: from oxygen reduction electrochemistry to cathode catalysts. *Chem. Soc. Rev.* **41**, 2172-2192 (2012).

95 Lee, D. U. *et al.* Recent progress and perspectives on bi-functional oxygen electrocatalysts for advanced rechargeable metal–air batteries. *J. Mater. Chem. A* **4**, 7107-7134 (2016).

96 Lee, D. U., Park, H. W., Park, M. G., Ismayilov, V. & Chen, Z. Synergistic Bifunctional Catalyst Design based on Perovskite Oxide Nanoparticles and Intertwined Carbon Nanotubes for Rechargeable Zinc–Air Battery Applications. *ACS Appl. Mater. Interfaces* **7**, 902-910 (2014).

97 Park, H. W. *et al.* Electrospun porous nanorod perovskite oxide/nitrogen-doped graphene composite as a bi-functional catalyst for metal air batteries. *Nano Energy* **10**, 192-200 (2014).

98 Lee, D. U. *et al.* Morphologically controlled Co_3O_4 nanodisks as practical bi-functional catalyst for rechargeable zinc–air battery applications. *Electrochem. Commun.* **43**, 109-112 (2014).

99 Tao, L. *et al.* Edge-rich and dopant-free graphene as a highly efficient metal-free electrocatalyst for the oxygen reduction reaction. *Chem. Commun.* **52**, 2764-2767 (2016).

100 Risch, M. *et al.* $La_{0.8}Sr_{0.2}MnO_{3-\delta}$ Decorated with $Ba_{0.5}Sr_{0.5}Co_{0.8}Fe_{0.2}O_{3-\delta}$: A Bifunctional Surface for Oxygen Electrocatalysis with Enhanced Stability and Activity. *J. Am. Chem. Soc.* **136**, 5229-5232 (2014).

101 Tian, G. L. *et al.* Toward full exposure of “active sites”: Nanocarbon electrocatalyst with surface enriched nitrogen for superior oxygen reduction and evolution reactivity. *Adv. Funct. Mater.* **24**, 5956-5961 (2014).

102 Lin, Z., Waller, G. H., Liu, Y., Liu, M. & Wong, C.-p. 3D Nitrogen-doped graphene prepared by pyrolysis of graphene oxide with polypyrrole for electrocatalysis of oxygen reduction reaction. *Nano Energy* **2**, 241-248 (2013).

103 Xia, B. Y. *et al.* A metal–organic framework-derived bifunctional oxygen electrocatalyst. *Nat. Energy* **1**, 15006 (2016).

104 Wang, Z. *et al.* Core-shell carbon materials derived from metal-organic frameworks as an efficient oxygen bifunctional electrocatalyst. *Nano Energy* **30**, 368-378 (2016).

105 Wang, J. *et al.* Heterogeneous Electrocatalyst with Molecular Cobalt Ions Serving as the Center of Active Sites. *J. Am. Chem. Soc.* **139**, 1878-1884 (2017).

106 Lee, D. U. *et al.* Highly Active and Durable Nanocrystal-Decorated Bifunctional Electrocatalyst for Rechargeable Zinc–Air Batteries. *ChemSusChem* **8**, 3129-3138 (2015).

107 Wiesenekker, G. & Baerends, E. Quadratic integration over the three-dimensional Brillouin zone. *J. Phys.: Condens. Matter* **3**, 6721 (1991).

108 Perdew, J. P., Burke, K. & Ernzerhof, M. Generalized gradient approximation made simple. *Phys. Rev. Lett.* **77**, 3865 (1996).

109 Zhang, Q. *et al.* Understanding the Anchoring Effect of Two-Dimensional Layered Materials for Lithium–Sulfur Batteries. *Nano Lett.* **15**, 3780-3786 (2015).

110 Gong, X.-Q., Liu, Z.-P., Raval, R. & Hu, P. A systematic study of CO oxidation on metals and metal oxides: density functional theory calculations. *J. Am. Chem. Soc.* **126**, 8-9 (2004).

111 Te Velde, G. & Baerends, E. Numerical integration for polyatomic systems. *J. Comput. Phys.* **99**, 84-98 (1992).

112 Li, J., Croiset, E. & Ricardez-Sandoval, L. Theoretical investigation of the methane cracking reaction pathways on Ni (111) surface. *Chem. Phys. Lett.* **639**, 205-210 (2015).

113 Seo, M. H., Park, H. W., Lee, D. U., Park, M. G. & Chen, Z. Design of highly active perovskite oxides for oxygen evolution reaction by combining experimental and ab initio studies. *ACS Catal.* **5**, 4337-4344 (2015).

114 Li, J., Croiset, E. & Ricardez-Sandoval, L. Effect of metal–support interface during CH_4 and H_2 dissociation on Ni/γ-Al_2O_3: a density functional theory study. *J. Phys. Chem. C* **117**, 16907-16920 (2013).

115 Li, J., Croiset, E. & Ricardez-Sandoval, L. Carbon clusters on the Ni (111) surface: a density functional theory study. *Phys. Chem. Chem. Phys.* **16**, 2954-2961 (2014).

116 Li, Y., Hasin, P. & Wu, Y. $Ni_xCo_{3-x}O_4$ nanowire arrays for electrocatalytic oxygen evolution. *Adv. Mater.* **22**, 1926-1929 (2010).

117 Wiesenekker, G., Te Velde, G. & Baerends, E. Analytic quadratic integration over the two-dimensional Brillouin zone. *J. Phys. C: Solid State Phys.* **21**, 4263 (1988).

118 Zasada, F. *et al.* Surface Structure and Morphology of M [CoM′]O_4 (M= Mg, Zn, Fe, Co and M′= Ni, Al, Mn, Co) Spinel Nanocrystals-DFT+U and TEM Screening Investigations. *J. Phys. Chem. C* **118**, 19085-19097 (2014).

119 Kapteijn, F., Rodriguez-Mirasol, J. & Moulijn, J. A. Heterogeneous catalytic decomposition of nitrous oxide. *Appl. Catal., B* **9**, 25-64 (1996).

120 Liu, X., Qiu, G. & Li, X. Shape-controlled synthesis and properties of uniform spinel cobalt oxide nanocubes. *Nanotechnology* **16**, 3035 (2005).

121 Nørskov, J. K. *et al.* Origin of the overpotential for oxygen reduction at a fuel-cell cathode. *J. Phys. Chem. B* **108**, 17886-17892 (2004).

122 Cong, H.-P. & Yu, S.-H. Shape control of cobalt carbonate particles by a hydrothermal process in a mixed solvent: an efficient precursor to nanoporous cobalt oxide architectures and their sensing property. *Cryst. Growth Des.* **9**, 210-217 (2008).

123 Park, M. G., Lee, D. U., Seo, M. H., Cano, Z. P. & Chen, Z. 3D Ordered Mesoporous Bifunctional Oxygen Catalyst for Electrically Rechargeable Zinc–Air Batteries. *Small* **12**, 2707-2714 (2016).

124 Castro, E. & Gervasi, C. Electrodeposited Ni–Co-oxide electrodes: characterization and kinetics of the oxygen evolution reaction. *Int. J. Hydrogen Energy* **25**, 1163-1170 (2000).

125 Fu, C. *et al.* One-step calcination-free synthesis of multicomponent spinel assembled microspheres for high-performance anodes of Li-ion batteries: a case study of $MnCo_2O_4$. *ACS Appl. Mater. Interfaces* **6**, 2439-2449 (2014).

126 Yang, J., Liu, H., Martens, W. N. & Frost, R. L. Synthesis and characterization of cobalt hydroxide, cobalt oxyhydroxide, and cobalt oxide nanodiscs. *J. Phys. Chem. C* **114**, 111-119 (2009).

127 Kim, T. W., Woo, M. A., Regis, M. & Choi, K.-S. Electrochemical Synthesis of Spinel Type ZnCo2O4 Electrodes for Use as Oxygen Evolution Reaction Catalysts. *J. Phys. Chem. Lett.* **5**, 2370-2374 (2014).

128 Yu, L., Xia, B. Y., Wang, X. & Lou, X. W. General formation of M–MoS_3 (M= Co, Ni) hollow structures with enhanced electrocatalytic activity for hydrogen evolution. *Adv. Mater.* **28**, 92-97 (2016).

129 McCrory, C. C., Jung, S., Peters, J. C. & Jaramillo, T. F. Benchmarking heterogeneous electrocatalysts for the oxygen evolution reaction. *J. Am. Chem. Soc.* **135**, 16977-16987 (2013).

130 Koza, J. A., He, Z., Miller, A. S. & Switzer, J. A. Electrodeposition of Crystalline Co_3O_4-A Catalyst for the Oxygen Evolution Reaction. *Chem. Mater.* **24**, 3567-3573 (2012).

131 Wang, J. *et al.* Hierarchical $NiCo_2O_4$ hollow nanospheres as high efficient bi-functional catalysts for oxygen reduction and evolution reactions. *International Journal of Hydrogen Energy* **41**, 8847-8854 (2016).

132 Indra, A. *et al.* Unification of catalytic water oxidation and oxygen reduction reactions: amorphous beat crystalline cobalt iron oxides. *Journal of the American Chemical Society* **136**, 17530-17536 (2014).

133 Wang, D., Chen, X., Evans, D. G. & Yang, W. Well-dispersed Co_3O_4/Co_2MnO_4 nanocomposites as a synergistic bifunctional catalyst for oxygen reduction and oxygen evolution reactions. *Nanoscale* **5**, 5312-5315 (2013).

134 Greeley, J. *et al.* Alloys of platinum and early transition metals as oxygen reduction electrocatalysts. *Nat. Chem.* **1**, 552-556 (2009).

135 Chen, Z. *et al.* Highly Active and Durable Core–Corona Structured Bifunctional Catalyst for Rechargeable Metal–Air Battery Application. *Nano Letters* **12**, 1946-1952 (2012).

136 Lee, J. S. *et al.* Ketjenblack Carbon Supported Amorphous Manganese Oxides Nanowires as Highly Efficient Electrocatalyst for Oxygen Reduction Reaction in Alkaline Solutions. *Nano Letters* **11**, 5362-5366 (2011).

137 Li, Y. *et al.* Advanced zinc-air batteries based on high-performance hybrid electrocatalysts. *Nat Commun* **4**, 1805 (2013).

138 Kangasniemi, K. H., Condit, D. A. & Jarvi, T. D. Characterization of vulcan electrochemically oxidized under simulated PEM fuel cell conditions. *Journal of The Electrochemical Society* **151**, E125-E132 (2004).

139 Wang, X., Li, W. Z., Chen, Z. W., Waje, M. & Yan, Y. S. Durability investigation of carbon nanotube as catalyst support for proton exchange membrane fuel cell. *J Power Sources* **158**, 154-159 (2006).

140 Li, Y. G., Tan, B. & Wu, Y. Y. Mesoporous Co_3O_4 nanowire arrays for lithium ion batteries with high capacity and rate capability. *Nano Letters* **8**, 265-270 (2008).

141 Yin, Y. D. *et al.* Formation of hollow nanocrystals through the nanoscale Kirkendall Effect. *Science* **304**, 711-714 (2004).

142 Gao, Y. Y., Chen, S. L., Cao, D. X., Wang, G. L. & Yin, J. L. Electrochemical capacitance of Co_3O_4 nanowire arrays supported on nickel foam. *J Power Sources* **195**, 1757-1760 (2010).

143 Li, Y., Tan, B. & Wu, Y. Mesoporous Co_3O_4 nanowire arrays for lithium ion batteries with high capacity and rate capability. *Nano letters* **8**, 265-270 (2008).

144 Hadjiev, V., Iliev, M. & Vergilov, I. The Raman spectra of Co_3O_4. *Journal of Physics C: Solid State Physics* **21**, L199 (1988).

145 Binotto, G. *et al.* Synthesis, characterization, and li-electrochemical performance of highly porous Co_3O_4 powders. *Chem Mater* **19**, 3032-3040 (2007).